



Laser ablation for water isotopic analysis with particular focus in spectral estimation for diffusion studies

Ph.D. Thesis

Eirini Malegiannaki

Supervisors: Vasileios Gkinis, Dorthe Dahl-Jensen, Carlo Barbante

Submitted: November 30, 2024

Preface

This thesis presents original research conducted by Eirini Malegiannaki, during PhD studies from 2021 to 2024. The project was supervised by Vasileios Gkinis, Dorthe Dahl-Jensen (Physics of Ice, Climate and Earth, Niels Bohr Institute, University of Copenhagen) and Carlo Barbante (Ca'Foscari University of Venice). Financial support for this research was provided by the H2020 Marie Skłodowska-Curie Actions through the DEEPICE project (Grant Agreement ID: 955750). Additional financial support was received by Carlsbergfondet (grant no. 2013_01_0899, CF21-0199), Villum Fonden (grant no. 00022995, 00028061), Danmarks Grundforskningsfond (grant no. 10.46540/2032-00228B) and H2020 Marie Skłodowska-Curie Actions (grant no. 101018266).

Part of this thesis is an article titled 'Towards high-resolution water isotope analysis in ice cores using laser ablation cavity ring-down spectroscopy', published in *Analyst*. (DOI: [10.1039/D4AN01054J](https://doi.org/10.1039/D4AN01054J)) A second article was published in *Past Global Changes Magazine* and is included in the Appendix D. (DOI: [10.22498/pages.31.2.64](https://doi.org/10.22498/pages.31.2.64))

Help of others has been acknowledged, and references to all relevant published works have been provided.

Abstract

This thesis presents a novel ice core sampling technique specifically designed for water isotope analysis, by coupling Laser Ablation (LA) with Cavity Ring Down Spectroscopy (CRDS). The micro-destructive nature of LA allows for high spatial resolution and minimal sample usage, addressing the challenges of achieving high accuracy and precision in water isotope measurements from the extremely thin layers at the base of deep ice cores, such as the one obtained from the Beyond EPICA - Oldest Ice Core project.

Two different laser ablation systems were employed in this study. The first system is a custom-made setup dedicated to water isotope studies in ice cores, while the second system uses a commercial LA setup coupled with a CRDS analyzer, serving as a proof of concept of the proposed method.

The first system comprises a femtosecond (fs) laser operating at 1030 nm with an open-design ablation chamber capable of scanning ice core samples up to 55 cm in length. This system was initially designed at the Physics of Ice, Climate, and Earth (PICE) - University of Copenhagen, and its development has been further advanced as part of this thesis. Test measurements were conducted on all critical components contributing to the functionality of a future LA-CRDS system, including laser focusing, gas flow dynamics, and ablation chamber design, along with detailed crater characterization to enhance understanding of the ablation process in ice. These tests provide initial insights into the system's ablation performance.

The second system is a commercial laser ablation setup that consists of an ArF nanosecond (ns) laser operating at 193 nm and an integrated closed-design two-volume ablation chamber accommodating samples up to 5 cm in length. The ns LA system was coupled with a CRDS water isotopic analyzer at Ca' Foscari University of Venice, achieving a resolution of 0.4 cm along the ice core depth in a discrete mode through raster scanning and further tested on ice standards and ice core samples.

Although LA-CRDS is still in the development stage for high-resolution water isotope measurements in ice cores, this study establishes foundational concepts and defines pathways for further research aiming at continuous, high-resolution isotopic analysis of long ice core records. Once fully operational, this method could provide a promising alternative to traditional continuous flow techniques that rely on melting and vaporizing ice samples. Ultimately, the LA-CRDS approach will facilitate the study of diffusion processes and improve temperature reconstructions, particularly for deep ice cores.

Resumé

Denne afhandling præsenterer en ny prøveudtagningsmetode til iskerner, specifikt designet til analyse af vandisotoper ved at koble laserablation (LA) med Cavity Ring Down Spectroscopy (CRDS). Laserablations destruktive natur i mikro størrelse muliggør høj rumlig opløsning og minimalt forbrug af prøver, hvilket henvender sig til udfordringerne ved at opnå høj nøjagtighed og præcision i målinger af vandisotoper fra de ekstremt tynde lag ved bunden af dybe iskerner, såsom den Beyond EPICA - Oldest Ice Core-projektet arbejder med.

To forskellige laserablationssystemer blev anvendt i denne undersøgelse. Det første system er et specialfremstillet system dedikeret til studier af vandisotoper i iskerner, mens det andet system bruger en kommerciel LA-opsætning koblet med en CRDS-analysator, der fungerer som en proof of concept for den foreslåede metode.

Det første system omfatter en femtosekund (fs) laser, der opererer ved 1030 nm med en åben-designet ablationskammer, der kan scanne iskerneprøver op til 55 centimeter i længden. Dette system blev oprindeligt designet ved Is, Klima og Geofysik (PICE)- Københavns Universitet, og dets udvikling er blevet fremskredet som en del af denne afhandling. Testmålinger er blevet udført på alle kritiske komponenter, der bidrager til funktion af et fremtidigt LA-CRDS-system, inklusive laserfokusering, gasflowdynamik og design af ablationskammeret sammen med detaljeret karakterisering af krater for at forbedre forståelsen af ablationsprocessen i is. Disse test giver indledende indsigt i systemets ablations ydeevne.

Det andet system er en kommerciel laserablationsopsætning, der består af en ArF nanosekund (ns) laser, der opererer ved 193 nm og et integreret lukket-design to-volume ablationskammer, der kan rumme prøver op til 5 centimeter i længden. ns LA-systemet blev koblet med en CRDS vandisotopisk analysator ved Ca' Foscari University of Venice hvilket opnåede en opløsning på 0,4 centimeter langs iskernedybden i en diskret tilstand med raster scanning og har yderligere testet på is standarder og iskerneprøver.

Selvom LA-CRDS stadig er i udvikling til højopløselige målinger af vandisotoper i iskerner, etablerer denne undersøgelse grundlæggende begreber og baner vejen for yderligere forskning med henblik på kontinuerlig, højopløselig isotopisk analyse af lange iskerne registreringer. Når metoden er funktionsdygtig, kunne den tilbyde et lovende alternativ til traditionelle kontinuerlige flowteknikker, der er nødt til at smelte og fordampe isprøverne. Endelig vil LA-CRDS-tilgangen fremme studiet af diffusionsprocesser og forbedre temperaturrekonstruktioner, især for dybe iskerner.

Acknowledgements

First, I would like to thank my supervisor, Vasileios Gkinis, for his help and guidance throughout my PhD, as well as for his expertise and valuable feedback during my work. Second, I want to thank my supervisors Dorte Dahl-Jensen and Carlo Barbante, for their for in supporting the broader context of this research. I am also grateful to Bo Vinther for always being available to offer help whenever it was needed. I am thankful to Barbara Stenni for her support and insights throughout this work. I want to offer a special thanks to Pascal Bohleber for his constant presence and support in tackling challenges and moving my research forward. I would also like to thank Yang Zhang, Aslak Grinsted, and Wolfgang Müller for being part of my evaluation committee and for taking the time to read and evaluate my work.

Thanks to all the colleagues and PhD fellows at NBI and University of Venice. Thank you, Daniele Zannoni, Ciprian Stremtan, Rémi Dallmayr, Piers Larkman, and Nico Stoll for all the help when conducting experiments in Venice. Also thank you, Isa Hendricks, Johanna von Drachenfels and Simon Fassel for helping build the system in Copenhagen.

I further would like to thank each one of the PhD students from the DEEPICE program; our conversations and time spent together made this a truly memorable PhD experience. Special thanks to Marie Kazeronie for all the help throughout the project, and to Amaëlle Landais and François Fripiat for their support during challenging times.

I'm deeply grateful to my friends Alkis, Dimitris, and Christos for their support. No matter the time of day, they were always there to answer my scientific questions, entertain my ideas—both wild and sensible—and helped bring clarity to my thoughts. Thank you to Zoe for being part of this journey and for turning every single moment—even the tough ones—into something to laugh about. My deepest thanks to Agnese for her support and all the ways she made this journey better. Thank you, Lili, Alexandra, Georgia, Sophia, Eleni, Giannis, Giorgos, Aris, Manolis, Annika and everyone else whose presence made a difference. Thank you, Christos for your patience and for always supporting and growing with me every step of the way. Finally, I want to offer a big thanks to my parents, Afroditi and Nikos, and my sister, Antonia, who have been my greatest source of strength and support.

Contents

Preface	iii
Abstract	v
Resumé	vii
Acknowledgements	ix
1 Aim and Structure of the Thesis	1
2 Water Isotope Paleoclimatology	5
2.1 Stable Water Isotopes	5
2.1.1 Fractionation Processes	5
2.2 Polar Ice Cores	6
2.2.1 Water Isotope Climate Signal	6
2.2.2 Diffusion	8
2.2.3 Thinning	9
2.2.4 Deep Ice Cores	9
2.3 Water Isotope Measurement Techniques	10
2.3.1 Water Isotope Analyzers	10
IRMS	10
CRDS	11
2.3.2 Ice Sampling Methods	14
Discrete Analysis	14
Continuous Flow Analysis (CFA)	14

2.3.3	New techniques	15
3	Laser Ablation	17
3.1	Laser - Matter Interaction	17
3.1.1	Laser Pulses	17
3.2	Laser Ablation	18
3.2.1	Pulse duration regimes	18
3.2.2	Incubation Effect	20
3.3	Material Removal	20
3.4	Laser Ablation in dielectric materials	23
3.5	LA sampling	24
3.6	Laser Ablation on ice cores	26
3.6.1	LA-ICP-MS	26
3.6.2	LA-CRDS	26
4	fs LA - CRDS	27
4.1	LA-CRDS Experimental Setup	29
4.2	Laser Ablation Optical Configuraiton	30
4.2.1	Optical Table	30
4.2.2	Focusing System	31
4.2.3	LA on ice	34
4.3	Cryo Cell	35
4.3.1	Introduction	35
4.3.2	Mechanical Translation	35
4.3.3	Gas Flow System - Optics Enclosure	36
	Water Vapour Concentration	38
4.3.4	Cryo Cell System Performance	41
	Temperature - Humidity Tests	41
4.3.5	Discussion and Outlook	46

4.4	Crater Characterization	48
4.4.1	Introduction	48
4.4.2	Artificial Ice Preparation	48
4.4.3	Imaging Systems	50
	Optical Microscopy	50
	Macro - Photography	50
	Image processing - Focus Stacking	52
4.4.4	Crater Morphology and LA Parameters	52
	Metal Target	52
	Glass slide	55
	Artificial Ice Target	57
	LA Groove on ice	61
4.4.5	Discussion and Outlook	64
4.5	Ablation Chamber	66
4.5.1	Introduction	66
4.5.2	Water Vapour production by fs LA on ice	66
4.5.3	Ablation Chamber Design	70
4.5.4	Discussion and Outlook	74
5	ns LA - CRDS	75
5.1	Paper published in Analyst	75
6	Conclusions and Outlook	91
A	Laser Beam Characterization	95
A.1	Laser Beam profiles	95
	A.1.1 Gaussian Beam	95
	A.1.2 Bessel Beam	96
A.2	Optical Elements	98

A.3	Beam profiling	100
A.3.1	Laser Beam Size	100
B	Temperature-Humidity Module	109
B.1	Arduino Code for Temperature Humidity Sensors	109
C	Crater Characterization	113
C.1	Protocol for Laser Focusing	113
C.2	Macro Photography	114
C.2.1	Crater Diameter Measurement Tool	114
C.2.2	Macro Photography System	117
D	Publications	119
D.1	Past Global Changes Magazine	119

List of Figures

2.1	The transport of a water mass from the subtropics to its deposition in polar regions.	7
2.2	Interval of the Site E ice core showing $\delta^{18}\text{O}$ measurements and diffusion-corrected data. Volcanic reference horizons in the Electric Conductivity Measurement (ECM) signal were used to guide the dating of the core. (Bo M. Vinther - Master Thesis)	9
2.3	Schematic representation of a Cavity Ring-Down Spectroscopy (CRDS) setup (left) and photodetector signals (right), showing decay rates under gas-present and gas-absent conditions.	13
2.4	Spectrum acquisition process showing detector signal over time (top) and its correlation to light loss as a function of wavelength (bottom), where intensity is proportional to the isotopic ratio.	13
2.5	Schematic diagram of the CFA-CRDS system. [Gkinis et al., 2011]	14
3.1	Schematic of laser-induced damage on the material (top) indicating diameter, d , of the ablated area, corresponding Gaussian fluence profile along the x -axis (bottom), and a 3D representation of the fluence distribution, highlighting the threshold fluence.	20
3.2	Laser Beam - Matter Interaction for a) short and b) ultra-short laser pulses. [Leitz et al., 2011]	21
3.3	Schematic showing precision in metal machining as a function of laser pulse duration. [Breitling et al., 2004]	21
3.4	Typical energy dissipation pathways and phase transformations occurring after material excitation by an ultrashort laser pulse. [Shugaev et al., 2016]	22
4.1	Absorption coefficient of ice across different wavelengths from UV to IR, highlighting the specific wavelength used for laser ablation in various ice core studies.	28

4.2	Laser ablation setup at the University of Copenhagen including high energy fs pulsed-Laser (1), reaching a mirror (2) mounted in the optical rail inside the freezer where a focusing system, enclosed in the cover box (3), directs the beam onto the ice surface placed in a holder (4), mounted on the linear translational stage (5). The ablation chamber (6) and the CRDS analyzer (7) serve for sample collection and water isotope analysis respectively.	29
4.3	Optical Configuration on the Optical Table including the path of both alignment and IR laser beams. (Adapted from [Peensoo, 2024] with minor modifications.)	30
4.4	Beam profile of IR laser beam (1030 nm).	32
4.5	Beam profile of IR laser beam (1030 nm) focused with a plan convex lens (f: 100 mm).	32
4.6	Laser fluence as a function of pulse energy for various optical configurations. The solid lines represent standard configuration by the use of a planoconvex lens, while the dashed lines indicate the addition of a beam expander (3X). Each line is annotated with specific spot sizes and depths of focus (DOF) at various pulse energies	33
4.7	Laser beam focusing optical configurations for LA.	34
4.8	Optics Enclosure mounted on the aluminum frame.	37
4.9	Optical elements of the LA focusing system mounted on the optical rail placed inside the optics enclosure.	38
4.10	Relative humidity and H ₂ O concentration measured at 19 °C (top) and −14 °C (bottom) over time using both DHT22 sensors and the CRDS analyzer.	40
4.11	DHT22 sensors placed inside the optics enclosure and in the freezer area for monitoring humidity and temperature. Stainless steel tube interfacing the CRDS instrument is placed above the ice surface.	41
4.12	Water vapour and temperature measurements across three consecutive days. The full temporal profile a) shows water vapour concentration obtained using four DHT22 sensors and CRDS-PICARRO, and temperature conditions (DHT22) influenced by dry air and freezer settings as well as ice presence and ablation processes. b) provides a zoomed-in view of Day 3 processes. Ice was left in the freezer overnight.	43
4.13	Water vapour and temperature measurements across three consecutive days. The full temporal profile a) shows water vapour concentration obtained using four DHT22 sensors and CRDS-PICARRO, and temperature conditions (DHT22) influenced by dry air and freezer settings as well as ice presence and ablation processes. b) provides a zoomed-in view of Day 3 processes. Freezer was not activated during the night.	45

4.14	Water vapour and temperature measurements across two consecutive days. Water vapour concentration was obtained using three DHT22 sensors and CRDS-PICARRO, and temperature was measured by DTH22 sensors.	46
4.15	Setup for artificial ice production: The system includes an evacuation setup with a cylindrical holder on a magnetic stirrer and heater, connected to a pressure gauge, which leads to a water trap filled with liquid nitrogen. The water trap connects to a vacuum pump. For controlled freezing, a heating tube encases the cylinder in a freezer, enabling gradual freezing over 3 days while the tube ascends, driven by a motor.	49
4.16	Macro-photography setup including motorized rail with a macro tube attached, mounted on a stand. The tube supports the camera at one end and the objective lens at the other. The stand incorporates a XY stage where the sample is placed.	51
4.17	Laser ablation craters formed on stainless obtained under varying pulse energy (μJ) and ablation time (s).	53
4.18	Linear fit of crater square diameter versus laser fluence for determining the ablation threshold and beam waist of the laser beam in stainless steel target, for different N	54
4.19	Plot of the logarithm of NF versus the natural logarithm of N , used to determine the incubation coefficient S from the slope of the fitted regression line. $F_{th}(1)$ can be derived from the intercept.	55
4.20	Laser ablation craters formed on glass slide under varying pulse energy (μJ) and ablation time (s). Crater images were obtained using both the macro system (top) and the optical microscope (bottom).	56
4.21	Linear fit of crater square diameter versus laser fluence for determining the ablation threshold and beam waist of the laser beam in glass slide target.	57
4.22	Ablation craters on artificial ice samples obtained with varying pulse energy values (20 μJ , 25 μJ , 30 μJ) and ablation duration (15 s, 30 s, 45 s, and 60 s). The diameters of the craters are annotated.	58
4.23	Ablation craters on artificial ice samples obtained with varying pulse energy values (30 μJ , 35 μJ , 40 μJ) and ablation duration (15 s, 30 s, 45 s, and 60 s). The diameters of the craters are annotated.	59
4.24	Crater square diameter versus laser fluence for determining the ablation threshold and beam waist of the laser beam in artificial ice target. Linear fit is applied when possible.	60
4.25	Plot of the mutli-pulse threshold fluence $F_{th}(N)$ versus the number of pulses, N , used to determine the incubation coefficient k , the single pulse threshold $F_{th}(1)$ and the saturation fluence $F_{th,\infty}$ can be derived from the fitting parameters.	61

4.26	Ablation craters formed on ice target by fs laser pulses of varying laser energy, 30 - 40 μJ , captured immediately after ablation and two days post-ablation. Imaging: Optical Microscopy	62
4.27	Ablation grooves formed on ice target by fs laser pulses of 40 μJ laser energy with scanning speed 0.2 mm/s. Imaging: Optical Microscopy	62
4.28	Ablation craters formed on ice target by fs laser pulses of varying laser energy, 30 - 40 μJ , captured two days post-ablation. Imaging: Macro-Photography	63
4.29	Ablation groove formed on ice target by fs laser pulses of 40 μJ laser energy with scanning speed 0.2 mm/s. Imaging: Macro-Photography	63
4.30	Ablation characteristics as a function of laser fluence (F_0) and number of pulses. Shown from left to right: total penetration depth, crater diameter, and mass of ablated ice.	69
4.31	Water vapour production (ppm) as a function of laser pulse energy and dry air flow rate during ablation. Ablation time varies from 10 to 60 seconds.	69
4.32	Ablation characteristics as a function of laser fluence (F_0) and scanning speed of the linear stage. Shown from left to right: total penetration depth, crater diameter, and mass of ablated ice.	70
4.33	Initial prototype of the ablation chamber for the fs LA-CRDS system. (a) Top view showing guide rod connections, sample inlet/outlet, and flush air port. (b) and (c) Cross-sectional views illustrating the sealing mechanism and internal structure. (d) Side view with dimensions of the ablation chamber, highlighting the chamber geometry.	72
4.34	Assembly of the ablation chamber positioned under a plane representing the optics enclosure, showing the mounting features for alignment and stability.	73
4.35	3D-printed ablation chamber prototype. (Left) Mounted on the plexiglass enclosure, showing the guide rods and spring mechanism for positioning. (Right) Chamber positioned above a metal target on the linear stage, used for testing.	73
A.1	Propagation and characteristic parameters of a laser beam operating at 1030 nm in the fs regime.	96
A.2	Bessel Functions. [Hecht, 2012]	97
A.3	Axicon Lens System.	100
A.4	IR laser beam spot with 3X beam expander.	104
A.5	Beam profile analysis of the ring shaped beam (alignment laser: 635 nm when moving the plano-convex lens (f: 175 mm) with respect to the imaging system.	105

A.6	Circular beam shape analyzed using python code A.3.	105
A.7	Circular beam shape analyzed using python code A.3 and laserbeam-size package.	106
A.8	Estimated ring radius at each position along the optical axis from the experiment of Fig. A.5.	106
A.9	Ray tracing diagrams illustrating laser beam propagation through different optical configurations, indicating the Depth of Focus (DOF). a) Laser beam passing through a convex lens. (b) Beam profile transformation using an axicon (c) A system of an axicon and a convex lens, illustrating changes in beam profile and extended DOF.	107
A.10	Ray diagram of the optical configuration including a beam expander (3X), an iris diaphragm, an axicon, and a convex lens.	108
C.1	Macro-photography system with LED panels lighting.	117

List of Tables

4.1	Specifications of the Imaging System and Lens Used in the Experiment	52
4.2	Summary of Ablation Parameters for Stainless Steel	54
4.3	Summary of Ablation Parameters for glass slide	57
4.4	Summary of Ablation Parameters for artificial ice target.	60
4.5	Parameters for Water Vapour Production Calculations	67

Chapter 1

Aim and Structure of the Thesis

This PhD thesis introduces an innovative analytical method for measuring water isotope ratios in ice cores. The core of the research lies in developing a micro-destructive sampling technique that achieves the dual goal of obtaining high resolution, high quality data, while at the same time ensuring the preservation of the precious ice core samples. This work was conducted within the framework of the DEEPICE project, integrated into the larger Beyond EPICA initiative, aiming to retrieve the oldest continuous ice core record, extending back to 1.5 million years [Lilien et al., 2021; Chung et al., 2023]. This ice core record will provide insights into Earth's past climate, particularly the Mid-Pleistocene Transition, by delivering the first high-resolution climate records for this period and enabling the investigation of the shift in the glacial cycles behavior from 40000 to 100000-year periodicity and the associated carbon cycle-climate feedbacks [Jouzel et al., 2010].

The analysis of water isotopes in ice cores provides a robust method for reconstructing past temperature variations, as the isotopic composition of precipitation ($\delta^{18}\text{O}$, δD) is directly linked to temperature at the time of deposition as snowfall [Dansgaard, 1964]. This relationship between isotopic ratios and temperature provides a primary method for reconstructing past temperature changes, which can be further validated and refined using alternative approaches like borehole thermometry [Dahl-Jensen et al., 1998] and gas isotope measurements in trapped air bubbles [Severinghaus et al., 1998]. The accurate interpretation of these isotopic archives necessitates the use of sophisticated isotopic models, which simulate the intricate physical processes governing isotopic fractionation. Moreover, a comprehensive understanding of past hydrological changes, including variations in atmospheric circulation patterns, can be achieved by integrating data from multiple water isotopes, including $\delta^{18}\text{O}$, δD , and $\delta^{17}\text{O}$ [Schoenemann et al., 2014].

Molecular diffusion causes a smoothing of the water isotopic signal in ice cores [Johnsen et al., 2000], blurring sharp transitions and obscuring high-frequency variability over time. This inherent limitation on paleoclimate resolution is exacerbated by the physical thinning of annual layers with depth, due to the accumulating weight of overlying ice and the dynamic flow of the ice sheet itself. These combined processes - diffusion-driven signal smoothing and ice flow-driven layer thinning - result in progressively poorer resolution of past climate variability in older, deeper sections of the ice core [Pol et al., 2010]. Therefore, new high-resolution analytical techniques for water isotope measurements are crucial for deriving and interpreting climate records.

Obtaining continuous, high-resolution records from deep ice cores poses significant analytical challenges, requiring both fine-scale sample extraction and the development of tailored preparation protocols that ensure compatibility with the operational constraints of existing water isotope analyzers. Thanks to the unique ro-vibrational transitions of water molecules in the near- and mid-infrared spectral regions that offer a distinct isotopic fingerprint, laser spectroscopy emerged as a powerful tool for precise water isotopic analysis of gaseous samples, driving innovation and expanding the possibilities of isotopic analysis beyond the traditional Isotope Ratio Mass Spectrometry [Kerstel et al., 2008]. Cavity Ring Down Spectroscopy laser-based analyzers are widely used in the ice core community for measuring multiple isotopes, $\delta^{18}\text{O}$, δD , and $\delta^{17}\text{O}$ simultaneously, even outside laboratory settings. Relatively high sampling resolution is achieved when CRDS is coupled with a Continuous Flow Analysis (CFA) ice melting/vaporization system.

This work addresses the critical need for a high-resolution yet precise sampling technique in water isotope analysis in ice cores, that will contribute to signal retrieval and reconstruction of past climate records. While the proposed method, Laser Ablation (LA)-Cavity Ring Down Spectroscopy (CRDS), continues to be refined toward achieving its full potential for high-quality data output, this research establishes a critical foundation for future advancements in the field.

This thesis is structured in the following way:

Chapter 2 introduces isotope paleoclimatology focusing on stable water isotopes, $\delta^{18}\text{O}$ and δD , from deep ice cores for reconstructing past climate. An overview of established ice sampling methods and analytical techniques for water isotope measurements is outlined. Furthermore, the chapter examines the limitations of current approaches and emphasizes the need for novel technological and experimental methods to enhance data resolution, precision, and accuracy.

Chapter 3 outlines the fundamental principles of Laser Ablation, focusing first on the laser-related characteristics and ablation parameters. It then establishes LA as a micro-destructive sampling method and discusses the inherent implications and challenges associated with this technique, such as matrix effects and elemental and isotopic fractionation. Building upon this foundation, the chapter shifts to the application of LA in ice core research. This section offers a review of the established use of Laser Ablation Inductively Coupled Plasma Mass Spectrometry (LA-ICP-MS) for impurity studies in ice cores. Finally, the chapter introduces the novel concept of developing LA-CRDS as a specialized method for high-resolution water isotope studies in ice cores.

Chapter 4 outlines the rationale for developing a femtosecond LA-CRDS system for water isotope analysis in ice cores. This encompasses a detailed description of the LA system, its constituent components, and the testing procedures employed. Post-ablation crater images are analyzed to establish correlations with ablation characteristics. The chapter details the design of the ablation chamber, the controlled environment where the ablated material is generated and captured. Finally, as the femtosecond LA-CRDS experimental setup is still in the development phase, this chapter explores potential advancements and necessary improvements.

Chapter 5 details the development and optimization of a nanosecond LA-CRDS

system for water isotope analysis in ice cores. The system comprises a commercial LA system, equipped with a two-volume ablation chamber, coupled to a water isotope analyzer. The coupling procedure is thoroughly described, with particular attention given to optimizing laser and ablation parameters for efficient production and collection of gas-phase ablated material for water isotopic analysis. A method for producing water isotope ice standards is presented and assessed. The performance of the LA-CRDS system is then evaluated through water isotope measurements of these standards and further tested using an ice core section. Finally, the section details the challenges and limitations inherent to the developed system, focusing on laser-ice interactions and isotopic response. This work concludes by proposing refinements to the ns LA-CRDS system and outlining advancements needed for broader application of LA-CRDS water isotope measurements in ice cores.

Chapter 6 summarizes the development of femtosecond and nanosecond laser ablation systems coupled with CRDS for high-resolution isotope analysis of ice cores. The femtosecond system is still in development, while the nanosecond system has successfully produced water isotopic signals. Key findings include the effects of laser settings on ablation quality and isotopic fractionation, proposing further optimization and validation against established methods suggested. Future work involves improving the technique, potentially by using the fs LA system, which is expected to maximize water vapour production and minimize isotopic fractionation in order to produce high-resolution and high-quality water isotopic signal.

Chapter 2

Water Isotope Paleoclimatology

2.1 Stable Water Isotopes

Oxygen and hydrogen atoms naturally occur in various stable isotopes, ^{16}O , ^{17}O , ^{18}O , ^1H , and ^2H or D (D stands for deuterium) with respective natural abundances of 99.759%, 0.037%, 0.204%, 99.985% and 0.0155% [Mook, 2000]. When these isotopes combine in water molecules, they form different water isotopologues which are molecules that differ in the number or type of isotopes present in their constituent atoms (e.g., $^{16}\text{H}_2\text{O}$, $^{17}\text{H}_2\text{O}$, $^{18}\text{H}_2\text{O}$, and ^{16}HDO). The term "isotopes" is often used for simplicity when referring to isotopologues, and this convention will be followed throughout this thesis.

The concentration of water isotopes are given with respect to a reference sample, using the delta notation, reported in per mil (‰) since the δ values are typically very small in nature:

$$\delta = \left(\frac{R_{\text{Sample}}}{R_{\text{Reference}}} - 1 \right) \cdot 1000\text{‰},$$

where R is the isotopic abundance ratio defined as follows:

$$^{18}R = \frac{^{18}\text{O}}{^{16}\text{O}}, \quad ^{17}R = \frac{^{17}\text{O}}{^{16}\text{O}}, \quad ^2R = \frac{\text{D}}{\text{H}}$$

For water isotopes, R_{Sample} and $R_{\text{Reference}}$ represent the isotopic ratios of the sample and the Vienna Standard Mean Ocean Water (VSMOW) with 2R and ^{18}R at levels of 155.76×10^{-6} and 2005.2×10^{-6} , respectively. The δ values for the water isotopes used in hydrology are denoted as $^{18}\delta$, $^{17}\delta$, and $^2\delta$, commonly expressed as $\delta^{18}\text{O}$, $\delta^{17}\text{O}$ and δD [Mook, 2000].

2.1.1 Fractionation Processes

The mass difference of water isotopes causes slight variations in their physical and chemical properties. More specifically, heavier isotopes have lower mobility leading to lower molecular diffusivity in the air and higher binding energies, which results in lower saturation vapour pressure. H_2^{18}O and HDO with saturation vapour pressure

lower than that of H_2^{16}O evaporate less easily [Mook, 2000]. Condensation, however, favors a higher fraction of heavy water molecules due to their greater tendency to condense compared to lighter molecules. These phenomena are related to isotopic fractionation, defined as the preferential separation of isotopes during physical and chemical processes. There are two primary types of isotope fractionation during phase transitions: equilibrium and kinetic fractionation. Equilibrium fractionation is a reversible process that affects isotope ratios based on their vapour pressures. On the other hand, kinetic fractionation, influenced by diffusion rates, irreversibly depletes heavier isotopes in the phase transition output. These processes shape the isotopic signature of water in different environmental systems, providing insights into the mechanisms governing the distribution and behavior of water isotopes, and ultimately contributing to a more comprehensive understanding of the hydrological cycle.

2.2 Polar Ice Cores

Polar ice cores consist invaluable archives of Earth's paleoclimate, formed through the gradual accumulation and densification of snow over millennia. The ice layers preserve atmospheric constituents within trapped air bubbles and diverse proxy data, including the unique isotopic signature of water molecules. The isotopic composition of water molecules preserved within the ice, specifically the ratio of heavier to lighter isotopes, offers a proxy for past temperatures. The isotopic signature, combined with analyses of atmospheric composition, particulate matter such as dust and pollen, and other proxies, allows for the reconstruction of the Earth's climate history, encompassing temperature variations, greenhouse gas concentrations, and significant environmental events spanning millennia.

2.2.1 Water Isotope Climate Signal

Water, originating from evaporation sources, is transported as water vapour towards the polar regions. During this journey, the air mass carrying the vapour progressively cools, forming clouds. The temperature drop reduces the capacity of the air mass to hold moisture and water condenses out of the air mass, ultimately leading to precipitation, in the form of either rain or snow depending on specific atmospheric conditions. The water vapour is depleted in the heavy isotope while the precipitate is enriched in the heavy isotope. The depletion of heavy water isotopes from both the remaining vapour and newly formed precipitation becomes more pronounced as more water rains out of a cloud. Consequently, when a cloud experiences greater cooling, the δ values for both vapour and precipitation become more negative (Fig. 2.1), reaching their most depleted values upon deposition on the ice sheet [Epstein et al., 1951; Mook, 2000]. This progressive fractionation process, known as Rayleigh distillation, imprints temperature information within the stable water isotopes of the snow precipitation, providing a natural thermometer for probing past climate conditions.

The annual accumulation of snow on ice sheets integrates numerous precipitation events into discrete layers. These layers retain a distinct seasonal resolution in

regions characterized by high annual accumulation rate. The precipitation stored in polar ice caps consists of stable water isotopes that directly reflect the relative depletion of water vapour from its evaporation source to the site of condensation [Epstein et al., 1951; Mook, 2000]. This isotopic composition, preserved in annual layers of ice, establishes a traceable correlation between water isotopic ratios and the temperature at the time of condensation [Dansgaard, 1964] and has been used to infer the temperature of the cloud at the time of condensation [Jouzel et al., 1984; Jouzel et al., 1997; Johnsen et al., 2001]. Ice sheets serve as repositories of past precipitation, preserving stratigraphically ordered archives at various sites in Greenland and Antarctica. Through ice-core drilling [Jouzel, 2013], we can access these archives and retrieve past temperatures imprinted in the water isotopic signals. Each layer of the extracted ice cores represents a discrete period of precipitation. The layered structure is key to unlocking the climate signal trapped within the ice, as it enables the development of ice core chronologies and the subsequent reconstruction of past climate conditions within a temporal framework.

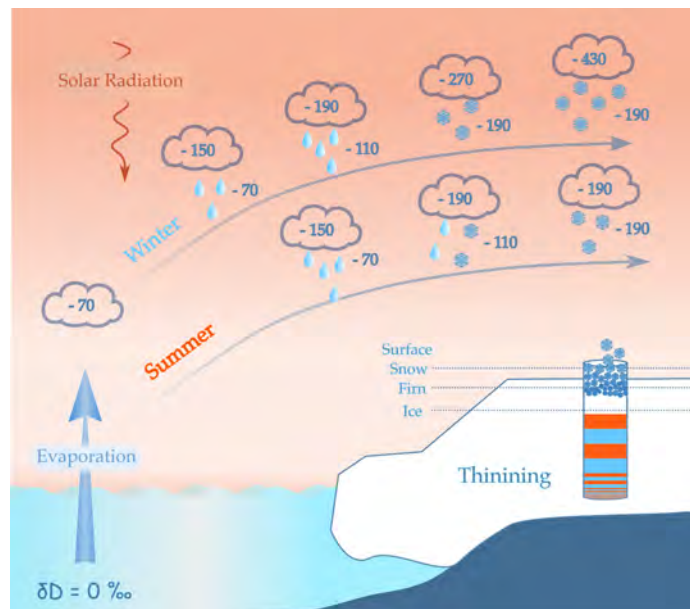


FIGURE 2.1: The transport of a water mass from the subtropics to its deposition in polar regions.

While the $\delta^{18}\text{O}$ and δD values in polar ice cores primarily reflect temperature patterns on the ice sheet, they are also influenced by the temperature of the oceanic moisture source. This dual influence can be disentangled by analyzing $\delta^{18}\text{O}$ and δD together, specifically through the deuterium excess ($d\text{-excess} = \delta\text{D} - 8\delta^{18}\text{O}$) [Dansgaard, 1964; Jouzel et al., 2010]. δD and $\delta^{18}\text{O}$ exhibit different equilibrium fractionation during evaporation, as well as unique kinetic fractionation behaviors and $d\text{-excess}$, which is commonly used as a measure of kinetic fractionation, provides insights into the evaporative conditions under which water vapour originated from the ocean surface, such as evaporation temperature and relative humidity. A strong correlation between $d\text{-excess}$ and the temperature of the evaporation source was reported in [Johnsen et al., 1989]. Variations in $d\text{-excess}$ from ice core records have been used to infer changes in the evaporation conditions at the ocean source from which polar precipitation originated, resolving questions stemming from changes in the location of evaporation sites [Cuffey et al., 2001; Stenni et al., 2004; Masson-Delmotte et al., 2005].

This approach, combined with advancements in analyzing the $\delta^{17}\text{O}$ isotope ratio [Barkan et al., 2005; Steig et al., 2014; Steig et al., 2021], from which the second-order water isotope parameter, ^{17}O excess ($\Delta^{17}\text{O}$) [Miller, 2002; Landais et al., 2008; Luz et al., 2010], is determined, allows for a more comprehensive reconstruction of past climate conditions, particularly humidity at the moisture source. This is because ^{17}O excess is less sensitive to temperature and more influenced by kinetic fractionation, making it especially useful for understanding variations in the hydrological cycle, such as humidity changes during evaporation. By providing complementary information to that obtained from d-excess, $\Delta^{17}\text{O}$ allows disentangling equilibrium and kinetic fractionation during evaporation, thus improving reconstructions derived from water isotope measurements in ice cores.

2.2.2 Diffusion

Water molecules disperse over time smoothing the water isotope signal [Johnsen et al., 2000]. This process, known as diffusion, occurs mainly in firn, but also in the ice matrix [Johnsen, 1977]. Diffusion in firn refers to the movement of water vapour in the porous medium, which has not yet compressed into solid ice. As the firn undergoes densification, the water molecules continue to diffuse, following concentration and temperature gradients, which gradually smooths the high-frequency isotopic signals. This effect of diffusion can be quantified using a metric known as the "diffusion length", which measures the cumulative displacement of water molecules relative to their original position in the firn. The magnitude of diffusion varies with environmental factors such as temperature and accumulation rate, ultimately affecting the isotopic record's accuracy as a proxy for past climate conditions. Once the firn is transformed into ice at the close-off depth, solid-phase diffusion due to isotopic gradients within the ice continues over longer timescales. This process is much slower compared to the diffusion in the firn and mainly becomes relevant in warmer regions of the ice sheet due to geothermal heating. The temperature dependence of the diffusion process enables the use of isotope measurements from ice cores to reconstruct past climatic conditions.

Spectral estimation of diffusion length is used in paleotemperature reconstruction from ice cores. Through spectral analysis, it is possible to estimate the extent to which original isotopic signals have been smoothed due to diffusion. By analyzing the power spectral density (PSD) of ice-core isotope data, the diffusion length can be estimated, which correlates with the past firn temperature conditions [Holme et al., 2018]. The signal restoration at a given depth of an ice core (Fig. 2.2) is performed by a method referred to as back diffusion using the estimated diffusion length [Johnsen, 1977].

It should be noted that the diffusion length estimate should be corrected for additional diffusion processes [Jones et al., 2017a], including sampling diffusion and ice diffusion. In addition, the thinning function of the ice also plays a significant role in the accuracy of the final diffusion length estimate, as it impacts the interpretation of both diffusion and temperature estimates.

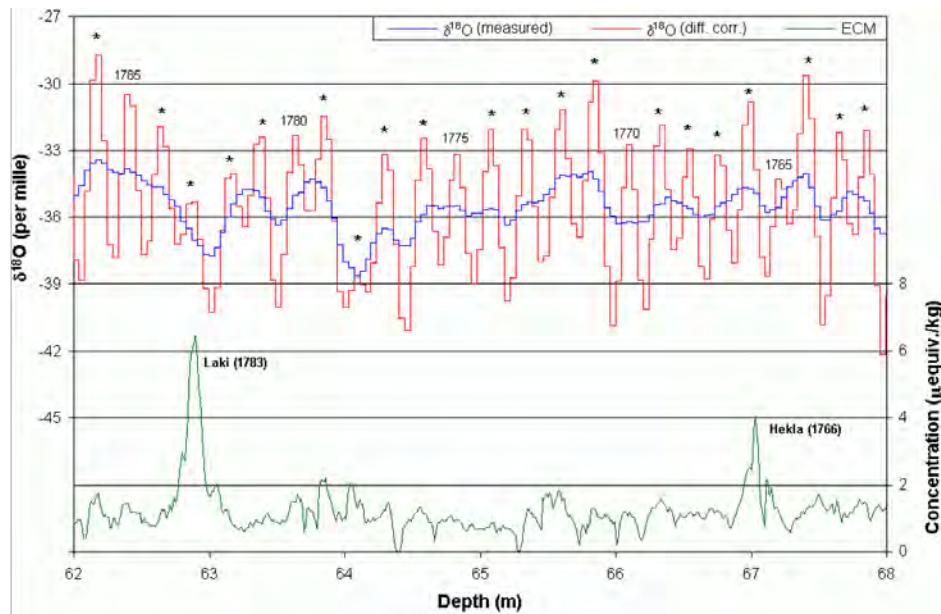


FIGURE 2.2: Interval of the Site E ice core showing $\delta^{18}\text{O}$ measurements and diffusion-corrected data. Volcanic reference horizons in the Electric Conductivity Measurement (ECM) signal were used to guide the dating of the core. (Bo M. Vinther - Master Thesis)

2.2.3 Thinning

The progressive thinning of ice core layers with depth, a consequence of both vertical compression under the weight of overlying ice and horizontal flow driven by gravity, has significant implications for the resolution of paleoclimate reconstructions. While shallower sections often preserve annual to sub-annual climate variability, deeper layers, subjected to millennia of compaction, represent considerably longer time intervals. This temporal averaging, inherent in deeper ice core records, can potentially mask abrupt climate events and hinder precise characterization of past climate dynamics. The thinning function, which models the vertical compression of annual ice layers and depends on ice flow, is crucial for accurately interpreting accumulation rates and water isotope diffusion in ice cores [Gkinis et al., 2014].

2.2.4 Deep Ice Cores

Deep ice core records can extend back hundreds of thousands to several million years, giving a long-term and continuous perspective of climate variability. The oldest ice core drilled to date is from the East Antarctic ice sheet, extracted at the EPICA Dome C site, and it is a continuous record of 3270 meters length that extends back 800,000-years [EPICA Community Members, 2004]. The acquisition of ice exceeding one million years in age represents a pivotal objective within paleoclimatology, as it would encompass the Mid-Pleistocene Transition—a crucial period marked by a shift in glacial cycles from a 40,000-year to a 100,000-year periodicity. Securing and analyzing an ice core record that extends through the Mid-Pleistocene Transition would provide critical data on the processes that influenced changes in Earth's climatic cycles during that time. Deep ice cores allow us to observe changes over

hundreds of thousands to millions of years, providing insight into natural climate variability, the history of greenhouse gases, and the Earth's response to past climate forcings, which is essential for improving the accuracy of future climate predictions.

Ice diffusion processes extend over longer timescales in these deep ice cores, particularly impacting the oldest, deepest layers. The rate of diffusion in these layers increases as the temperature increases due to geothermal heating from the underlying bedrock. Moreover, this effect is intensified over time due to the pronounced thinning of layers caused by ice flow, leading to signal attenuation [Pol et al., 2010].

High-resolution measurements are essential, not only for resolving the water isotope signal in the oldest sections of deep ice cores, but also for improving the diffusion length estimations [Kahle et al., 2018; Holme et al., 2018; Shaw et al., 2024] that contribute to signal restoration as well as temperature reconstructions [Gkinis et al., 2021; Kahle et al., 2021] and the subsequent climate signal interpretation. For instance, continuous-flow analysis (CFA) provides high-resolution datasets [Gkinis et al., 2011; Emanuelsson et al., 2015; Jones et al., 2017b] that allow for more precise identification of the isotopic signal and the noise present in the measurements [Holme et al., 2018]. A high sampling resolution (such as 0.5 cm compared to discrete 5 cm data) leads to a better representation of the noise characteristics and more robust spectral estimation, resulting in a more precise diffusion length estimation.

2.3 Water Isotope Measurement Techniques

The most used analytical techniques for water isotope signal acquisition are Isotope Ratio Mass Spectrometry (IRMS) [Sharp, 2007] and Cavity Ring Down Spectrometry (CRDS) [Crosson, 2008]. The adopted water isotope measurement method is either Discrete Analysis or Continuous Flow Analysis (CFA) [Gkinis et al., 2011]. The latter is commonly used in the ice core research for studying both chemical impurities and water isotopes, and unlike Discrete Analysis is fast and allows the extraction of a continuous water isotope record.

2.3.1 Water Isotope Analyzers

The analysis of stable water isotopes in ice cores is a sophisticated process that involves careful extraction and measurement techniques to ensure precise and accurate results.

IRMS

In the field of water isotope analysis, Isotope Ratio Mass Spectrometry has long served as a standard technique for determining the relative abundance of hydrogen and oxygen isotopes. The limitations of the IRMS technique for water primarily stem from the tendency of water molecules to adhere to the surfaces of the system, so liquid water samples should be chemically converted into gases like carbon dioxide

and hydrogen which are easier to analyze. For $\delta^{18}\text{O}$ analysis, the water is equilibrated with a known volume of carbon dioxide (CO_2) in a temperature-controlled environment. During this equilibration, oxygen isotopes exchange between the water and CO_2 until they reach isotopic equilibrium. The CO_2 , now carrying an isotopic signature representative of the water, is then isolated for analysis [Epstein et al., 1953]. For δD analysis, water is converted into hydrogen gas through reduction reactions using metal reagents such as hot uranium [Bigeleisen et al., 1952], chromium [Gehre et al., 1996] or a platinum catalyst as described in [Huber et al., 2003] using a continuous-flow mass spectrometer that significantly reduces analysis time and errors. The simultaneous measurement of both isotopes, $\delta^{18}\text{O}$ and δD , has been introduced using a pyrolysis furnace for the conversion of water to CO and H_2 combined with continuous-flow IRMS [Begley et al., 1997] [Gehre et al., 2004].

However, the sample preparation and processing required for the chemical conversion of water into a gas molecule compatible with the IRMS analyzer is time-consuming and can compromise both analytical accuracy and system throughput. These limitations, together with the high cost of the instrument, its lack of portability, and the development of alternative methods such as laser spectroscopy in the near and mid-infrared regions, have shifted the focus toward more practical solutions. Laser spectroscopy offers a significant advantage by enabling the direct injection of water vapour into the spectrometer, allowing simultaneous measurement of isotopic ratios like $\delta^{18}\text{O}$ and δD . This approach not only simplifies sample preparation but also provides precision comparable to IRMS systems [Brand et al., 2009] while supporting a portable and user-friendly design.

CRDS

Water, along with other small molecules important in environmental science, exhibits characteristic ro-vibrational transitions in the near- and mid-infrared spectral regions. These transitions are influenced by isotopic substitution, resulting in a unique spectral signature for each isotopologue which can be resolved, under conditions of low vapour pressure and high instrumental resolution. The unique spectral features, assigned to a particular isotopologue and the direct link between their intensities and isotopic abundances, provide a tool for measuring isotopic ratios. This has set the foundation for employing laser spectroscopy in precise isotopic analysis, establishing it as a powerful alternative to traditional mass spectrometry techniques [Kerstel, 2004; Kerstel et al., 2008].

The CRDS technique stands out among direct absorption methods due to its high sensitivity and straightforward experimental setup [Crosson, 2008]. This is achieved by using a high-finesse resonant optical cavity, typically only a few centimeters long, formed by two or more highly reflective mirrors (99.999% reflectivity). The cavity traps the laser light, which undergoes reflections between the mirrors multiple times and increases the effective path length to kilometers. This, in turn, enhances the interaction between the light and the analyte, leading to increased sensitivity for detecting even small isotopic variations. CRDS instruments can also be easily deployed in the field allowing for on-site analysis in remote locations, overcoming the limitations of traditional laboratory-based IRMS instrumentation.

A CRDS analyzer operates by coupling light from a narrow-linewidth laser into a resonant cavity, which bounces back and forth between the high reflectivity mirrors, causing a progressive buildup of intensity until a maximum value is reached. A fraction of the laser light passes through the mirror and reaches a photodetector, which converts the light into a signal reflecting the light intensity in the cavity. The laser light is then abruptly turned off and there is a light 'leakage' from the cavity which arises from losses due to scattering and absorption in the cavity, as well as losses at each reflection from the partially reflective mirrors. The light intensity decays exponentially in time in the cavity. The decay is subsequently monitored by measuring light leaking out of the cavity as a function of time:

$$I(t) = I_0 e^{-\frac{t}{\tau}} \quad (2.1)$$

Given the fact that the absorption inside the cavity is governed by the Beer-Lambert Law the decay constant τ [Berden et al., 2000], commonly referred to as the "ring-down time", is described as follows:

$$\tau(\nu) = \frac{l_c}{c(1 - R + \alpha(\nu))} \quad (2.2)$$

where d is the mirror separation, c the speed of light, R the mirror reflectivity, and $\alpha(\nu) = \sigma(\nu) \cdot n \cdot d$ the frequency dependent molecular absorbance.

The primary measurement parameter in the CRDS technique is the ring-down time (τ), which indicates the photon's lifespan within the optical cavity, taking into account both intrinsic and sample-related losses [Berden et al., 2000]. Ring-down time is inversely related to the optical losses in the cavity, including the effects of molecular absorption at specific wavelengths. In an empty cavity, the ring-down event is described by an exponential decay function of time with a $1/e$ time $\tau(\nu)$ representing the fundamental characteristic of a CRDS system, which is only influenced by the reflectivity of the mirrors and the optical path length between the mirrors. The introduction of absorbing species inside the cavity introduces an additional loss channel and shortens the ring-down time, resulting in a faster decrease of the light intensity. The absorption intensity at a specific wavelength is determined by comparing the ring-down times between an empty cavity and a gas-filled cavity, as shown in Fig. 2.3.

It then follows that the molecular absorption spectrum is obtained by plotting the decay rate $1/\tau$ as a function of frequency.

$$\sigma(\nu) \cdot n = \frac{1}{c} \left(\frac{1}{\tau} - \frac{1}{\tau_0} \right) \quad (2.3)$$

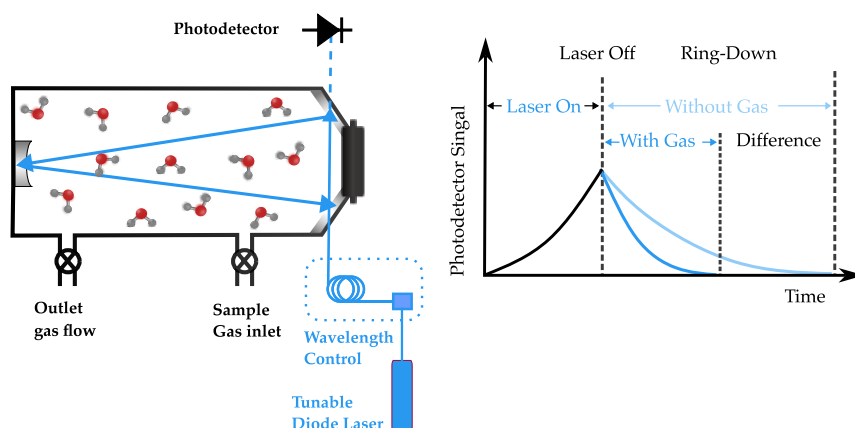


FIGURE 2.3: Schematic representation of a Cavity Ring-Down Spectroscopy (CRDS) setup (left) and photodetector signals (right), showing decay rates under gas-present and gas-absent conditions.

CRDS has evolved to include both pulsed and continuous-wave (CW) lasers [Berden et al., 2000]. The latter, CW-CRDS, offers improved spectral resolution and duty cycle, enhancing the precision of absorption measurements in research applications. The analyzer continuously scans the laser over spectral features of the examined molecule and records the loss and wavelength at each spectral point. Each absorption spectrum is obtained by measuring τ across various emission wavenumbers, ν (Fig. 2.4). The CRDS analyzer employed in this study works in a wavelength scanned mode (WS-CRDS) which further enhances precision by tuning the laser across the absorption features of a target molecule. Instead of physically removing the absorbing gas, the tunable laser is used to scan across both absorbing and non-absorbing wavelengths. By comparing the ring down times at these wavelengths, the absorption characteristics of the target gas are determined.

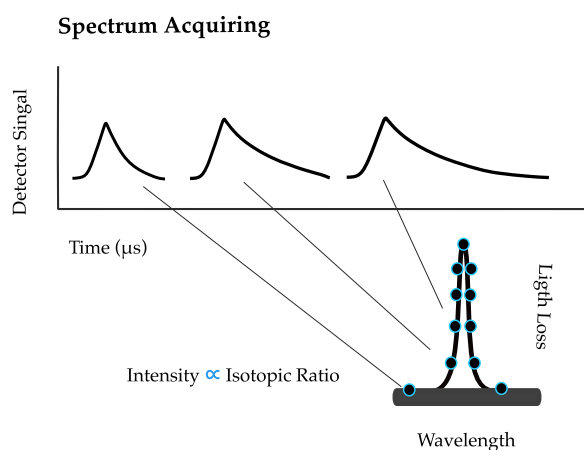


FIGURE 2.4: Spectrum acquisition process showing detector signal over time (top) and its correlation to light loss as a function of wavelength (bottom), where intensity is proportional to the isotopic ratio.

2.3.2 Ice Sampling Methods

Discrete Analysis

For routine water isotope analysis in ice cores, the ice core sections are prepared by cutting them into smaller segments. These segments are subsequently melted, and the resulting meltwater is transferred into vials for analysis. The analysis is performed by a CRDS analyzer, widely used in recent years, which is coupled with an autosampler that introduces the liquid water into a vaporization module directly connected to the analyzer [Steig et al., 2014].

Continuous Flow Analysis (CFA)

Continuous Flow Analysis (CFA) was originally developed to study chemical impurities in ice cores by analyzing continuously melted segments, capturing high-resolution data both in laboratory and field settings [Kaufmann et al., 2008]. Later, CFA was adapted for water isotope measurements in ice cores [Gkinis et al., 2011] obtaining high sampling resolution [Emanuelsson et al., 2015; Jones et al., 2017b; Steig et al., 2021]. Ice core samples are melted continuously using a melthead in a controlled way and the meltwater from the inner section of the ice rod is extracted and analyzed online using a CRDS analyzer, which provides a continuous water isotopic profile of the core. This setup obtains long-term isotopic records and detects fine-scale variations that might be missed with discrete sampling. Depth scale is determined by using an optical encoder attached to a stabilizing weight. Alternatively, depth measurements can be performed using a high-accuracy laser displacement sensor [Dallmayr et al., 2016], that measures the distance to the top of the weight. The flow rates in individual lines can be adjusted by controlling the speed of the peristaltic pumps employed and selecting tubing with varying diameters. A 6-port valve selects between the ice core sample or water standards, used for VSMOV calibration, while another peristaltic pump regulates the water vapour concentration directed to the spectrometer. The sample is injected into a 170°C oven for complete evaporation, with controlled water flow to ensure stable water isotope measurements with the CRDS analyzer.

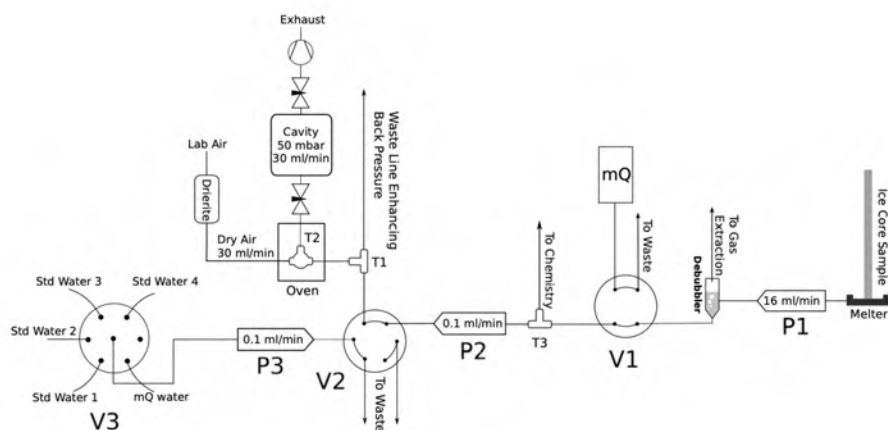


FIGURE 2.5: Schematic diagram of the CFA-CRDS system. [Gkinis et al., 2011]

2.3.3 New techniques

Both discrete and continuous flow analysis for water isotope studies in ice cores require sample preparation which means melting the ice sample, depth control and registration, and vaporization of the liquid sample. However, when layers that belong to the deepest part of the core are to be analysed, their extremely thin nature makes both measurement and analysis of water isotope signal quite intricate and new adopted techniques on water isotopes with high accuracy and precision are needed.

The Laser Melting Sampler described in [Motizuki et al., 2023] offers a new approach to high-resolution water isotope analysis applied to ice core samples. The LMS employs a laser beam, transferred through an optical fiber, to melt the ice within a specially designed silver nozzle. The meltwater produced by laser irradiation is efficiently extracted using a peristaltic tube pump, ensuring minimal isotopic fractionation. The system achieves a depth resolution of 3 mm. The extracted meltwater is then analyzed for stable water isotope ratios using a Los Gatos Research liquid water isotope analyzer.

Laser ablation is an established powerful technique used in various fields and it can also be applied in ice sampling serving a dual purpose: a. direct solid-gas transition and b. use of the smallest amount of sample possible for analysis, given the micro-destructive nature of the ablation process, offering high sampling resolution. In this way, the ice is not melted and the same sample can be used for another type of analysis. A Cavity Ring Down Spectrometer can be used for water isotope signal detection of the ablated mass in the gas phase. This design is expected to allow both fast gas phase sample collection directly from the ice sample and high-quality water isotopic measurements [Malegiannaki et al., 2024].

Chapter 3

Laser Ablation

3.1 Laser - Matter Interaction

3.1.1 Laser Pulses

The temporal profile of the intensity (or irradiance) of a Gaussian laser pulse is described by the equation:

$$I(t) = I_0 \exp\left(-4 \ln(2) \left(\frac{t - t_0}{\tau_L}\right)^2\right) \quad (3.1)$$

where I_0 is the peak intensity for $t = t_0$, and τ_L is the full width at half maximum (FWHM) of the pulse duration.

The spatial intensity distribution of the laser beam is described by:

$$I(r) = I_{\text{peak}} \exp\left(-\frac{2r^2}{\omega_0^2}\right), \quad (3.2)$$

where $I_{\text{peak}} = I(r = 0)$ is the peak intensity at the center of the beam, r is the radial distance from the beam center, and ω_0 is the beam radius, defined as the distance where the intensity falls to $1/e^2$ of its peak value.

The fluence of a laser pulse is defined as the integral of the intensity over time at a fixed point in space:

$$F(r) = \int_{-\infty}^{\infty} I(t) dt \quad (3.3)$$

For a Gaussian laser pulse in time and space, the peak fluence (F_{peak}) and the pulse energy (E_{pulse}) are related based on the pulse width and the beam radius as follows:

$$F_{\text{peak}} = I_{\text{peak}} \tau_L \frac{1}{2} \sqrt{\frac{\pi}{\ln 2}} = \frac{2E_{\text{pulse}}}{\pi \omega_0^2} \quad (3.4)$$

Another key parameter that describes laser pulses is the Pulse Repetition Rate (PRR), which denotes the number of laser pulses emitted per second. The period T between consecutive pulses is inversely related to the PRR [Marks et al., 2022], and can be expressed as:

$$T = \frac{1}{\text{PRR}} \quad (3.5)$$

In ultrashort laser pulses, one of the critical parameters is the peak power, P_{peak} , which quantifies the highest power level achieved at any point in the time domain within the pulse. For a Gaussian pulse shape, the peak power can be approximated as follows:

$$P_{\text{peak}} \approx 0.94 \frac{E_{\text{pulse}}}{\tau_L} \quad (3.6)$$

The ultrashort pulse lasers, with pulse durations in the picosecond (ps) or femtosecond (fs) range, are capable of reaching extremely high peak power, often in the gigawatt range. The average power, P_{ave} , which is the power output averaged across the entire repetition period, is given by:

$$P_{\text{ave}} = E_{\text{pulse}} \times \text{PRR} \quad (3.7)$$

3.2 Laser Ablation

Laser ablation occurs when atoms in a material's surface absorb enough laser energy to overcome their binding energy, causing them to detach from the surface. This energy absorption must exceed a defined threshold, differing from typical evaporation under equilibrium conditions. Lasers that generate long pulse (e.g. nanosecond regime) at lower intensities remove material by sequential heating, melting, and evaporation. Conversely, ultrashort pulsed lasers create a non-equilibrium state, often involving plasma formation, requiring significantly higher intensities, typically around 10^{13} W/cm^2 , compared to nanosecond pulses, which operate at about 10^8 W/cm^2 to 10^9 W/cm^2 [Gamaly, 2011]. A typical threshold fluence for ablation is generally about 1 J/cm^2 .

3.2.1 Pulse duration regimes

In the short pulse regime, the heat diffusion length during the laser pulse, which represents the penetration depth of heat into the material due to thermal conduction, is given by the formula:

$$l_{th} = 2\sqrt{D\tau_L} \quad (3.8)$$

where $D(\frac{k}{c_p\rho})$ is the heat diffusion coefficient [Boardman et al., 1996], τ_L is laser pulse duration, k is the thermal conductivity, c_p is the specific heat capacity, and ρ is the density.

In the ultrashort pulse regime, the thermal diffusion length is typically much shorter than the optical absorption length, meaning that optical absorption primarily determines the heat affected volume during the pulse.

The ablation depth per pulse can be calculated following the equation:

$$L \approx \alpha^{-1} \ln \left(\frac{F_0}{F_{th}^l} \right) \quad (3.9)$$

where F_{th}^l is the ablation threshold fluence and α is the absorption coefficient of the material.

There are two ablation regimes in ultrashort pulse laser ablation [Yang et al., 2007] reported in the literature and both depend logarithmically on the laser fluence [Nolte et al., 1997]. In the lower fluence regime, the density of hot electrons is too low and the heat diffusion is negligible, the ablation depth per pulse is given by equation 3.9, while in the higher fluence regime, there is a significant influence by the electronic heat conduction and the ablation depth can be calculated as follows:

$$L = l_{th} \cdot \log \left(\frac{F_0}{F_{th}^h} \right) \quad (3.10)$$

Liu's method [Liu, 1982] is a straightforward technique for determining both the waist of a Gaussian beam and the fluence threshold (Fig. 3.1) of any material based on the assumption that there is a threshold modification response, which is expressed through the correlation between the threshold modification fluence F_{th} and the diameter \emptyset of the ablated crater following the equation:

$$D^2 = 2w^2 \ln \left(\frac{F_0}{F_{th}} \right) = 2w^2 \ln \left(\frac{E_{pulse}}{E_{th}} \right) \quad (3.11)$$

where the peak laser fluence is defined by:

$$F_0 = \frac{2E_{pulse}}{\pi w^2} \quad (3.12)$$

with E_{pulse} being the incident laser pulse energy.

Combining equations 3.11 and 3.12 we can derive an equation that correlates the crater diameter with the more easy to indentify parameter of laser energy per pulse. Applying a linear fit representing the square diameter of the crater (the ablation modification) versus the logarithm of the pulse energy, the laser spot size as well as the E_{th} can be determined from the slope and the intercept of the fitting line, respectively.

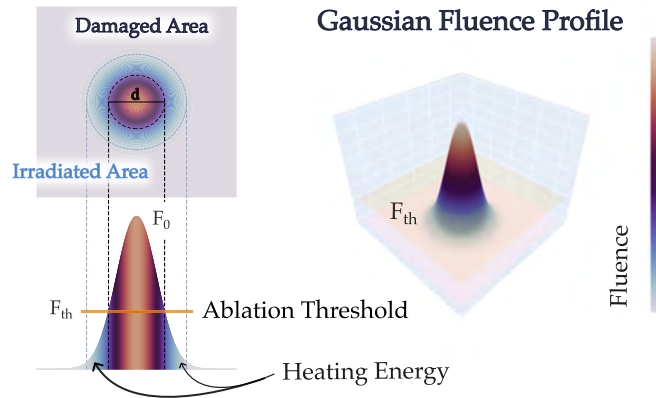


FIGURE 3.1: Schematic of laser-induced damage on the material (top) indicating diameter, d , of the ablated area, corresponding Gaussian fluence profile along the x -axis (bottom), and a 3D representation of the fluence distribution, highlighting the threshold fluence.

3.2.2 Incubation Effect

When multiple laser pulses are delivered to a target specimen, the ablation threshold fluence decreases with increasing pulse number. This phenomenon, known as the incubation effect, arises from material modifications induced by repeated irradiation, making subsequent ablation easier. The dependence of the ablation threshold on incident pulse number (N) is modelled by a power law equation [Jee et al., 1988]:

$$F_{th} = F_{th}(1)N^{S-1} \quad (3.13)$$

where $F_{th}(1)$ is the single-pulse ablation threshold fluence and S represents the incubation coefficient, describing the degree of incubation in the material. When $S = 1$, no incubation is observed, while values between 0 and 1 indicate material softening, with lower values reflecting that the damage accumulation mechanism can reduce the ablation threshold.

3.3 Material Removal

The mechanisms of material removal via laser ablation depend significantly on the pulse duration, ranging from microseconds to femtoseconds, which determines how energy interacts with the material and how efficiently the removal takes place.

For short pulses, typically in the microsecond to nanosecond range, the ablation is dominated by thermal effects (Fig. 3.2). The laser energy propagates through the target material, generating heat and creating a molten layer. This molten material is expelled by recoil pressure, and additional mechanisms such as vaporization or spallation can occur when pressures beneath the molten surface rise. The heat transfer leads to considerable thermal stress, which may cause fragmentation or explosive

boiling, resulting in the ejection of vapour and molten material. The significant heat diffusion into the surrounding areas results in a relatively large heat-affected zone, limiting the precision of the ablation process.

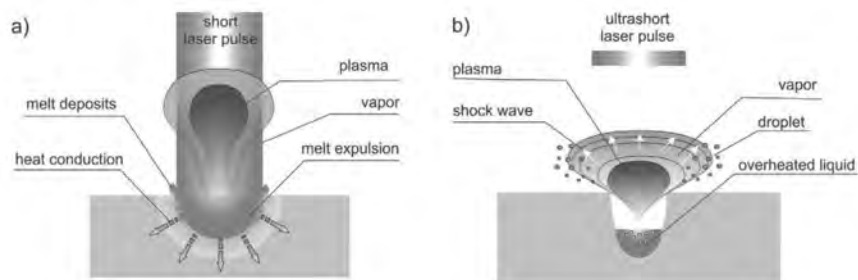


FIGURE 3.2: Laser Beam - Matter Interaction for a) short and b) ultrashort laser pulses. [Leitz et al., 2011]

Ultrafast laser-matter interaction is highly complicated and ablation may proceed through different processes depending on factors related to both the optical and thermal properties of the target material and laser parameters such as pulse width, laser fluence and laser wavelength. An ultra-short laser pulse is characterized by extremely high intensity and the energy deposited through irradiation of the material is highly confined in space and time. For that reason, non-linear phenomena arise, which in turn, lead to a non-thermal laser ablation and well-structured crater formation. Due to the localized thermal process of electrons, fast energy transfers in the material and thermal diffusion in the bulk material is considerably inhibited, reducing heat affected zones, which facilitates high-precision material processing [Chichkov et al., 1996; Breitling et al., 2004] (Fig. 3.3).

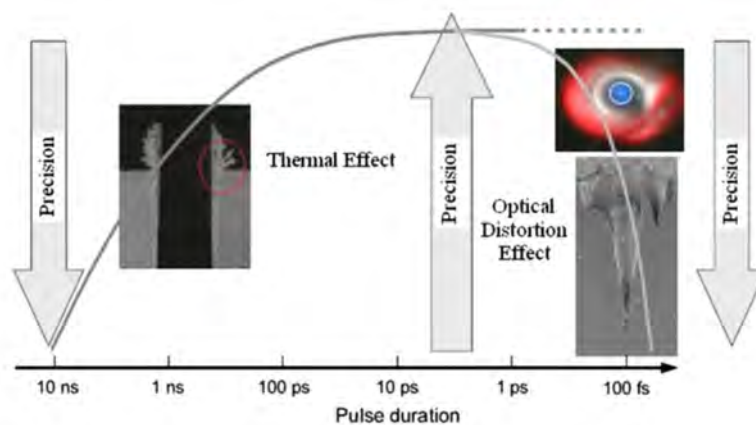


FIGURE 3.3: Schematic showing precision in metal machining as a function of laser pulse duration. [Breitling et al., 2004]

We can define three fundamental processes (Fig. 3.4) [Shugaev et al., 2016], separated in time, that take place during the aforementioned interaction: (a) laser excitation of the optically active electronic states in the illuminated spot and ultra-fast phenomena related to that, plasma formation, non-thermal phase transformation and/or Coulomb explosion (femtosecond - picosecond regime), (b) fast non-equilibrium phase transformations caused by excited electrons-lattice energy transfer resulting to laser induced ablation (picosecond regime), (c) followed by cooling and resolidification of the laser affected area leading to material structural change (nanosecond regime).

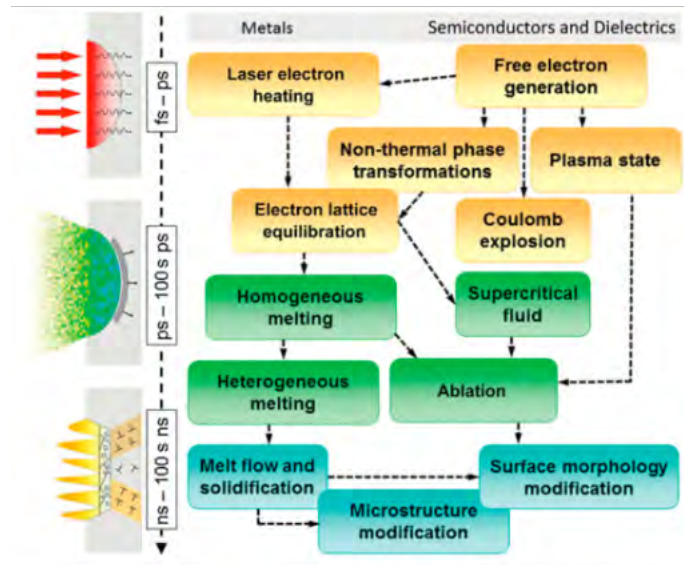


FIGURE 3.4: Typical energy dissipation pathways and phase transformations occurring after material excitation by an ultrashort laser pulse. [Shugaev et al., 2016]

More specifically, ultra-short laser pulses interaction with solid materials requires the presence of free electrons under strong laser excitation conditions as the starting point which leads to ablation and microstructure modification of the bulk material, following different mechanisms for different materials, including metals, semiconductors and dielectrics [Gamaly et al., 2013; Cheng et al., 2013; Mao et al., 2004]. Free electrons, which are present in metal targets, absorb energy due to the inverse Bremsstrahlung effect that may lead to plasma formation. On the other hand, laser excitation of a dielectric surface through free electron transitions to excited states in the bandgap lead to non-thermal phase transformations or even Coulomb explosion due to energy absorption by the excited electrons and subsequent electron emission and charging of the surface. Laser excitation takes place in the femtosecond (fs) - picosecond (ps) regime and phase transitions are observed under the electronically excited state on the sub-ps time scale, without involving electron-phonon equilibration or lattice heating [Shugaev et al., 2016]. In other words, lattice heating occurs on a ps time scale resulting in vapour formation and plasma phases followed by a rapid expansion. In this case thermal conduction in the lattice can be neglected. Relaxation processes, electron-lattice energy transfer, heat diffusion and hydrodynamic motion may happen when the laser pulse is finished. This means that during

the pulse an atomic movement in the irradiated solid area is insignificant and there is no disturbance in the atomic structure.

Depending on the laser fluence, different material removal mechanisms are observed. At lower fluences, rapid stress buildup may lead to the ejection of entire layers of the material, while at higher fluences, superheated material undergoes explosive boiling, leading to violent ejection. Further increases in fluence can result in fragmentation, where the molten material disintegrates into small clusters due to high strain rates. At the highest fluences, vaporization occurs, where the surface of the target is completely atomized, producing a vapour of atoms and small molecules.

3.4 Laser Ablation in dielectric materials

Laser ablation of dielectric materials involves intricate interactions between laser radiation and the material, which differ fundamentally from those observed in metals or semiconductors, as previously mentioned. Dielectrics, being non-conductive materials, exhibit a distinctive response to laser irradiation due to their electronic configuration. When exposed to ultrafast laser pulses, dielectric materials undergo a series of physical processes that lead to material removal, driven largely by nonlinear absorption phenomena [Stuart et al., 1996; Krüger et al., 2004; Balling et al., 2013].

Dielectrics typically lack free electrons in their conduction band, making linear absorption insufficient for significant ablation. However, when subjected to high-intensity ultrafast laser pulses, nonlinear processes such as multiphoton ionization (MPI) and avalanche ionization (AI) come into play, enabling material breakdown. In multiphoton ionization, multiple photons are absorbed simultaneously by a valence electron, providing it with enough energy to transition into the conduction band. Once free electrons are generated, further energy absorption occurs via avalanche ionization, where these free electrons gain energy from the laser field and subsequently ionize additional atoms through collisions.

These ionization processes cause a rapid accumulation of free electrons, leading to the formation of a dense plasma within the focal region. This dense plasma creates strong Coulomb forces that exceed the binding forces of the lattice, ultimately resulting in rapid material ejection. This mechanism, known as Coulomb explosion, is a key pathway for ablation in dielectrics under ultrafast laser irradiation.

Another important aspect of dielectric ablation is the role of thermal effects. When femtosecond laser pulses are employed, the energy is initially transferred predominantly to the electron system, with minimal heat diffusion to the lattice during the pulse duration. This characteristic minimizes thermal damage and results in highly localized ablation, often referred to as "cold ablation" [Mirza et al., 2016]. However, depending on the fluence and pulse duration, localized melting and phase changes can also contribute to material removal.

The dynamics of laser ablation in dielectrics are significantly influenced by laser parameters such as pulse energy, pulse duration, and wavelength. Ultrafast laser

pulses (ranging from femtoseconds to picoseconds) are particularly effective for high-precision micromachining of dielectrics [Breitling et al., 2004], as they allow precise control over ablation depth and produce minimal thermal effects, resulting in clean features without substantial collateral damage. The two regimes of ablation—low and high fluence—exhibit distinct behaviors. In the low-fluence regime, ablation is often characterized by smooth morphology and limited melting, whereas in the high-fluence regime, phase explosion and material fragmentation can occur, resulting in a rougher surface.

These fundamental processes and dynamics make ultrafast laser ablation a promising technique for processing dielectric materials in applications that require high precision and minimal thermal impact, such as LA sampling of ice samples for water isotope analysis investigated in this thesis.

3.5 LA sampling

Laser ablation has long been established as a versatile sampling method in analytical chemistry, used to either analyze the generated light or examine the produced aerosols. The technique facilitates in-situ analysis by converting minute amounts of solid samples into vapour phase constituents—a mixture of vapour and particles—without requiring complex sample preparation or specific size requirements [Russo et al., 1998]. This feature of LA makes it highly adaptable for a range of solid matrices, from biological to geological samples.

Once the ablated material is generated, it requires an ablation chamber for initial collection, followed by efficient transportation through interface transfer lines to an analyzer. The most common analyzers coupled with LA are mass spectrometers, specifically Inductively Coupled Plasma - Mass Spectrometer (ICP-MS) and Time Of Flight - Mass Spectrometer (TOF-MS) [Russo et al., 2002; Burger et al., 2017]. These techniques exploit the aerosol generated from laser ablation, which is introduced directly into the analyzer for chemical analysis, while the ablation chamber is continuously flushed with a carrier gas to maintain transport efficiency.

The generation of aerosols and gas during laser ablation is influenced by several factors, including laser parameters such as pulse duration, energy, wavelength, and repetition rate. The characteristics of the ablated material, such as particle size distribution and aerosol homogeneity, are dependent on these laser parameters [Koch et al., 2008], [Zheng et al., 2017]. For instance, shorter pulse durations, such as those produced by femtosecond lasers, tend to generate smaller and more uniform particles, leading to improved transport efficiency and more reproducible analytical results. Conversely, nanosecond lasers often generate larger molten particles, which can contribute to elemental and isotopic fractionation due to preferential vaporization of certain elements [Hergenröder, 2006; Kuhn et al., 2003]. The vapour phase is typically enriched in volatile components, while the particulate phase contains refractory elements, leading to challenges in accurately representing the bulk composition of the sample in the analysis [Koch et al., 2008]. The efficient generation and transport of these aerosols are critical for maintaining the integrity of the sample's chemical composition. The generation of two separate phases was also reported by [Van Helden et al., 2024]. This study further investigates the two-phase transport of

particulates and gaseous constituents and highlights that laser energy density and wavelength significantly affects the ablation process. Changing the laser wavelength from 193 nm to 213 nm affects how material is distributed between particulate and gaseous phases during ablation. Specifically, at the shorter wavelength, more material remains in the particulate phase, whereas at the longer wavelength, material is more likely to be transported in the gaseous phase.

Fractionation phenomena during laser ablation, due to both the ablation and transport processes, have been extensively studied for both elemental [Kuhn et al., 2003] and isotopic analysis [Kuhn et al., 2007], [Jackson et al., 2003; Zhang et al., 2020] of the aerosol generated using LA as the sampling method and ICP as the analyzer. Matrix effects and calibration procedures [Zhang et al., 2013] have also been thoroughly investigated for LA-ICP-MS to improve analytical accuracy and mitigate biases. However, little is known about the impact of these effects on the gaseous phase (vapour) sampled by LA. The behavior, composition, and transport characteristics of the vapour phase require further research to fully understand and optimize analytical methodologies for comprehensive analysis.

3.6 Laser Ablation on ice cores

3.6.1 LA-ICP-MS

Laser ablation on ice samples was previously used for ice sampling on LA-ICP-MS (Laser Ablation - Inductively Coupled Plasma - Mass Spectrometry) multi-elemental analysis of ice samples [Müller et al., 2011; Sneed et al., 2015; Della Lunga et al., 2017; Spaulding et al., 2017; Bohleber et al., 2020; Bohleber et al., 2021; Poitrasson et al., 2017]. Previous studies mainly utilized nanosecond pulsed lasers, often operating in the ultraviolet (UV) wavelength range. UV radiation has been found to couple effectively with ice, leading to efficient material removal via laser-induced ablation. For effective coupling with the ICP-MS, the ablated material needs to be in aerosol form. In this context, UV wavelengths have been particularly successful for nanosecond laser ablation of ice. IR lasers have been also used for impurities studies [Reinhardt et al., 2001] in ice cores due to the high absorption coefficient of ice at this wavelength [Warren et al., 2008].

3.6.2 LA-CRDS

When LA technique is employed for water isotope measurements on ice samples, there are some specific restrictions that need to be addressed. During the ablation no or minimum melting of ice is expected, while after the ablation, re-condensation of the ablated material should be avoided. The solid ice should be directly ablated into the gas phase, and generation of particulates is important to be prevented or if any of them are produced, they should not travel to the CRDS cavity where the gas phase analysis takes place. Fractionation is, also, one of the main disadvantages that characterize the LA procedure which affects the quality of the recorded water isotope signal. The sample size, also, should be at the standard ice core sample dimensions and the measurements should be done in a continuous analysis mode for achieving high-resolution continuous water isotope profiles, especially for deep ice cores. Taking into account the above restrictions, high power pulsed laser operating at the femtosecond regime used in this study and in [Kerttu, 2021] with a high repetition rate is possible to achieve fine crater formation, with minimal presence of melting, which means that material can be removed through a "cold ablation" procedure, minimizing isotopic fractionation.

Chapter 4

fs LA - CRDS

This chapter explores ultra-short LA as an alternative to traditional melting methods for sampling solid ice for water isotopic analysis, with a particular emphasis on its potential for advancing ice core studies. The application of this technology is driven by the need for high-resolution analysis, particularly in deep ice cores like the Beyond EPICA ice core, retrieved from Antarctica. Deep ice cores constitute a continuous climate archive with the potential for high temporal resolution given that their extremely thin layers at the deepest part of the core can be resolved. The high-resolution sampling that LA offers can unlock this potential by providing high depth and temporal resolution. This is crucial not only for constructing a continuous and detailed water isotope record but also for investigating processes like diffusion and water vein [Pol et al., 2010; Ng, 2023] formation in the deepest sections of the ice core. Understanding these processes, which can obscure climate signals, is essential for accurate signal restoration and interpretation. At the same time, the micro-destructive nature of laser ablation ensures that only the smallest amount of sample required by the detection system is used for analysis, preserving the invaluable samples for further investigation.

However, several challenges need to be addressed to fully realize the potential of LA for water isotope analysis in ice cores. One key aspect is that the ablation process must be carefully controlled to minimize or eliminate ice melting and prevent isotopic fractionation of the ablated material. Another critical issue is the generation of particulates during ablation which should be minimized, and any produced should be prevented from reaching the detection system. Direct ablation of solid ice into the gas phase is essential for maximizing vapour production, which is necessary for compatibility with water isotope analyzers that require gas phase samples. Additionally, this process must be optimized to fulfill the analyzer's requirements regarding the quantity of sample needed for high-quality measurements, while at the same time ensuring high-spatial resolution. Finally, maintaining standardized ice core sample dimensions and employing a continuous analysis mode is crucial for acquiring high-resolution, continuous water isotope profiles from ice core records, while ensuring precise depth control and registration.

High-power pulsed lasers operating in the femtosecond regime with high repetition rates offer a promising tool for addressing these challenges. These lasers enable fine crater formation without melting, effectively achieving "cold ablation" [Mirza et al., 2016], due to minimal heat-affected zones. This minimal heating is expected to significantly reduce isotopic fractionation, ensuring a more accurate representation of the original ice composition. The "cold ablation" regime is well-established

as characteristic for IR lasers when the pulse duration satisfies $\tau_L \leq 10ps$ [Weingarten, 2009]. Also, there is difficulty ablating ice with UV lasers, as shown by the absorption coefficient curve for artificial ice [Warren et al., 2008] in Fig 4.1. However, the role of impurities in natural ice and how they affect laser-ice interactions is not yet fully understood. Femtosecond lasers are less affected by these challenges and can offer a more consistent ablation. Moreover, the amount of ice sample removed during laser ablation with fs pulses in the IR regime should be higher than this estimated for ns laser systems [Müller et al., 2011], which is important for producing enough water vapour for analysis.

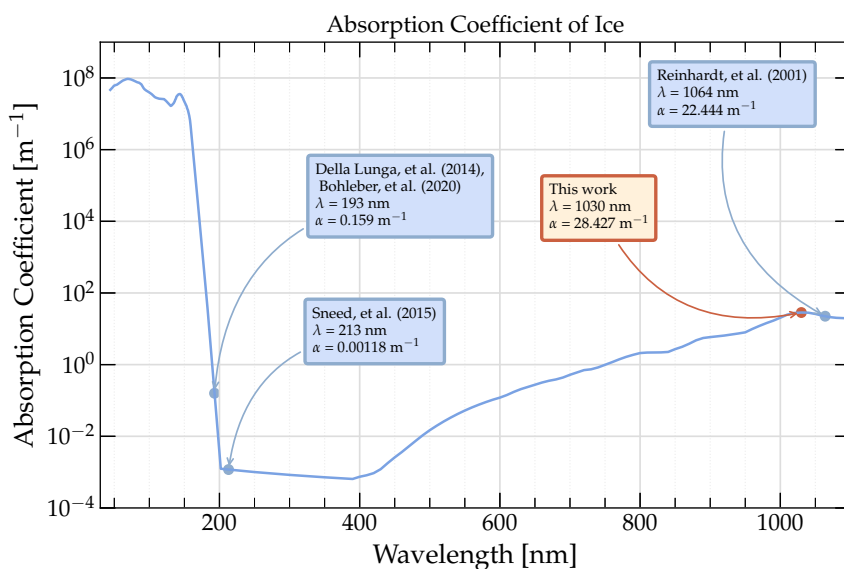


FIGURE 4.1: Absorption coefficient of ice across different wavelengths from UV to IR, highlighting the specific wavelength used for laser ablation in various ice core studies.

Given that Cavity Ring Down Spectroscopy has been widely used for water isotope analysis in ice cores, this chapter proposes a novel method: coupling a CRDS analyzer with a fs LA system, operating at a central wavelength of 1030 nm in the IR region. This approach is expected to generate gas-phase samples directly from solid ice, circumventing the need for melting/vaporization required by traditional ice sampling techniques. Consequently, fast, high-resolution, continuous analysis of ice cores, even at very fine resolutions, should be achievable. This chapter builds on that foundation, focusing on the development and testing of a fs LA system for integration with CRDS. A proof of concept is presented in Chapter 5, demonstrating the coupling of laser ablation with a CRDS analyzer using a commercially available nanosecond LA system.

4.1 LA-CRDS Experimental Setup

The experimental setup [Peensoo, 2024] comprises three basic parts: (a) the LA system, (b) the Cryo-Cell and (c) the detection system which is a Cavity Ring Down Spectrometer for water isotope analysis (L2130-i by PICARRO). The laser ablation system (Fig. 4.2) consists of a femtosecond pulsed laser (1) directing the beam through optical elements into the cryo-cell through an opening. Inside the cryo-cell, which in this setup is a freezer, the beam is reflected by a mirror (2) mounted on an optical rail and focused by a lens system enclosed in a cover box (3). The focused beam reaches the ice sample (4), which is mounted on a linear translation stage (5). Dry air for the gas flow system is introduced into the freezer through a second opening, and the third opening is for the wiring and tubing connected to (7) the CRDS water isotopic analyzer. A simple ablation chamber for sample collection (6) was initially designed as depicted in Fig. 4.2. An improved design of the ablation chamber was constructed and integrated into the system as detailed in Section 4.5.



FIGURE 4.2: Laser ablation setup at the University of Copenhagen including high energy fs pulsed-Laser (1), reaching a mirror (2) mounted in the optical rail inside the freezer where a focusing system, enclosed in the cover box (3), directs the beam onto the ice surface placed in a holder (4), mounted on the linear translational stage (5). The ablation chamber (6) and the CRDS analyzer (7) serve for sample collection and water isotope analysis respectively.

4.2 Laser Ablation Optical Configuration

The fs LA system comprises a femtosecond IR laser mounted on an optical table where optical elements direct the laser beam into the focusing system, which is placed on a rail perpendicular to the sample tray.

4.2.1 Optical Table

The LA system includes two laser sources mounted on the optical table (Fig. 4.3): (a) a high-energy pulsed IR laser (ORIGAMI 10XP by NKT Photonics) with central wavelength at 1030 nm and a repetition rate ranging from 50 kHz to 1 MHz, generating laser pulses in the femtosecond regime with energy values up to 40 μ J and (b) an alignment continuous laser operating at 635 nm and 0.9 mW (Compact Laser Module with a USB connector by Thorlabs). The alignment laser, which is typically lower in power and visible to the eye, was used for preliminary alignment of the optical path before introducing the high-power femtosecond laser to prevent any potential misalignment that could lead to damage to the optical elements [Peensoo, 2024]. The beams from both lasers are aligned using mirrors (M1–M4) and combined at the dichroic mirror (DM), which transmits 97.0% of the 635 nm alignment laser and reflects 98.1% of the 1030 nm IR laser. After alignment, mirrors M5 and M6 direct the two beams through the holes of the protective screen and the freezer to reach the focusing system inside the freezer. Two iris diaphragms facilitate the beams' alignment on the table before entering the freezer.

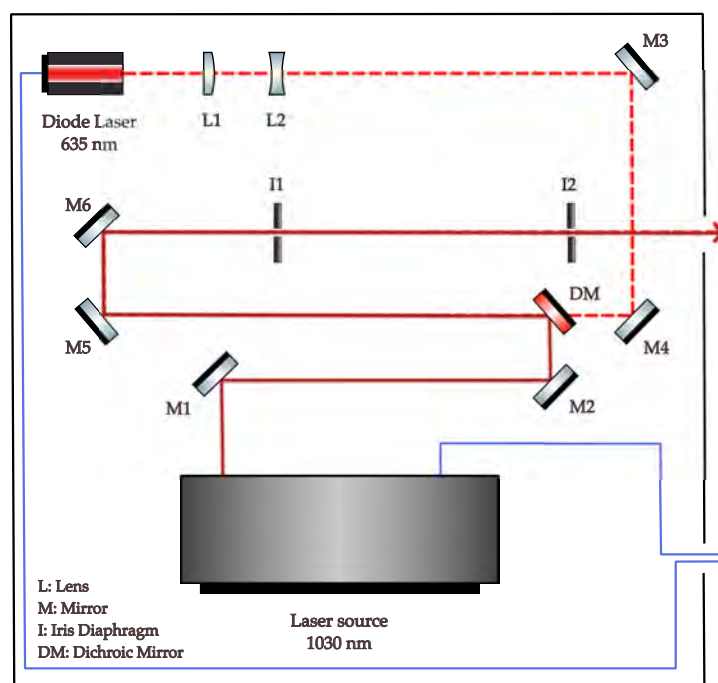


FIGURE 4.3: Optical Configuration on the Optical Table including the path of both alignment and IR laser beams. (Adapted from [Peensoo, 2024] with minor modifications.)

4.2.2 Focusing System

The laser beam that enters the freezer, where the LA process takes place, reaches a mirror which is positioned at a 45-degree angle and directs the laser beam onto the sample surface, after passing through a system of focusing lenses.

Optical configurations were built in order to modify the laser beam size and/or shape exiting from either the fs laser system operating at 1030 nm or the continuous laser source operating at 635 nm and perform simple beam characterization by imaging the beam spot at the focal plane of each optical configuration (the imaging system design was developed with contributions from Isa Hendriks). The IR laser produces pulses of 400 fs duration. The laser has a TEM₀₀ Gaussian beam profile with a beam quality factor of $M^2 = 1.2$ and a maximum power of 4 W. A repetition rate of 50 kHz was selected. The optical elements used for the configurations of the focusing system are plano-convex lenses of varying focal lengths (f: 100 - 200 mm), an air-spaced achromatic doublet (ACA254-200-B, f: 200 mm by Thorlabs) which offers correction for optical aberrations, a 3X beam expander (BE03-1064 3X UVFS High-Power Beam Expander, V-Coated for 1064 nm by Thorlabs) and an 1° angle axicon lens was used (AX251-B - 1.0°, 650 - 1050 nm AR Coated UVFS, Ø1" (Ø25.4 mm) Axicon by Thorlabs).

Light distribution of the laser spot was recorded with a microscope USB camera (BRESSER MikroCamII 5MP HIS Mikroskopkamera) with a CMOS sensor and the acquired images were analyzed using laserbeamsize python package [Prahl, 2021] (The code used can be found in A.3.1). A neutral density filter was also employed with all the optical configurations tested (NE30A-B - Ø25 mm Absorptive Neutral Density Filter, ARC: 650-1050 nm) The pixel size is $3.45 \times 3.45 \mu\text{m}$ and the active area of the sensor is $8.45 \times 7.07 \text{ mm}$. The sensor size should be at least 3 times the largest focused laser spot diameter and the pixel pitch should be 10 times smaller than the smallest beam diameter measured in order to fit within at least 10 pixels. The largest spot diameter measured is about 6 mm when the beam expander was applied, and the tails of the beam were cropped, so we can not trust such a measurement (Fig. A.4). The smallest spot diameter measured is about 55 μm (Fig. 4.5) when the plano-convex lens (f = 100 mm) was applied, which means that the spot diameter fits within 23 pixels and the resolution is high enough to trust the measurement. In Fig. 4.4 the IR laser beam spot size was analyzed and the spot diameter was estimated around 2.5 mm. The alignment laser beam radius (635 nm) was estimated about 3 mm following the same procedure.

An annular beam characterization was performed using a configuration where the main optical element was the axicon lens, to achieve an extended depth of focus (Eq. A.14). Simple ray tracing simulations (Fig. A.9, A.10) were also conducted to evaluate the depth of focus and compare it to that obtained with other optical configurations. However, a more detailed analysis is needed for precise beam characterization in such a system. Preliminary results are provided in A.3 for potential future applications, as the axicon lens configuration was not used further in the experiments presented in this thesis.

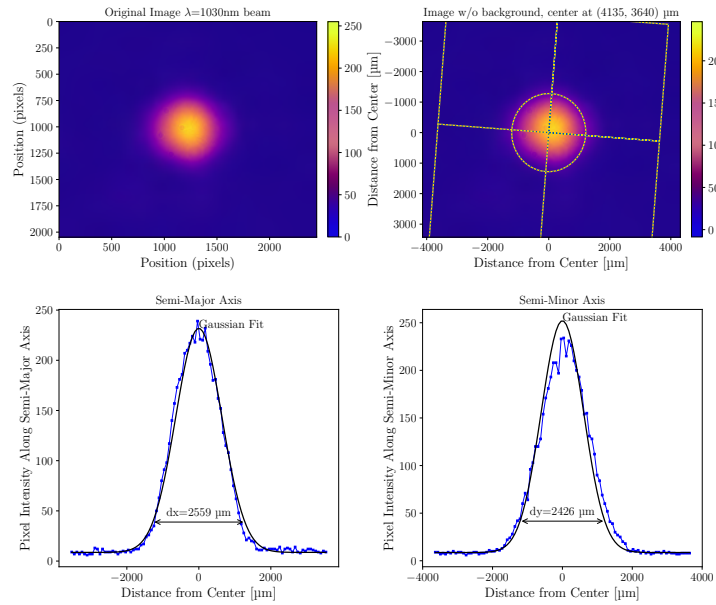


FIGURE 4.4: Beam profile of IR laser beam (1030 nm).

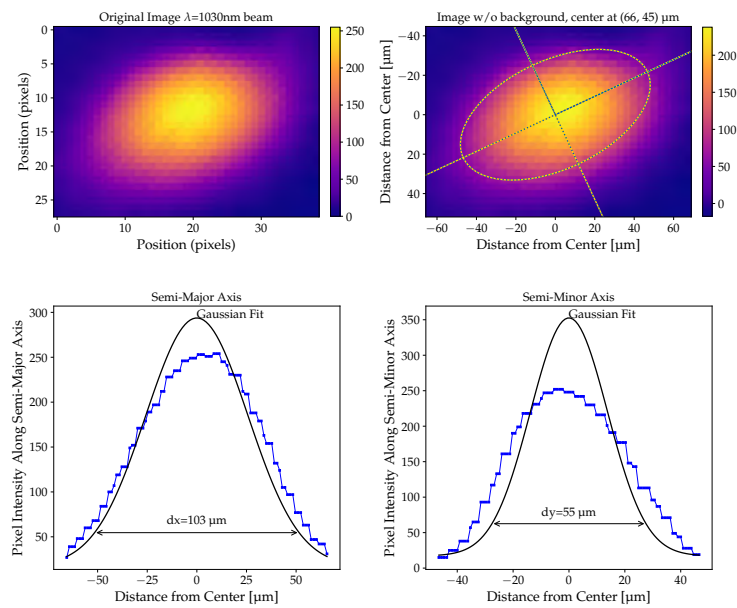


FIGURE 4.5: Beam profile of IR laser beam (1030 nm) focused with a plan convex lens (f: 100 mm).

Figure 4.6 illustrates the relationship between laser fluence and pulse energy of a laser beam (beam diameter: 2.5 mm, wavelength: 1030 nm, M^2 : 1.2) focused using lenses of various focal lengths, both with and without a 3X beam expander. Shorter focal lengths (e.g., 100 mm) produce higher fluence values due to smaller spot size, but this comes at the cost of a shallow depth of focus (DOF), requiring precise alignment for effective ablation. As the focal length increases, the spot size becomes larger (Eq. A.12), reducing fluence (Eq. 3.4), while the DOF increases (Eq. A.13), making the system less sensitive to minor misalignments. The use of the beam expander reduces the spot size for all focal lengths, thereby increasing the fluence. For example, the 200 mm focal length combined with the beam expander results in a smaller spot size, achieving higher fluence than without the beam expander, while still maintaining a practical DOF.

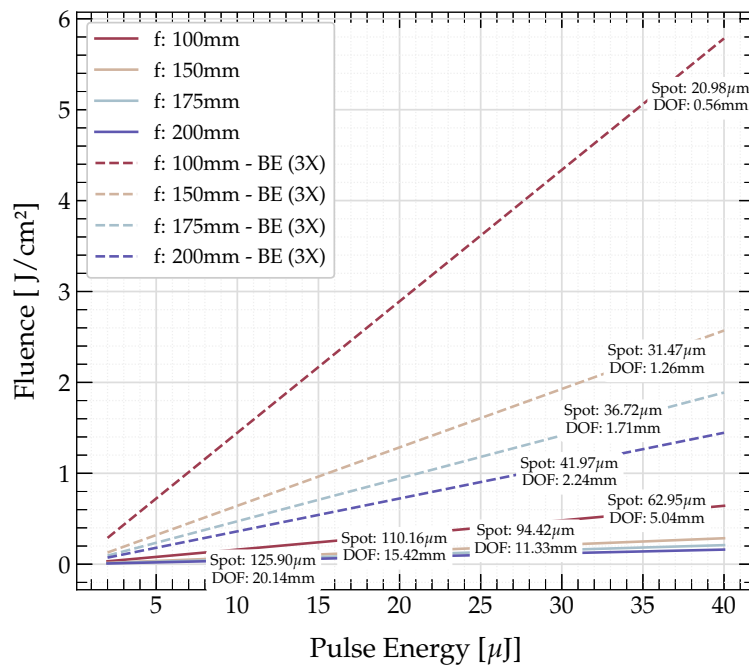


FIGURE 4.6: Laser fluence as a function of pulse energy for various optical configurations. The solid lines represent standard configuration by the use of a planoconvex lens, while the dashed lines indicate the addition of a beam expander (3X). Each line is annotated with specific spot sizes and depths of focus (DOF) at various pulse energies

4.2.3 LA on ice

The selection of the optical configuration for the laser ablation process on ice samples requires the optimization of three parameters: (a) laser spot size: small spot size means high spatial resolution along the sample surface, (b) laser fluence: high values of fluence result on efficient laser ablation of ice sample and (c) depth of focus: large DOF ensures that the ablated material will be insensitive to the examined sample surface anomalies. Two different optical configurations were employed to focus the laser beam in the laser ablation experiments. The first configuration uses a simple plano-convex lens (L) with a focal length of 200 mm, and the second configuration incorporates the 3X beam expander (BE) with either the plano-convex lens or the achromatic doublet (AD) with the same focal length of 200 mm. The purpose of testing these configurations was to investigate the ablation process on different target materials, including metal, glass, and ice, under the simplest possible optical setup that could still yield sufficient ablated material for analysis.

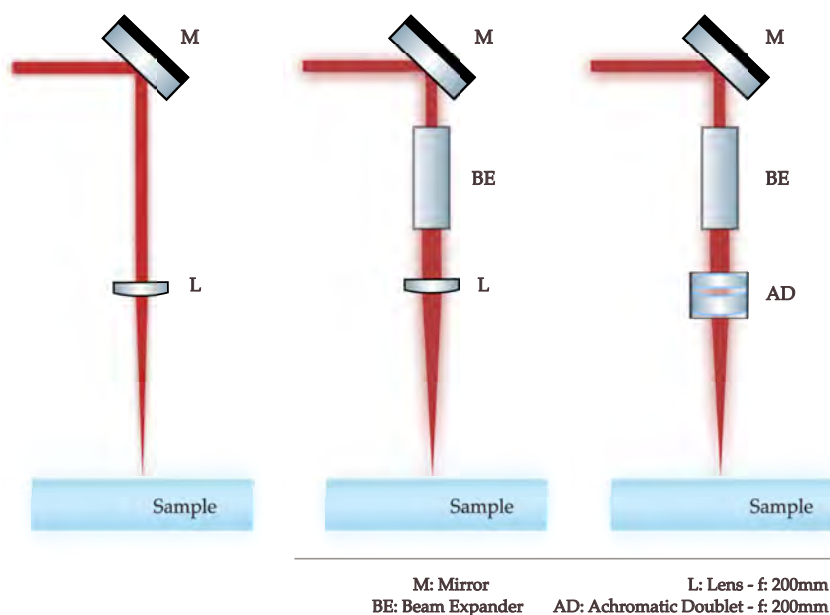


FIGURE 4.7: Laser beam focusing optical configurations for LA.

4.3 Cryo Cell

4.3.1 Introduction

This section provides a detailed overview of the Cryo Cell system designed for fs laser ablation analysis on ice core samples for water isotopic measurements initially developed by [Kerttu, 2021]. The mechanical translation system—including the motorized linear stage and sample holder accommodating standard ice core dimensions was developed by Kerttu Maria Peensoo with contribution from Simon Alexander Munk Wael Fassel, enabling precise sample movement in both discrete and continuous ablation modes. Building upon their work, we further developed the gas flow system and designed an enclosure to enhance control over the environmental conditions affecting the focusing optics, which are placed inside the cryo cell. This ensures optimal performance and stability of the laser system. Achieving low temperature and low humidity in both the freezer and the enclosure is crucial for preventing condensation on the optical components and sublimation of the ice samples during laser ablation. An overview of the gas flow system is provided, along with the testing carried out—including monitoring temperature, humidity, and water vapour concentration using digital sensors and a cavity ring-down spectroscopy (CRDS) analyzer—to optimize operational parameters and improve the system's performance.

4.3.2 Mechanical Translation

The ice sample, with standard dimensions 30 mm × 30 mm × 550 mm, is placed in a sample holder mounted on a motorized linear stage, allowing micro-metric translational movement. The standardized dimensions facilitate the preservation of the sample for subsequent analyses using other analytical techniques. The sample holder consists of a plexiglass tray which is fixed to the stage. The ice sample is secured in the tray, equipped with adjustable plexiglass walls that enable manual, transverse repositioning of the sample. The tray base, mounted to linear bearings and connected via magnetic kinematic seats, ensures consistent positioning and easy removal for sample adjustments or inspections. The stage is secured within the freezer to an aluminum profile frame, which is mounted on wooden plates with bead positioning screws, facilitating detaching and realigning when it is needed.

The operational flexibility of the system is governed by an Arduino-based software that controls both the mechanical translation of the stage and the laser parameters. Both the laser firing and the stage's translational movement are synchronized and controlled remotely through the software. The system allows adjustments in laser parameters such as ablation time, pulse energy, and repetition rate, along with stage movement parameters like distance, speed, and direction. There are two modes of operation:

1. **Discrete Mode:** The number of ablation spots and the distance between them can be selected by the user, allowing for precise, targeted ablation. This laser ablation mode forms distinct ablation craters at each ablation spot.

2. **Line Scan Mode:** This mode supports continuous linear scanning, where parameters such as the travel distance and speed of the stage are predefined. The laser systematically ablates the ice surface creating a groove.

Log files are generated, documenting all operational parameters—including laser and mechanical translation settings such as speed and position. These detailed records are crucial for improving the precision of positional control and depth registration during the analysis of an ice core sample.

4.3.3 Gas Flow System - Optics Enclosure

The freezer in the setup, functioning as an ablation cell, interfaces with the CRDS water isotopic analyzer (L2130-i by PICARRO), which operates using dry air environment. To maintain consistency and ensure accurate measurements, it is crucial that the freezer is also supplied with dry air. This setup minimizes humidity, which is essential during the laser ablation of ice samples. Low humidity prevents sublimation on the ice samples, preserving their integrity for isotopic analysis. Ensuring dry conditions within the freezer is critical not only for protecting the quality of the samples but also for maintaining the operational efficiency of the analyzer.

The dry air unit (AD70L - Air Dryer by Peak Scientific), which incorporates an oil-free compressor (by Jun-Air), delivers dry air through a 6 mm plastic tube that is directly connected to the freezer. An airtight seal is maintained to ensure no ambient air contaminates the internal environment of the freezer. Dry air is pre-cooled by traveling through a coiled section of tubing spanning several meters and placed inside the freezer before entering the freezer. The flow rate of 70 L/min allows the freezer to be fully flushed with dry air in approximately 10-15 minutes. Attached to the outlet of the dry air unit is a flow controller with a one-touch fitting which is equipped with eight adjustable settings, allowing for precise control over the airflow. This is crucial, particularly during extended operations or overnight runs, as it permits the reduction of dry airflow to conserve energy and minimize wear on the compressor. Although dry air is supplied in the freezer, condensation on the optical elements can still occur, and the IR laser beam may scatter, especially when the lid is opened to place or reposition the sample. A cover (Fig. 4.10) that encloses the optical elements that are part of the LA focusing system inside the freezer was built to avoid these issues.

The optics enclosure consists of two basic parts: (a) a metal base plate and (b) a plexiglass box. The metal base plate accommodates the rail where the optical elements are placed. There are small openings in the cover box where 6 mm plastic tubes can be inserted to allow dry airflow in the box, during the measurements. An opening in the box allows the laser beam propagating from the optical table to pass through the box. The beam reaches a mirror that guides it into the sample surface passing through a second opening at the bottom part of the box. Flex metal bellows are inserted in each opening, where adapters with external SM1 threads were adjusted to insert optical windows. There is a free movement of the bellows in the X- and Z- directions before they are tightly screwed that allows the proper alignment of the box opening with the freezer hole, where the laser beam passes. The distance between the bottom part of the box and the sample surface is about 85 mm and the

space between will be used for the integration of a sample collection-transfer system to the CRDS analyzer. Once the enclosure is integrated into the system, the dry airflow from the 6 mm plastic tube connecting the dry air unit to the freezer is divided using a Tee fitting. This fitting attaches to two 6 mm plastic tubes, directing the ends into the enclosure's cover openings. Dry air is introduced into the enclosure via these openings and is circulated within the freezer space through the two openings, which are designed to allow the laser beam to pass through and reach the sample. For further information on installing or removing the enclosure, the reader may refer to the [Optics Enclosure Manual](#).

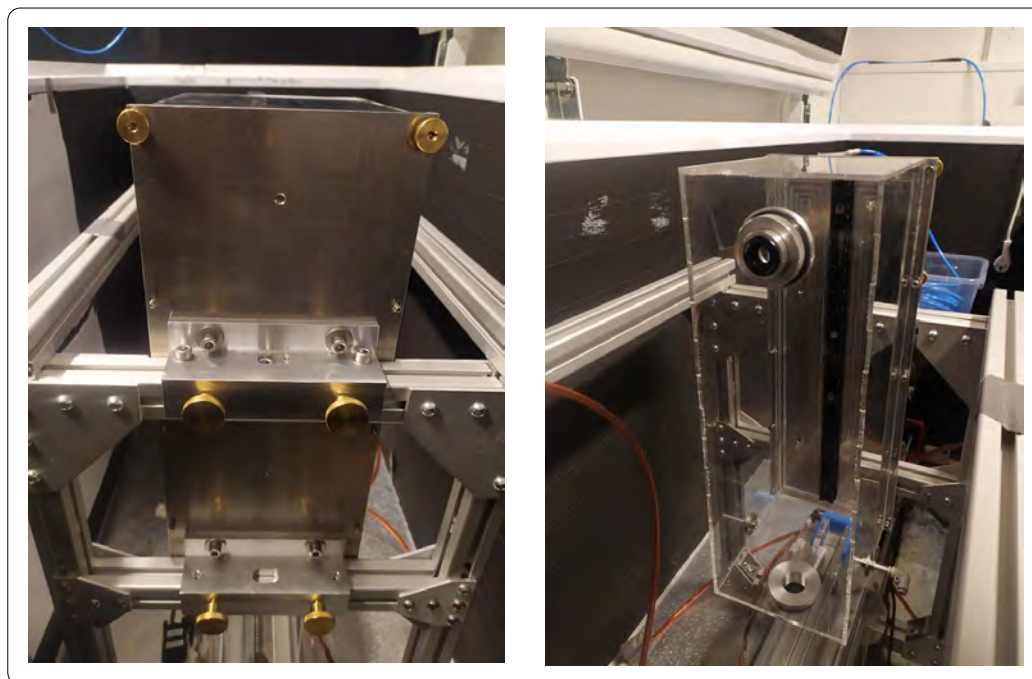


FIGURE 4.8: Optics Enclosure mounted on the aluminum frame.

For the precise vertical adjustment of the focusing lens without disassembling the optics enclosure, which is crucial for maintaining the stability and alignment of the system during experiments, an assembly was created using components purchased from Thorlabs. The system for precise focusing of the lens comprises the PD1/M 20 mm linear stage with piezo inertia drive, the XPCM1/M 30 mm cage system mount, the PD1FM Ø1" optic mount, and the K-Cube controller (Fig. 4.9). The PD1/M 20 mm linear stage is used for its capability to achieve micrometer-level adjustments, which are essential for accurate focusing. The stage is mounted to the XPCM1/M 30 mm cage system mount, integrating it into the optical path while providing flexibility in positioning along the z-axis or x-axis. The PD1FM Ø1" optic mount holds the focusing lens and attaches directly to the linear stage, allowing precise movement of the lens in sync with the linear adjustments. The K-Cube controller, which is placed outside the freezer, drives the PD1/M linear stage, enabling manual or automated control over the movement. This enables straightforward vertical adjustment of the lens to achieve optimal focus while maintaining stable alignment of the optical path. The system's snap-on clamping mechanisms simplify lens adjustments without disrupting the overall setup.

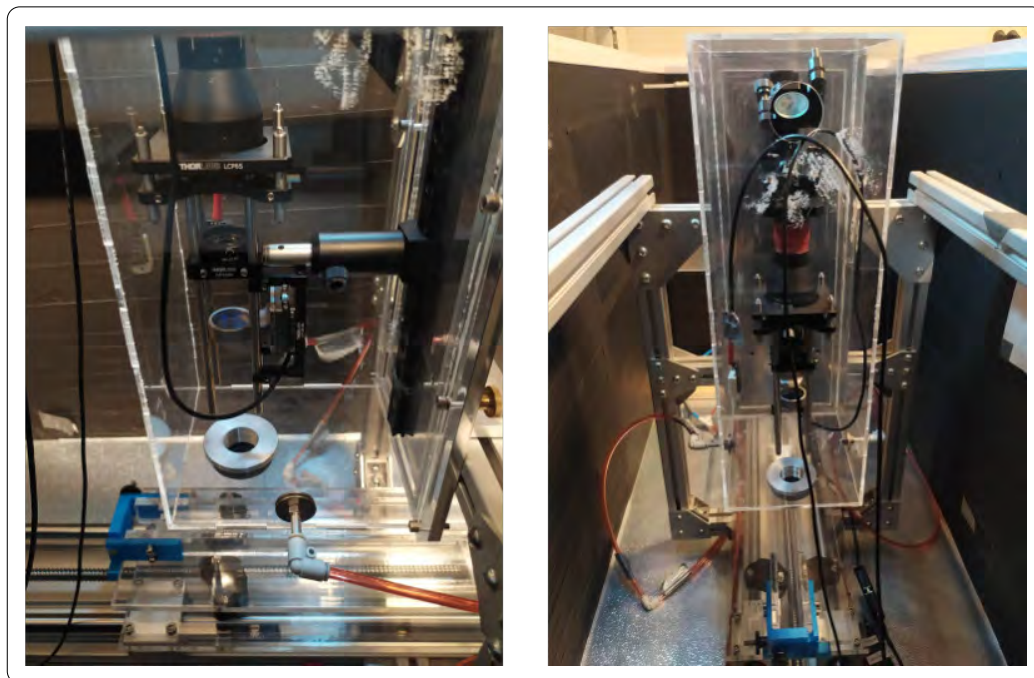


FIGURE 4.9: Optical elements of the LA focusing system mounted on the optical rail placed inside the optics enclosure.

A simple module for measuring relative humidity and temperature was developed to monitor humidity levels inside the enclosure and the freezer. The module features four DHT22 digital sensors for temperature and humidity measurements, an LCD screen for real-time updates, and an SD card reader for data logging, all controlled through an Arduino microcontroller. The Arduino code is provided in [B.1](#).

Water Vapour Concentration

Run tests were carried out in both -14°C and 19°C , using all four sensors of the Relative Humidity - Temperature module, which were placed inside the enclosure, along with a 1/16 inch stainless steel tube interfacing with the CRDS. This tube extends through a hole at the bottom of the freezer, which is filled with small Styrofoam blocks to prevent exchanges with the lab environment and maintain the integrity of the dry air inside the freezer. The objective was to monitor relative humidity, temperature, and water vapour concentration inside the enclosure. Water vapour values were determined using the temperature and humidity measurements and were also directly recorded by the CRDS. Measurements varied air flow rates, employing the 5, 4, and 3 settings of the flow controller.

For the estimation of water vapour concentration in parts per million (ppm) based on temperature and relative humidity, we used two established formulas for calculating the saturation vapour pressure, each applicable to different temperature regimes.

For temperatures between 169 K and 273.16 K, the saturation vapour pressure, p_{ice} , is determined using the equation [Murphy et al., 2005]:

$$p_{\text{ice}} = \exp\left(28.868 - \frac{6132.9}{T}\right), \quad (4.1)$$

where T represents the temperature in Kelvin.

For temperatures above 273.15 K, the saturation vapour pressure, p_{liq} , is calculated using the expression [Murphy et al., 2005]:

$$p_{\text{liq}} = 611.21 \times \exp\left(\frac{17.502 \times (T - 273.15)}{240.97 + (T - 273.15)}\right). \quad (4.2)$$

The vapour pressure p_{vapour} is obtained by adjusting the saturation vapour pressure with the relative humidity (RH):

$$p_{\text{vapour}} = \frac{RH}{100} \times p_{\text{saturation}}, \quad (4.3)$$

where RH is given as a percentage. This is then converted to ppm using the standard atmospheric pressure (101 325 Pa):

$$\text{ppm} = \frac{p_{\text{vapour}} \times 10^6}{101325}. \quad (4.4)$$

The data presented in Fig. 4.10 shows the relative humidity and water vapour concentration measurements at 19 °C and −14 °C over time, obtained using DHT22 sensors and a CRDS analyzer. The humidity and temperature data collected from four DHT22 sensors were averaged and used to calculate the water vapour concentration. At 19 °C, both the relative humidity and water vapour show a rapid decline, stabilizing at low levels. In the first 10 minutes to 15 minutes, the water vapour signal can reach 20 ppm to 100 ppm indicating effective humidity control inside the enclosure. At −14 °C, despite the initial decrease of the water vapour concentration, the system exhibits a different behavior compared to the scenario at 19 °C. The stabilization occurs at higher levels of humidity, indicating a slightly reduced efficiency of humidity control at this lower temperature. The CRDS data shows a higher concentration of water vapour compared to the sensor readings, suggesting that the CRDS may be detecting subtler changes in water vapour that the DHT22 sensors cannot. The difference in readings between the CRDS and the sensors at −14 °C might also point to limitations in the sensors' performance at lower temperatures, or to different environmental dynamics within the freezer that affect sensor readings. However, the humidity baseline can be kept at a low level, which is crucial for the optics' performance. Additionally, the integration of an ablation chamber in the optics enclosure is planned. The chamber, where the ablation processes will take place, will be supplied with the same source of dry air. Maintaining low water vapour concentrations in this system is critical, not only for the detection of subtle water isotope signals produced during laser ablation but also for minimizing condensation.

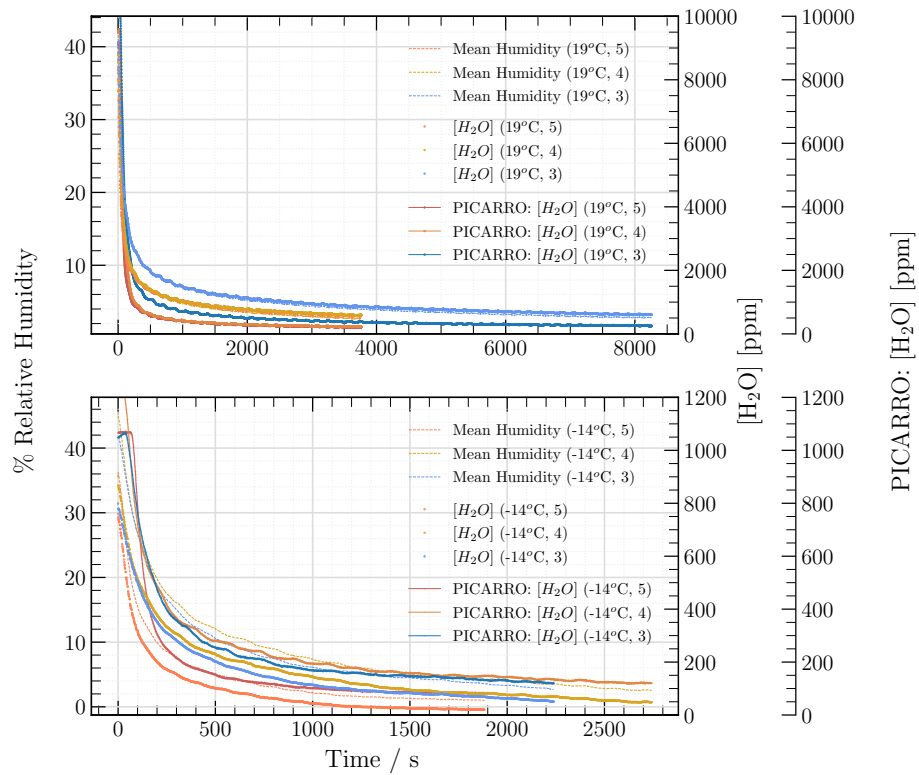


FIGURE 4.10: Relative humidity and H₂O concentration measured at 19 °C (top) and -14 °C (bottom) over time using both DHT22 sensors and the CRDS analyzer.

4.3.4 Cryo Cell System Performance

Temperature - Humidity Tests

To evaluate the environmental conditions inside the freezer under which laser ablation experiments on ice cores are carried out, we designed tests that included monitoring humidity, water vapour concentration, and temperature. Three DHT22 sensors were placed at different positions in the freezer, and one in the enclosure, measuring relative humidity and temperature. These values were then converted to water vapour concentration in ppm. The stainless steel tube reaching the CRDS inlet was placed above the ice sample holder, enabling direct water vapour measurements in ppm (Fig. 4.11). The aim was to replicate the conditions necessary for conducting laser ablation measurements on ice samples. First, the freezer and enclosure were flushed with dry air, and the temperature was subsequently lowered to -19°C . Flushing the freezer with dry air before initiating the cooling process creates a low-moisture environment minimizing the risk of condensation during cooling, as lower temperatures can cause residual water vapour to condense on the surfaces. By preventing this initial condensation, the subsequent drying phase becomes more efficient. Once stable conditions were achieved, the ice sample was positioned inside the freezer for laser ablation measurements. After placing the sample in the freezer, a waiting period is necessary before measurements begin. Opening the lid causes humidity to rise, with the extent depending on the activity—whether simply placing the sample or performing more time-consuming tasks like final checks or focusing. Once the lid is closed, the rate at which humidity decreases again depends on the dry air unit's flow setting. The dry airflow delivery is described in the Gas Flow System Section.



FIGURE 4.11: DHT22 sensors placed inside the optics enclosure and in the freezer area for monitoring humidity and temperature. Stainless steel tube interfacing the CRDS instrument is placed above the ice surface.

In the test measurements shown in Fig. 4.12 a), measurements start with the maximum flow of the dry air unit (setting 8) and it took about 30 minutes to reduce the water vapour concentration from 8000-10000 ppm to 1000 ppm. Subsequently, the freezer was turned on and the dry air unit's flow was reduced to 5 for overnight operation. For the day following, the ice sample was placed in the freezer and left overnight, leading to a rapid increase in both humidity and temperature upon opening the freezer lid. The CRDS recorded the highest humidity level at 2000 ppm, while the sensors inside the freezer registered a maximum of 1000 ppm. The sensor inside the enclosure showed no significant response and quickly returned to the baseline. The humidity readings obtained from the CRDS analyzer were consistently higher compared to those from the DHT22 sensors. After the lid was closed again, the DHT22 sensors recorded a decrease back to baseline levels around 200 ppm (it took 1-2 hours for the environmental conditions to stabilize again at the initial values, with the dry air unit at 5), but the CRDS readings did not show the same behavior. Instead, the CRDS showed higher and fluctuating levels of water vapour (1000-1500 ppm) compared to the initial baseline. This could be due to moisture remaining in the tube or sublimation from the ice adding water vapour, leading to cycles of condensation and evaporation within the stainless steel tube, causing fluctuations in the CRDS readings. During the laser ablation experiments on Day 3 (zoomed-in Fig. 4.12 b)), all sensors recorded an increase in humidity, likely due to additional water vapour introduced by the ablation process and/or sample handling. The CRDS continued to show high values even after ablation ended. The freezer sensors also showed increased humidity levels, which gradually decreased but did not fully return to the baseline, even after a period of more than 2-3 hours, indicating incomplete removal of water vapour.

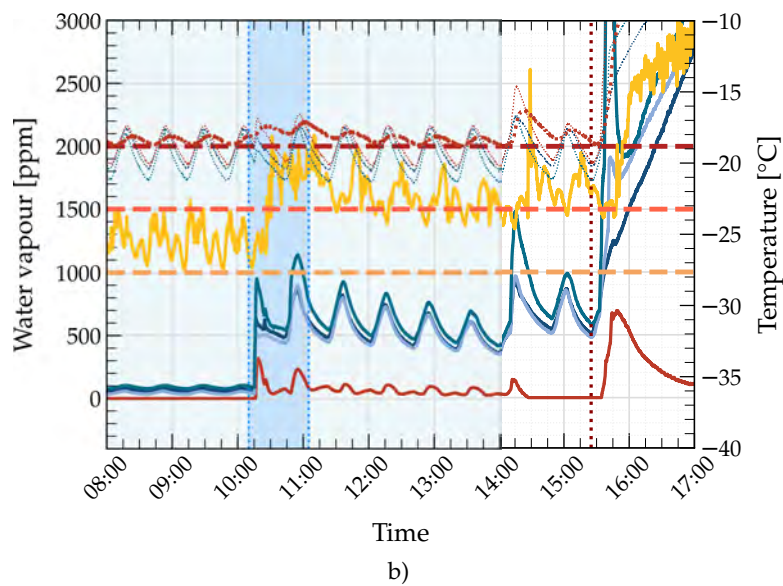
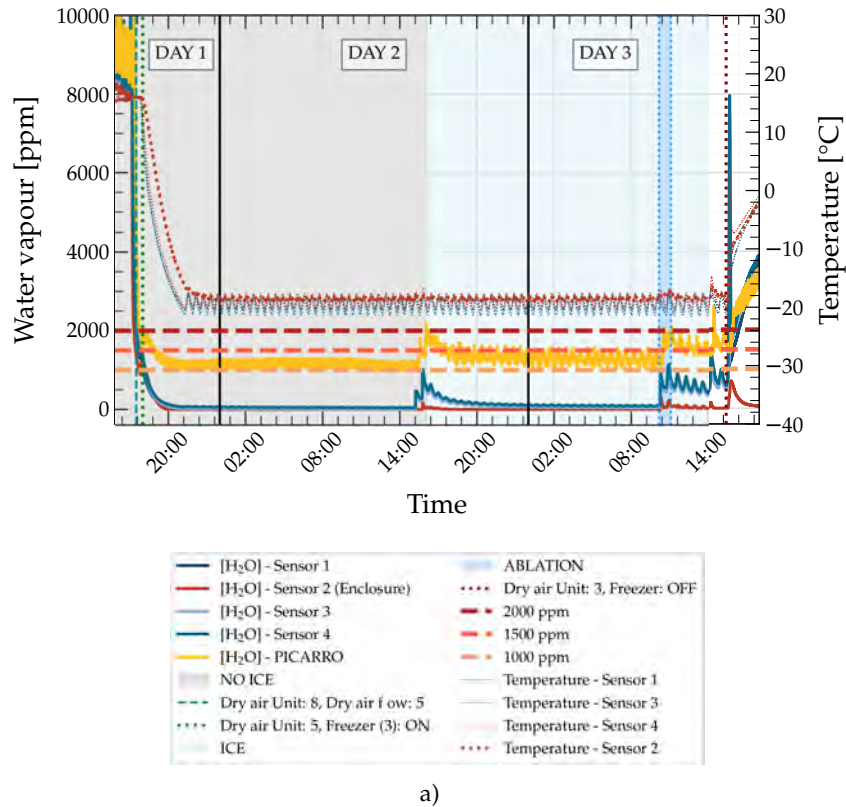


FIGURE 4.12: Water vapour and temperature measurements across three consecutive days. The full temporal profile a) shows water vapour concentration obtained using four DHT22 sensors and CRDS-PICARRO, and temperature conditions (DHT22) influenced by dry air and freezer settings as well as ice presence and ablation processes. b) provides a zoomed-in view of Day 3 processes. Ice was left in the freezer overnight.

In a subsequent series of experiments (Fig. 4.13 a)), the dry air unit was initially set at a flow rate of 4, and the system was left to operate overnight. In this case, the

CRDS and DHT22 sensors in the freezer seemed to record similar trends, unlike the sensor inside the enclosure, likely due to the low flow of dry air. The freezer was then activated early in the morning using a timer, reaching -19°C . Initially, the water vapour concentration decreased, as expected, because colder air holds less water vapour. But, during the temperature stabilization phase the water vapour level began to rise again and exhibited fluctuations, as recorded by all the sensors, with the CRDS recording higher values. This increase and subsequent variability can be attributed to residual water vapour undergoing condensation and sublimation, which the system could not adequately handle. We then increased the dry airflow to setting 8, and the humidity levels began to decrease within about 40 minutes. Afterward, the dry airflow was set to 4, the freezer was turned off, and the system was left running overnight again. The temperature increased to around 15°C , and the humidity followed a similar trend, increasing accordingly as residual water could evaporate more easily. During this phase, the difference between the CRDS and DHT22 sensor readings decreased. However, when the freezer was reactivated the next morning, the humidity levels dropped with the temperature, but the CRDS consistently recorded higher values than the DHT22 sensors. The lowest humidity level achieved was still higher compared to the previous day with a subsequent rising in the humidity during the stabilization phase. To minimize additional humidity, the dry airflow was increased using setting 8, and the freezer was briefly opened to place the sample. In the zoomed-in plot (Fig. 4.13 b)), we observed noticeable jumps in both humidity and temperature when the freezer lid was opened. Both subsequently decreased relatively quickly, though the CRDS showed a slower reduction compared to the DHT22 sensors. Additionally, we ventilated the dry air unit's compressor to remove accumulated water, as approximately 300 ml had collected after 2-3 days of continuous operation. Regular ventilation is recommended to prevent water buildup that can impact the system's efficiency and performance.

When comparing the two experimental series, several factors may explain the differences in humidity levels observed after cooling. In the first experiments, a shorter initial drying period of approximately 30 minutes with a higher dry air flow rate likely reduced humidity effectively, minimizing the risk of moisture reabsorption. In contrast, for the subsequent experiments a lower dry air flow was used for 6-10 hours overnight, resulting in a less efficient drying process. This prolonged flushing may have allowed humidity to accumulate inside the freezer, leading to higher water vapour levels during cooling. The reduced efficiency of the dry air supply may also be linked to water accumulating in the compressor after three days of operation, further exacerbating the humidity levels inside the freezer. Additionally, fluctuations in ambient humidity in the lab environment or other issues connected with the compressor's performance could have further influenced the humidity levels. Together, these factors suggest that achieving stable, low humidity conditions inside the freezer is highly sensitive to the dry air flow, the duration and timing of drying and cooling phases, the ambient environment, and the consistent performance of the equipment.

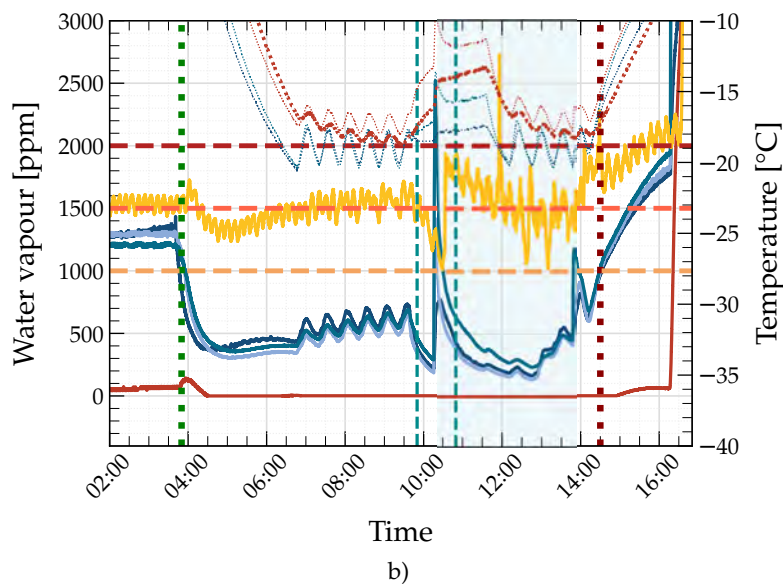
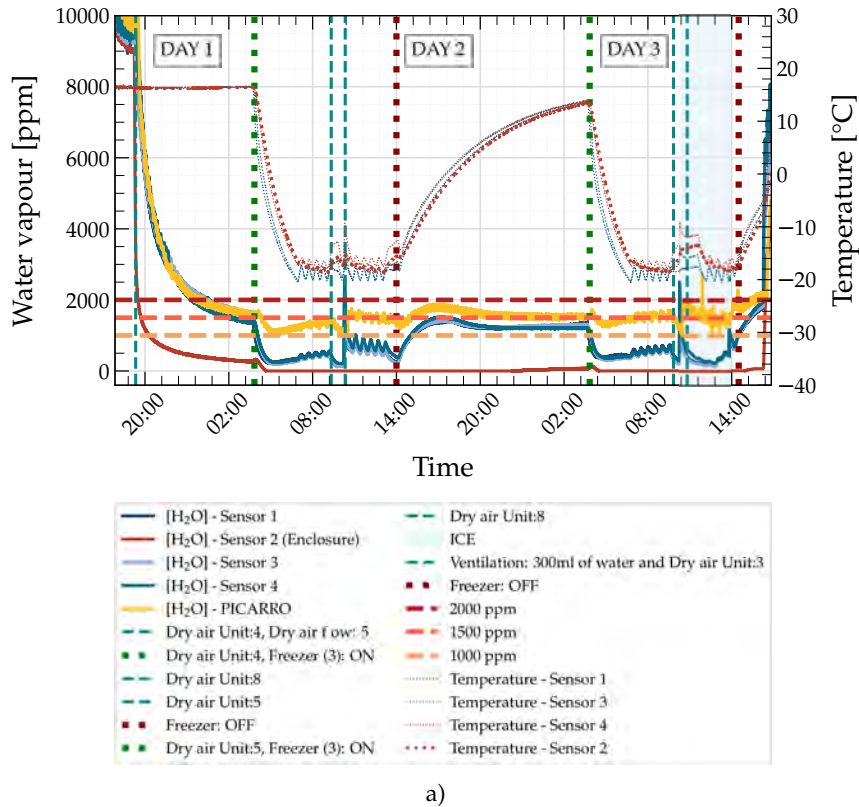


FIGURE 4.13: Water vapour and temperature measurements across three consecutive days. The full temporal profile a) shows water vapour concentration obtained using four DHT22 sensors and CRDS-PICARRO, and temperature conditions (DHT22) influenced by dry air and freezer settings as well as ice presence and ablation processes. b) provides a zoomed-in view of Day 3 processes. Freezer was not activated during the night.

In the final test, EPS (Expanded Polystyrene) foam blocks, which have insulating properties and low moisture absorption, were placed in empty spaces within the

freezer, so that the overall air volume is reduced, helping the system to stabilize humidity levels more quickly. The dry air unit was set to 3 and at the same time, the freezer was activated. When the humidity level was low enough, we turned off the freezer and left the dry air unit operating. Unlike the previous test, the water vapour levels in both the freezer and the enclosure decreased at a similar rate, and it took around 3 hours to reach 1000 ppm water level in the freezer space. In contrast, the previous test required 6-7 hours with the freezer deactivated. The freezer was activated using the timer early in the morning. Dry air unit was switched to 5 during laser ablation measurements. The dry air unit - compressor system was working for 24h, and there was no accumulated water when venting the compressor. The use of the EPS blocks might have facilitated a faster decrease of the humidity but the low flow in the dry air unit did not help humidity reach a low level. Using a more efficient compressor, running it for a long duration, and handling the system remotely once the ice is placed could help prevent excess humidity from entering and ensure faster reduction when it does occur.

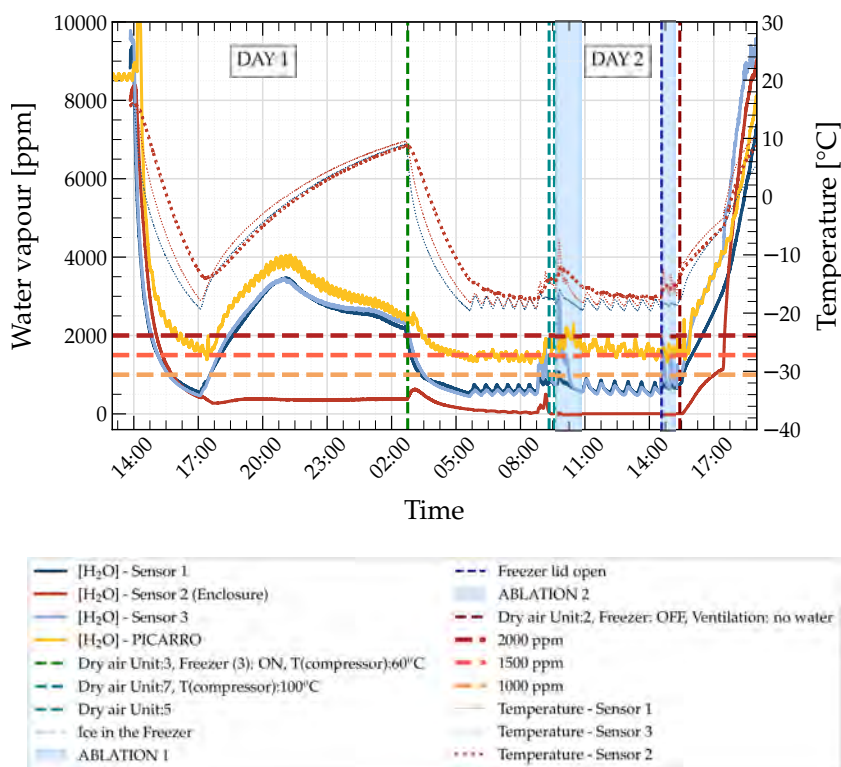


FIGURE 4.14: Water vapour and temperature measurements across two consecutive days. Water vapour concentration was obtained using three DHT22 sensors and CRDS-PICARRO, and temperature was measured by DTH22 sensors.

4.3.5 Discussion and Outlook

The Cryo Cell system designed for LA - water isotopic analysis comprises the motorized translation stage synchronized with laser parameters, which allows for both discrete and continuous ablation, an optics enclosure with the focusing system, and dry air circulation to control conditions within the freezer and the enclosure, reducing condensation and sublimation and ensuring good data quality. While humidity

levels inside the optics enclosure were consistently maintained at low levels, achieving stable humidity control in the freezer remains a challenge. Temporary humidity spikes occur when accessing the freezer highlighting the need for better humidity control during sample handling and overnight operations. Low airflow or prolonged freezer operation can lead to moisture buildup, impacting baseline humidity. High airflow can reduce humidity quickly but is not recommended for long-term use due to energy costs and compressor wear. For recording humidity levels, the CRDS analyzer directly quantifies water vapour via a dedicated conduit, ensuring accurate real-time measurements. Water vapour concentration is also determined using humidity and temperature readings from DHT22 sensors. Even though their response to humidity changes mirrors that measured with the CRDS, they appear to underestimate the absolute water vapour concentration value either due to the calculations used to determine it or their inherently lower accuracy. Also, the current setup, which includes a long stainless steel tube exposed to lab conditions reaching the CRDS analyzer, may be affecting water vapour readings. Testing different tube lengths, insulating the tube or using a different tube material could help maintain a consistent temperature, improving the accuracy of water vapour concentration measurements.

Further modifications could improve humidity control and stability, particularly after freezer access for sample positioning when humidity temporarily peaks. An immediate solution would be to replace EPS blocks with plexiglass boxes filled with ice gel packs. These boxes would occupy unused space, reducing the free air volume and helping maintain a stable low temperature, which indirectly supports humidity control. The ice gel packs' cooling effect would keep the internal environment consistently cold, slowing moisture buildup and promoting faster humidity reduction after opening the freezer lid. Sealing all the openings of the freezer could also contribute to improved control and stabilization of humidity levels within the Cryo Cell. For the laser passage, a sealed optical window can be installed in the opening of the freezer to block external air without disrupting beam propagation. While silicone-based seals or epoxy putty could be applied around cable and tube entry points, rubber grommets with slits or cable entry sealing caps may be preferred for their flexible, airtight seal, allowing easy cable adjustments. Additionally, integrating a freezer-compatible dehumidifier and a high-capacity compressor would contribute to stabilizing low humidity levels.

Overall, improving both the airflow control, freezer access and measurement protocols will be essential for stabilizing humidity and temperature conditions in the Cryo-Cell system, especially during long-duration experiments.

4.4 Crater Characterization

4.4.1 Introduction

The morphology of craters formed during laser ablation provides insights into the laser-material interaction mechanisms, both during and after the pulse. Laser parameters significantly influence ablation phenomena, directly impacting crater size and shape. The properties of the irradiated material play also an important role in laser-matter coupling, leading to variations in crater morphology. Crater characterization provides insights into the efficiency of the laser machining process by examining the volume of ablated material and the quality of ablation, for example through the formation of sharp well-defined craters. It also considers potential accumulation effects, such as heating, absorption, and plasma formation.

In this section, we present a characterization of craters resulting from femtosecond laser ablation on different target materials: stainless steel, glass slides, and artificial ice. We describe the preparation of artificial ice samples and the imaging systems employed, including optical microscopy and a macro-photography setup coupled with focus stacking techniques. By conducting laser ablation experiments with varying parameters—such as laser pulse energy and ablation duration—we investigated their influence on crater size and shape. Analyzing the crater dimensions allowed us to determine laser beam properties and critical parameters like ablation threshold fluence, and the effects of multiple pulses (incubation) using impact-based techniques. Also, the morphology of the craters provides information about underlying processes that we aim to avoid, such as heating and incomplete phase transitions during ablation, which can lead to isotopic fractionation in the ablated material—a critical concern in water isotope analysis on ice cores. This information is crucial for optimizing the ablation process of ice samples by fine-tuning ablation parameters to obtain desired characteristics in both the crater and the ablated material, reflecting their interdependent nature.

4.4.2 Artificial Ice Preparation

A system for the production of cylindrical artificial ice pieces resembling ice cores of length 25 cm and diameter of 10 cm has been developed at PICE [Schmidt, 2021]. Contributions to its current design were made by Kerttu Maria Peensoo (kerttumari-apeensoo@gmail.com), and Alexandre Desaix (vmk779@alumni.ku.dk). The system is designed to produce bubble-free ice samples via a two-step process: initial evacuation of dissolved gases from liquid water and subsequent controlled slow freezing.

The evacuation setup consists of a cylinder mounted on a metal base, with metal lid at the top. The cylinder is secured by long bolts and wingnuts connecting the base to the lid. The lid includes an O-ring to ensure an airtight seal and is equipped with valves for controlling the air evacuation process. The cylinder is connected to a vacuum pump to facilitate the removal of air. This connection is managed through a valve, which allows control over the gas flow into and out of the cylinder. Attached directly to this valve is a pressure gauge for continuously monitoring the pressure

levels inside the cylinder to ensure they remain within the required parameters for the experiments. A water trap, filled with liquid nitrogen, is also integrated into the system to remove moisture from the gas evacuated from the cylinder, preventing water vapour from compromising the integrity of the vacuum system.

The cylinder is filled with milli-Q water and placed on a magnetic stirrer plate with the lid valve closed. Heating and stirring are then initiated concurrently. These processes facilitate removing the air from the water. The vacuum pump is turned on and the pressure inside the cylinder decreases. When the pressure is below 0.1 mbar, degassing starts by opening the lid valve which results in intense bubble generation. The air evacuation should be maintained for at least 30 minutes or more, until the bubble generation is minimized, to avoid bubble formation in the ice. Once evacuation is complete, we first close the lid valve. Then, we use a cap to seal the valve after disconnecting the system at the valve connection.

The second step of slow freezing takes place inside the freezer, where the water is frozen from the bottom up, allowing dissolved gases to escape rather than being trapped in the ice. A heating tube, made of copper with heating wire wrapped around it and insulated with 2 cm of material, covers the cylinder with the degassed water to avoid instant freezing. The tube's temperature is maintained at 4 °C by setting the AC power source's voltage to 150V. Over a period of three days, the motor-driven heating tube is raised, enabling a slow freezing process of the water. This gradual freezing facilitates the upward movement of air and its entrapment as bubbles in the ice is minimized.

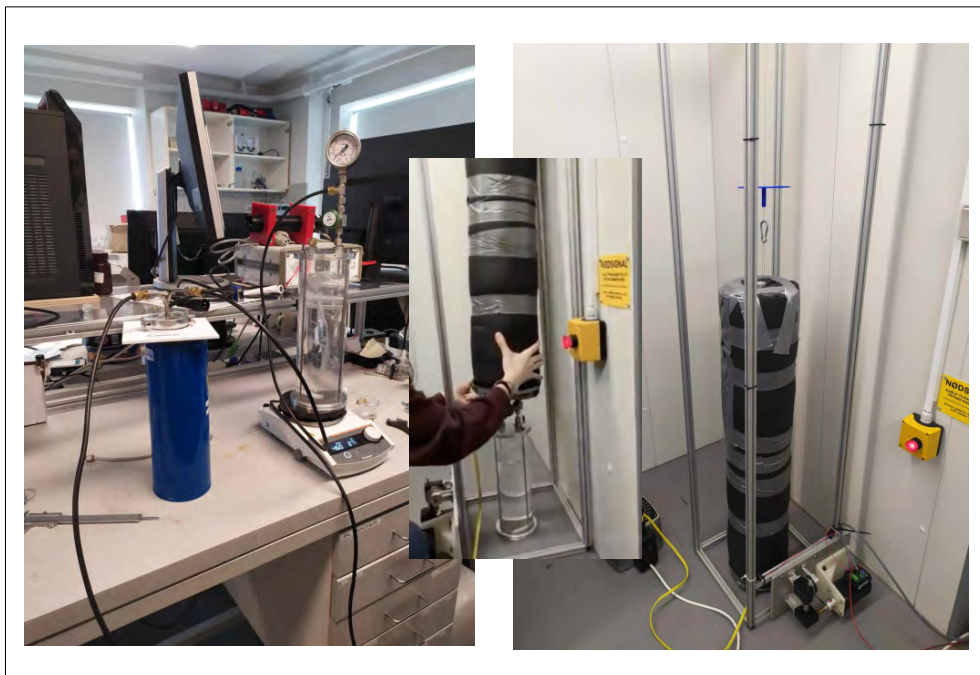


FIGURE 4.15: Setup for artificial ice production: The system includes an evacuation setup with a cylindrical holder on a magnetic stirrer and heater, connected to a pressure gauge, which leads to a water trap filled with liquid nitrogen. The water trap connects to a vacuum pump. For controlled freezing, a heating tube encases the cylinder in a freezer, enabling gradual freezing over 3 days while the tube ascends, driven by a motor.

4.4.3 Imaging Systems

Optical Microscopy

A metallurgical reflection-type microscope (BRESSER Science MTL-201) equipped with objectives ranging from 4X to 80X magnification was used for visual inspection of any modification or crater generated in the ablated samples. A camera with a CMOS detector (BRESSER MikroCamII 5MP HIS Mikroskopkamera), described in section 4.2.2, was integrated into the microscope for image capturing using the Bresser MikroCamLab II software which is available in [BRESSER, 2023]. This system enabled 2D analysis of the microstructures and crater morphology of the samples under varying experimental conditions, allowing for precise measurement of crater size in terms of diameter, without considering depth.

Macro - Photography

To examine ablation crater morphology in both surface features and depth, we employed a macro photography setup using an objective lens combined with focus stacking techniques for image processing. This setup was initially developed by Johanna von Drachenfels (Project: Morphology Characterization of Laser Ablation Craters in Ice). The objective lens provided the necessary high magnification to capture fine details of the crater's surface, but the shallow depth of field at such magnifications limits the focus to only a narrow plane. To address this, focus stacking which involves capturing a series of images at varying focal depths and merging them to create a composite image, has the potential for capturing a crater's surface morphology in two dimensions with high resolution and at the same time to produce a detailed representation of its depth.

Macro photography is a technique that captures small subjects at high magnification, often achieving a magnification ratio of 1:1 or greater. This results in the subject appearing as large as or larger than its actual size on the camera sensor, facilitating observation of fine details. A macro tube or extension tube, extending from the camera could increase the distance between the camera sensor and the lens. This extension allows for greater magnification by enabling the lens to focus much closer than its normal minimum focusing distance. For even higher magnification, far beyond what standard macro lenses can provide, in the front of the macro tube, a microscope objective can be attached. Microscope objectives allow for capturing extremely small details at high resolutions.

A Fujifilm X-T3 camera, equipped with an APS-C sensor with $21.3 \text{ mm} \times 15.6 \text{ mm}$ size, which has 6240 horizontal and 4160 vertical pixels and pixel size of $3.76 \mu\text{m}$, was mounted onto a vertically oriented WeMacro Stand. This stand incorporates a motorized 100 mm rail with a stepper motor of $1 \mu\text{m}$ precision. A computer running WeMacro software [WeMacro, 2024] controls both the camera shutter and the rail's stepper motor via a dedicated controller unit. All connections of the components and system control settings can be found in WeMacro Manual [WeMacro, 2023]. At the base plate of the stand, beneath the camera, the sample platform is adjusted with the integrated manual linear translational stage (XY axes) allowing precise sample positioning. With proper adjustments, the macro-photography system, as shown

in Fig. 4.16 can be converted to the horizontal position. To achieve high magnification, an infinity-corrected microscope objective (MPlan APO HL LWD 20X) with long working distance was selected. The objective was attached to the camera using a WeMacro Pro Grade Raynox DCR150 tube set, which included the necessary adapters (M42-M26 adapter for objective lens and M42-FX adapter for the camera).



FIGURE 4.16: Macro-photography setup including motorized rail with a macro tube attached, mounted on a stand. The tube supports the camera at one end and the objective lens at the other. The stand incorporates a XY stage where the sample is placed.

The numerical aperture (NA) of the objective lens plays a crucial role in determining both the resolution and the depth of field, which is the range in front of and behind the focal point that appears sharp. It also depends on the focal length and distance to the subject. For the MPlan APO HL LWD 20X objective used here, the NA is 0.29, which allows for sufficient light collection and a good resolution balance and the depth of field is approximately $6\ \mu\text{m}$. With the 20 X objective, the camera's $3.76\ \mu\text{m}$ pixel size translates to a physical size $3.76\ \mu\text{m}/20 = 0.188\ \mu\text{m}$ (188 nm) at the sample. This means that each pixel on the sensor represents a region of 188 nm on the sample. To determine crater sizes from the captured images, a calibration was performed using a microscope slide with a 1 mm scale. For the 20 X objective, this yields a conversion factor of $0.17\ \mu\text{m}$ per pixel, which allows the calculation of crater dimensions from image pixel counts.

For image capturing with the macro system, we used LED panels that have adjustable brightness for precise control of light intensity and provide even, shadow-free illumination. They are positioned at adjustable angles on both sides (C.2), ensuring uniform lighting of the sample.

TABLE 4.1: Specifications of the Imaging System and Lens Used in the Experiment

Parameter	Value
Camera Model	Fujifilm X-T3
Sensor Size	23.5 × 15.5 mm
Resolution	6240 × 4160 pixels
Pixel Density	265.66 pxl/mm
Objective Lens	MPlan APO HL LWD 20X
Magnification	20X
Numerical Aperture (NA)	0.29
Depth of Field	6 μm
Micron per Pixel (20X)	0.17 μm/px

Image processing - Focus Stacking

Focus stacking is a digital image processing technique used to overcome the limitations of shallow depth of field, a common challenge in macro and micro photography. By capturing multiple images of the same subject at slightly different focal distances and then digitally combining them, focus stacking produces a final image with a significantly extended depth of field. This technique allows for achieving sharpness across all areas of the image, even when using high magnification or wide apertures that typically result in a very narrow region of focus. The software used for focusing stacking was Helicon Focus Software [HeliconSoft, 2024]. For crater diameter measurement, we developed a Python tool (C.2) that facilitates macro photography image analysis. It employs OpenCV for image processing, where the user can draw circles on craters using a mouse-based interface, and the program calculates and displays the crater diameters in microns.

4.4.4 Crater Morphology and LA Parameters

Metal Target

For the preliminary testing of the LA system, we tested a stainless steel target sample, to assess the performance of the optical setup under various laser parameters, including ablation time (15-60 seconds) and pulse energy (2-40 μJ). The images of the laser ablation craters on stainless steel are obtained using optical microscopy and are presented in Fig. 4.17. Laser pulse energy is a critical factor that influences crater size with higher energies typically producing larger craters, which is consistent with the theory of defect accumulation effects in multiple pulse irradiation [Jee et al., 1988]. Increasing ablation duration which means increasing number of pulses delivered does not contribute to variable crater sizes. Additionally, a coloring effect around the craters is observed, which is attributed to the heating [Di Niso et al., 2014] of the

surrounding metal area during ablation due to the excess energy which is not dissipated in the short interval between pulses. This phenomenon is common in laser ablation of metal employing high repetition rates (more than 10 kHz [Raciukaitis et al., 2008] [Hodgson et al., 2021]).

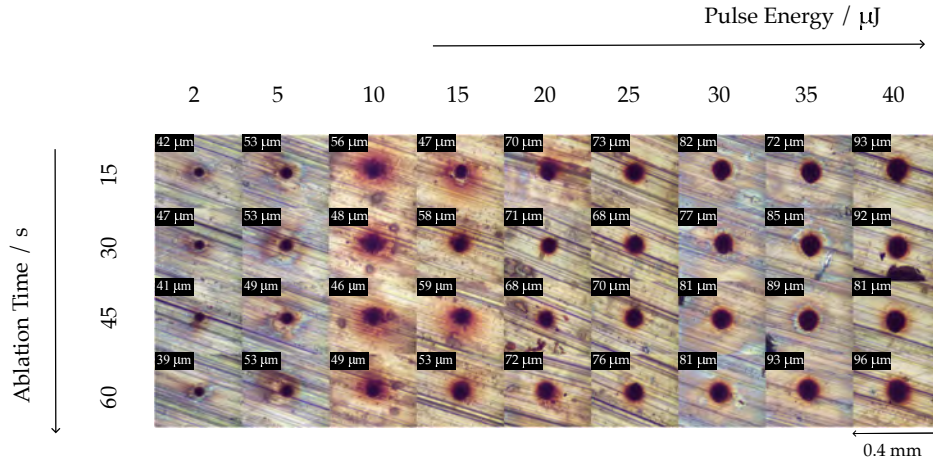


FIGURE 4.17: Laser ablation craters formed on stainless obtained under varying pulse energy (μJ) and ablation time (s).

In Fig. 4.18 the square of the crater diameter is plotted against the logarithm of the pulse energy for different total pulse counts (N: 750000, 1500000, 2250000, 3000000), which are shown with different colors. For lower pulse energy values the crater diameter seems to be consistent before exhibiting an increasing trend. We applied a linear fit to this section of the data, following the D-square method to determine the laser spot size obtained by the system and the threshold fluence for stainless steel, as described by equation 3.11. The results are presented in Table 4.2, which summarizes the ablation parameters including laser beam waist (w), threshold pulse energy (E_{th}), threshold fluence (F_{th}), the coefficient (R^2), and corresponding ablation durations which correspond to a specific number of pulses in each case. The estimated laser spot radius values are very close to the one calculated theoretically in Fig. 4.6 (41.97 μm) for the focusing system used in this experiment. Regarding the threshold fluence, it is confirmed that increasing the number of subsequent pulses delivered to the sample leads to a reduction in its value.

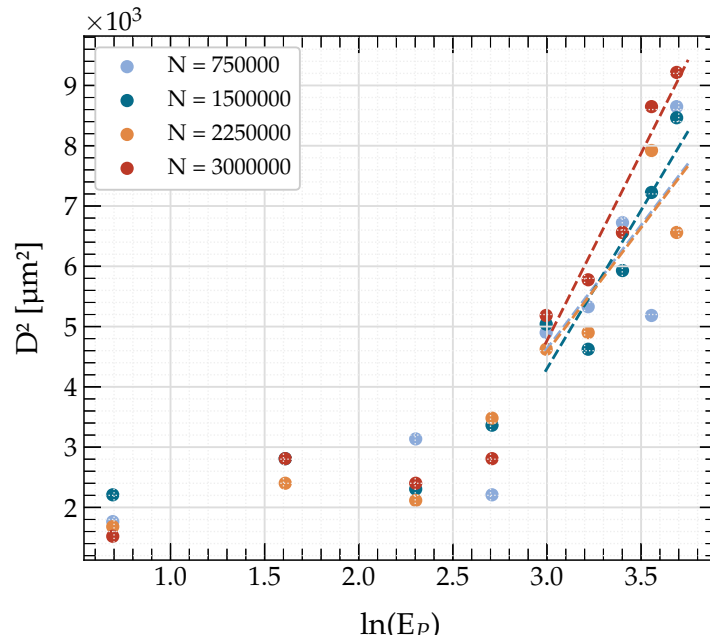


FIGURE 4.18: Linear fit of crater square diameter versus laser fluence for determining the ablation threshold and beam waist of the laser beam in stainless steel target, for different N .

TABLE 4.2: Summary of Ablation Parameters for Stainless Steel

N Pulses	w (μm)	E_{th} (μJ)	F_{th} (J/cm^2)	R^2	Ablation Time (s)
750000	45.24	6.47	0.20	0.52	15.0
1500000	51.24	8.85	0.22	0.82	30.0
2250000	45.33	6.58	0.20	0.69	45.0
3000000	55.72	9.32	0.19	0.92	60.0

In the case of multi-shot laser ablation on metals using repetition rates lower than 100 kHz, incubation effect is found to be low for pulses on the femtosecond regime when pulse of less than 600 kHz are applied in metals [Di Niso et al., 2013]. The incubation coefficient values determined using the model in equation 3.13 are typically between 0.8 and 0.9 [Raciukaitis et al., 2008] [Mannion et al., 2004]. We applied the same model for the threshold fluence of the stainless steel sample (repetition rate: 50 kHz and pulse duration: 400 fs) as derived by the D-square method. Figure 4.19 shows the linear regression of $\ln(NF_N)$ versus $\ln(N)$, where the fitting line is shown as a dashed line. The slope, 0.97, corresponds to the S value and aligns with values reported in the literature, for the applied repetition rate. The intercept of -1.15 corresponds to a threshold fluence of $0.32 \text{ J}/\text{cm}^2$ for a single pulse. The high R^2 value of 0.9944 validates the accuracy of the incubation model applied to ultrashort pulse laser ablation on metal targets.

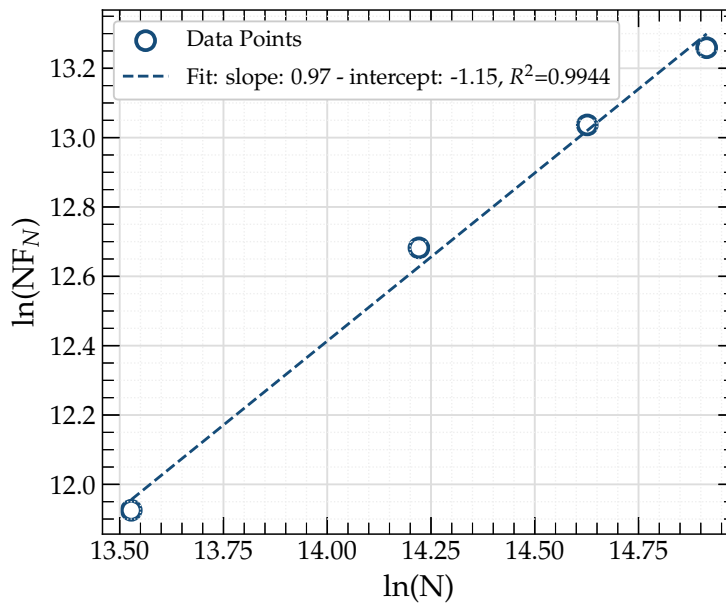


FIGURE 4.19: Plot of the logarithm of NF versus the natural logarithm of N , used to determine the incubation coefficient S from the slope of the fitted regression line. $F_{th}(1)$ can be derived from the intercept.

Glass slide

In laser ablation studies on glass, the resulting crater morphologies were inspected using both optical microscopy and a macro photography system, as shown in Fig. 4.20. For the macro photography setup, a glass slide was placed on a matte black surface to minimize reflections and enhance contrast, and it was then positioned on the macro stage for imaging.

The microscopy provides a detailed view of the ablation features but also results in multiple reflections and interference patterns that can introduce color fringes and obscure fine details of the crater boundaries. The bright background makes it difficult to discern subtle variations in crater morphology, especially in the presence of reflections from the transparent glass slide. In contrast, the macro-photography system offers a different approach to imaging by placing the glass slide on a matte black background. The diffuse, angled lighting and dark background provide enhanced contrast, making crater boundaries clearer and reducing reflections and scattered light. This is especially useful for imaging ablation craters on transparent or semi-transparent materials like glass and ice. The macro images maintain better clarity, showing details such as thermal spallation and cracking, which can be more challenging to capture with the reflective illumination of the microscope.

The evolution of crater morphology and size is influenced by the pulse energy. At lower energy levels, craters are typically small and circular, indicative of a uniform and stable energy distribution from the laser. These craters exhibit well-defined edges with minimal material displacement, suggesting a clean ablation process with

minimal thermal diffusion into surrounding areas. As the energy increases, these initially smooth features transition to more complex structures. By the mid-energy range (25 μm to 30 μm), craters begin displaying pronounced ridges and melting at the edges, with the shape deviating from perfect circularity and the size becoming larger.

At the highest pulse energies (35 μm to 40 μm), craters show considerable changes in morphology, characterized by significant melting, material displacement, and possibly redeposition around the craters. The ridges around these craters are particularly pronounced at the edges, where thermal and mechanical stresses are highest. This reflects the intense interaction between the laser pulses and the glass, where the rapid heating and cooling cycles impact the physical structure of the glass. Sometimes, this abrupt thermal gradient causes the glass to expand unevenly, leading to stress accumulation and the formation of cracks that may propagate from the point of stress like the edges of a crater, and extend outward.

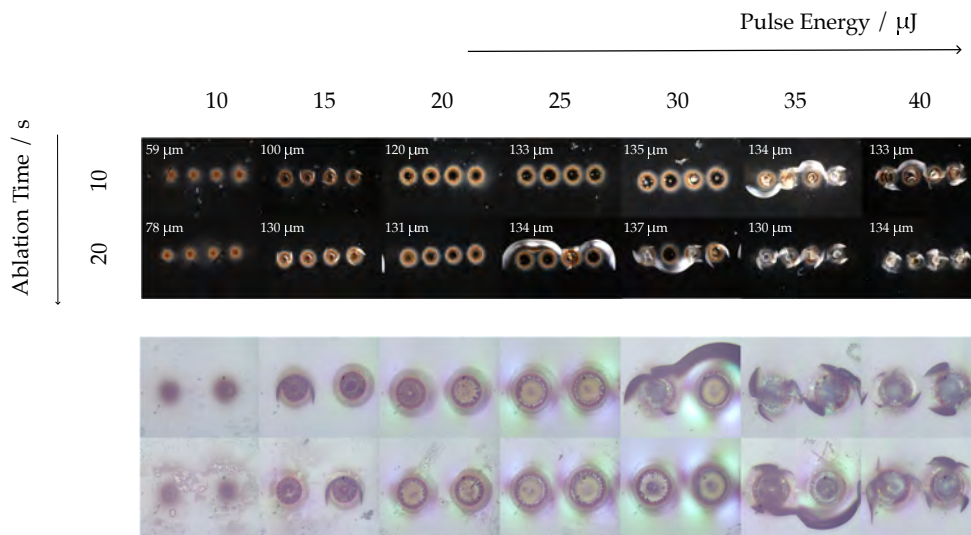


FIGURE 4.20: Laser ablation craters formed on glass slide under varying pulse energy (μJ) and ablation time (s). Crater images were obtained using both the macro system (top) and the optical microscope (bottom).

The plot in Fig. 4.21 shows a linear increase in crater square diameter with the natural logarithm of pulse energy at lower energy levels, indicating a predictable relationship in line with Liu's theory. However, at higher energy values, the trend deviates from linearity, suggesting a saturation effect [Hanuka et al., 2019; Marks et al., 2022] where additional increase in pulse energy results in minimal changes in crater size. This saturation behaviour is more pronounced for the dataset with a higher number of pulses (N: 1 000 000), implying that the ablation process may have already reached a steady state. In this case, the linear regression method for determining the ablation threshold and beam waist becomes less reliable due to potential saturation.

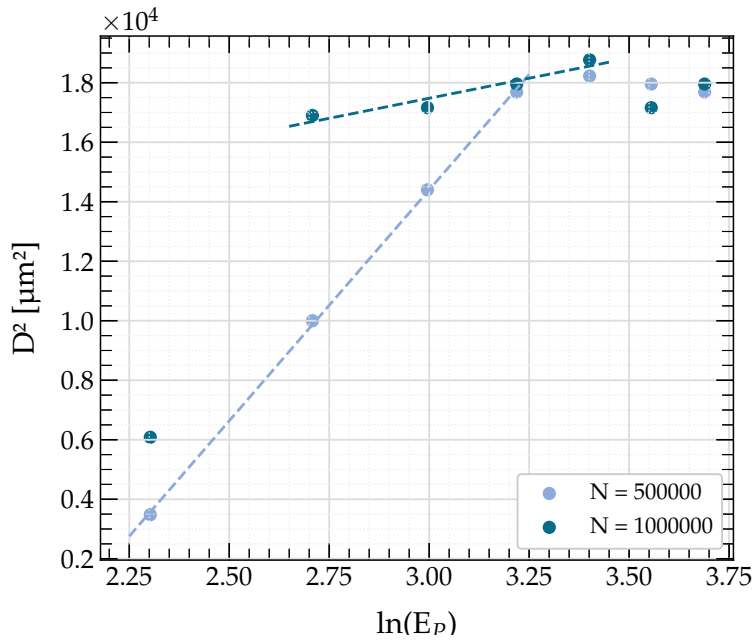


FIGURE 4.21: Linear fit of crater square diameter versus laser fluence for determining the ablation threshold and beam waist of the laser beam in glass slide target.

TABLE 4.3: Summary of Ablation Parameters for glass slide

N Pulses	w (μm)	E_{th} (μJ)	F_{th} (J/cm^2)	R^2	Ablation Time (s)
500000	88.11	7.95	0.065	0.9996	10
1000000	36.71	0.03	0.002	0.9096	20

Artificial Ice Target

Artificial ice cores were prepared according to the method outlined in Section: Artificial Ice Preparation, and subsequently cut into blocks with dimensions of $32 \times 32 \times 250$ mm. The system was flushed with dry air, and the temperature was set to -19°C . After completing the measurements, the sample, still secured in its holder, was removed from the freezer. It was then placed in an ice core box filled with gel ice packs, so it could be transferred to the cold room, where the imaging systems were placed for crater image analysis, avoiding condensation. Inspection of ablation craters was done by the use of optical microscopy. To evaluate the ablation performance and quality for ice measurements, we employed the same crater formation procedure with varying pulse energy values and ablation durations as used for previous sample targets. Pulse energy from $20 \mu\text{J}$ to $40 \mu\text{J}$ was tested for ablation time ranging from 15 s to 60 s, as shown in Fig. 4.22, 4.23. In most craters, an elevated ring of material surrounding the edge of a crater, called a rim is formed, as shown in in Fig 4.22. This is a typical phenomenon in ultra-fast ablation of dielectrics [Mirza et al., 2016] [Zhou et al., 2023]. Rims are generated when the material is ejected during ablation and then recondenses and solidifies around the perimeter. This typically occurs when the laser pulse causes both vaporization and melting. This outward

ejection of material could be also caused by the high-pressure plasma generated during fs laser ablation [Ben-Yakar et al., 2003]. The rapid cooling and re-solidification of this molten material at the edges of the craters lead to the formation of sharp and well-defined rims. This process is facilitated by the short pulse duration and high energy of the laser, highlighting the dynamic interactions of energy absorption, heat transfer, and material displacement.

Crater size increases with both pulse energy and ablation time, though the trend is not strictly linear. At 30 μJ , crater sizes generally grow with longer ablation time, but there are cases where craters at 45 s are smaller than at shorter ablation time, indicating the influence of factors like recondensation or uneven energy distribution. At 35 μJ , crater size consistently increases with ablation time, though some variations remain. At 40 μJ , the largest craters are formed, especially at 45 s and 60 s. Overall, higher pulse energy and longer ablation times (increasing number of pulses in multi-pulse ablation) generate larger craters, but the variations in size suggest a complex interplay of laser pulse energy, material properties, and heat dissipation.

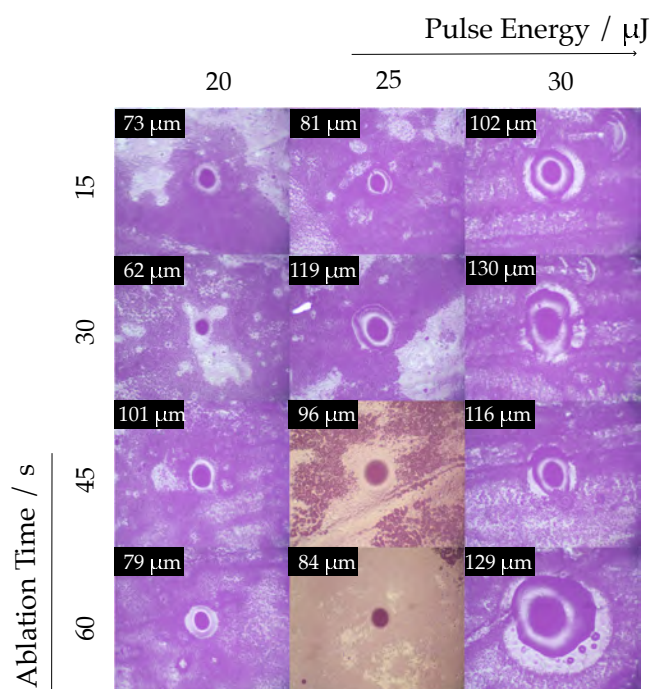


FIGURE 4.22: Ablation craters on artificial ice samples obtained with varying pulse energy values (20 μJ , 25 μJ , 30 μJ) and ablation duration (15 s, 30 s, 45 s, and 60 s). The diameters of the craters are annotated.

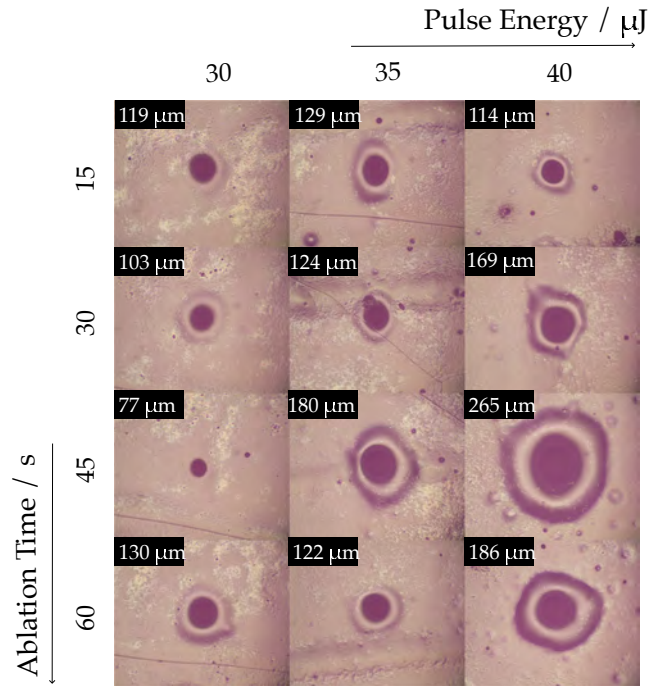


FIGURE 4.23: Ablation craters on artificial ice samples obtained with varying pulse energy values (30 μJ , 35 μJ , 40 μJ) and ablation duration (15 s, 30 s, 45 s, and 60 s). The diameters of the craters are annotated.

We constructed linear regression lines selectively to dataset segments where the relationship between the natural logarithm of pulse energy and the square of crater diameter displayed linear characteristics. The estimated multi-shot ablation threshold values, F_{th} , as derived from the intercept of the linear fit, are the same order of magnitude as the ones estimated for the glass slide for a similar number of pulses. The value for the laser spot radius derived is two or three times larger than the one calculated theoretically, which could be primarily attributed to poor focusing and/or the impact of multiple pulse ablation.

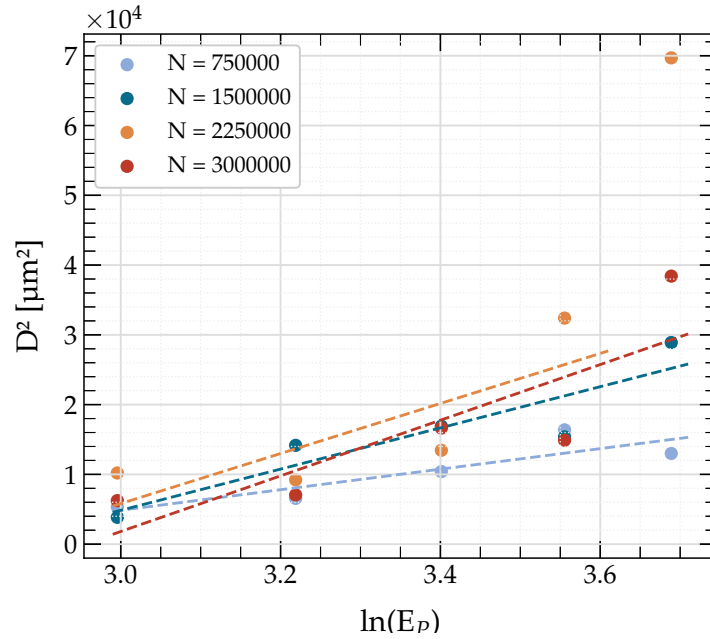


FIGURE 4.24: Crater square diameter versus laser fluence for determining the ablation threshold and beam waist of the laser beam in artificial ice target. Linear fit is applied when possible.

TABLE 4.4: Summary of Ablation Parameters for artificial ice target.

N Pulses	w (μm)	E_{th} (μJ)	F_{th} (J/cm ²)	R ²	Ablation Time (s)
750000	85.80	14.44	0.13	0.78	15.0
1500000	121.50	17.04	0.07	0.82	30.0
2250000	133.91	17.08	0.06	0.63	45.0
3000000	141.20	19.19	0.06	0.70	60.0

For the investigation of the incubation effect of laser ablation on ice with fs laser pulses at 50 kHz, we applied the following equation 3.13 (model 1) and power law models [Ashkenasi et al., 1999] [De Palo et al., 2022] which take into consideration the saturation of incubation for very high numbers of pulses:

$$F_{th}(N) = F_{th,\infty} + [F_{th,1} - F_{th,\infty}] N^{S-1} - (model2) \quad (4.5)$$

where $F_{th,\infty}$ is the saturation fluence, S is the incubation coefficient.

$$F_{th}(N) = F_{th,\infty} + [F_{th(1)} - F_{th,\infty}] e^{-k(N-1)} - (model3) \quad (4.6)$$

where $F_{th,\infty}$ is the saturation fluence, k is an empirical incubation coefficient, which can take any value reflecting the extent of the incubation effect in the specific material.

In Fig. 4.25 the multi-pulse threshold fluence is shown as a function of the number of pulses, along with the models fit. The extracted parameters from model 3 give the values for the single pulse threshold fluence ($F_{th}(1)$: 0.38 J/cm²), the saturation fluence ($F_{th,\infty}$: 0.06 J/cm²) and the incubation coefficient (k : 2.11×10^{-6}). The very

small value of k suggests a slow decay and this might indicate that the material has already reached or is near to saturation. The curve is fitted to data that represent a very high number of pulses, and they lack representation from lower pulse numbers (such as 1, 10, or 1000), capturing a regime that no longer results in significant changes in the material properties and the threshold fluence.

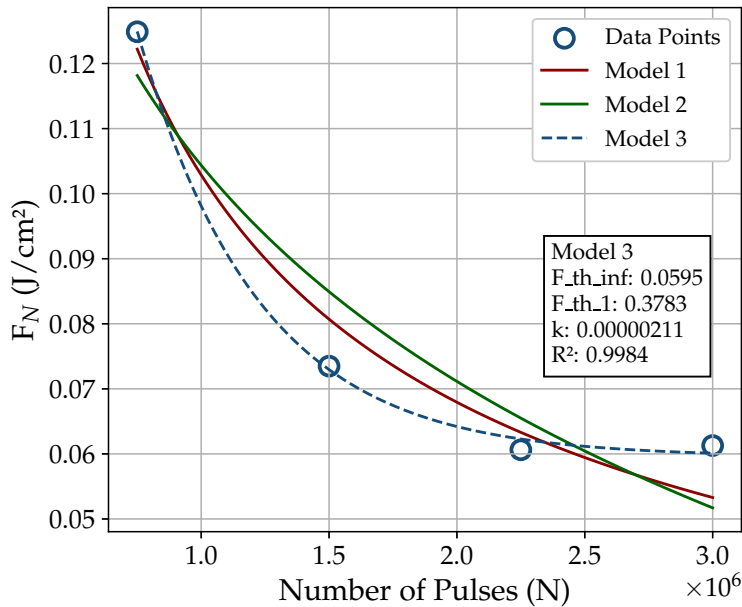


FIGURE 4.25: Plot of the multi-pulse threshold fluence $F_{th}(N)$ versus the number of pulses, N , used to determine the incubation coefficient k , the single pulse threshold $F_{th}(1)$ and the saturation fluence $F_{th,\infty}$ can be derived from the fitting parameters.

LA Groove on ice

We examined laser ablation on ice, analyzing both circular crater creation and grooves. Craters were formed using various pulse energies during a 20-second ablation, employing only a doublet lens for focusing without a beam expander. Grooves were observed at a pulse energy of 40 μ J, with the sample moving at a constant speed of 0.2 mm/s on the linear stage; lower energies failed to yield visible grooves. Images of the craters were captured immediately and 48 hours post-ablation, using the microscope - 20X objective system for Day 0 and Day 2 images. This allows for the evaluation of potential alterations in crater morphology that may suggest post-ablation effects. Day 2 crater images were also acquired using the macro photography system.

We observed minor surface alterations around the craters and subtle changes in their shape between images captured on Day 0 and Day 2, with no significant differences in overall crater size. These observations suggest sublimation effects, underscoring the importance of immediate imaging post-ablation to ensure accurate morphological assessments. No rim formation was observed around these craters, especially compared to previous experiments on ice targets. This could be due to

different energy coupling dynamics or lower thermal effects during ablation, which did not lead to the re-solidification of ejected material.

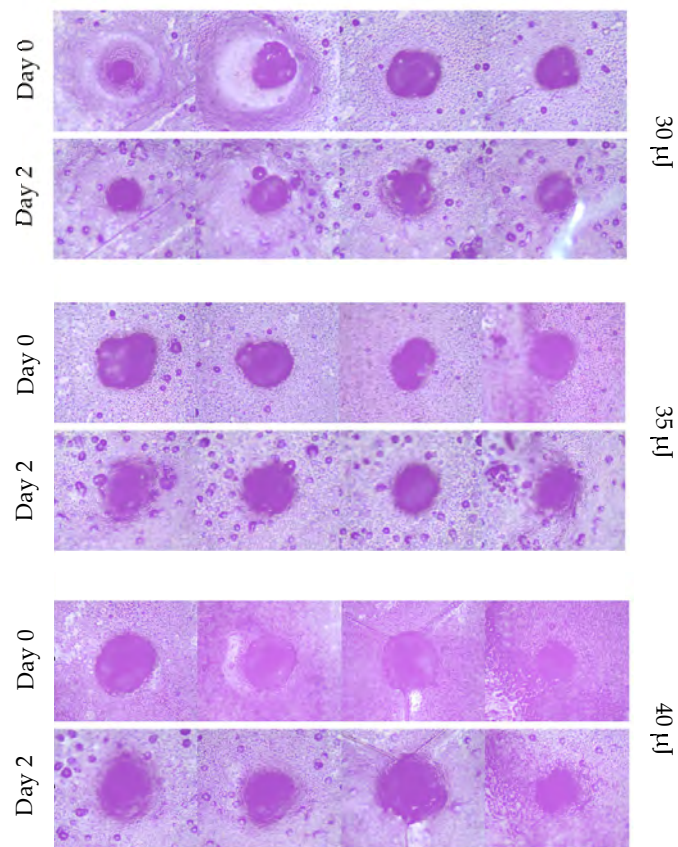


FIGURE 4.26: Ablation craters formed on ice target by fs laser pulses of varying laser energy, 30 - 40 μJ , captured immediately after ablation and two days post-ablation. Imaging: Optical Microscopy

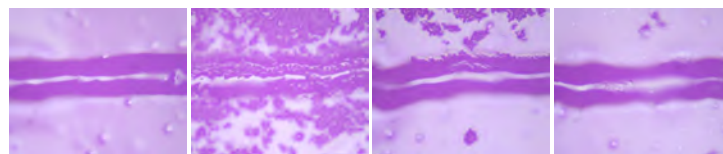


FIGURE 4.27: Ablation grooves formed on ice target by fs laser pulses of 40 μJ laser energy with scanning speed 0.2 mm/s. Imaging: Optical Microscopy

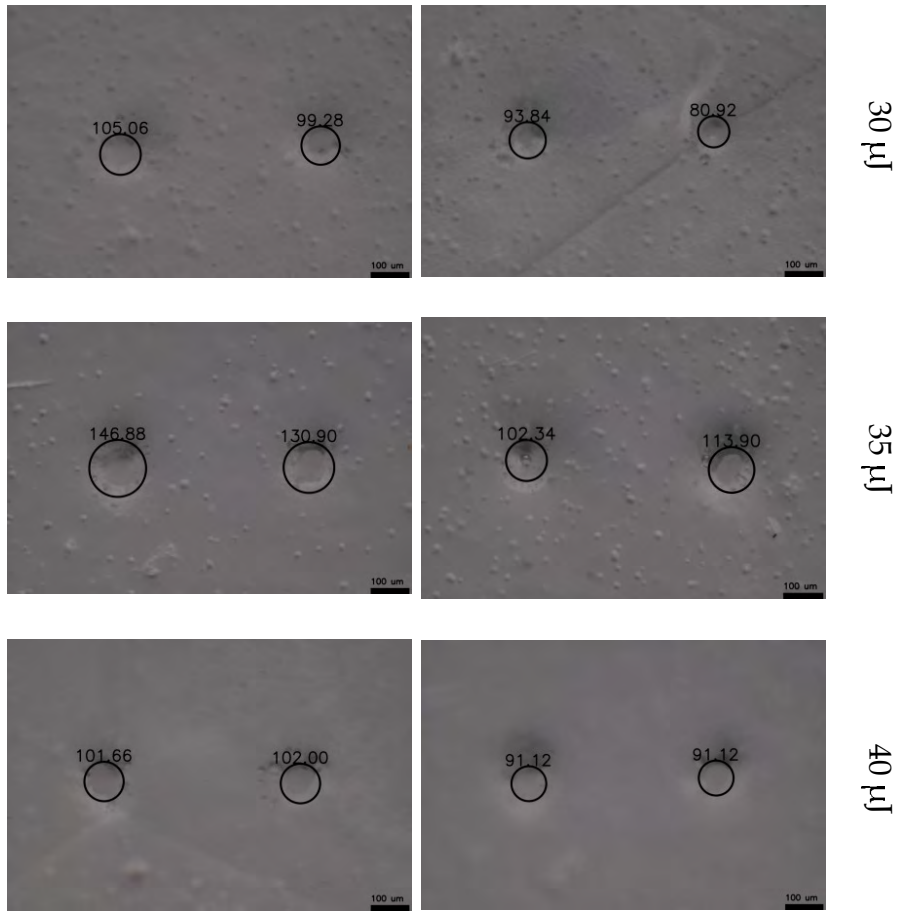


FIGURE 4.28: Ablation craters formed on ice target by fs laser pulses of varying laser energy, 30 - 40 μJ , captured two days post-ablation. Imaging: Macro-Photography

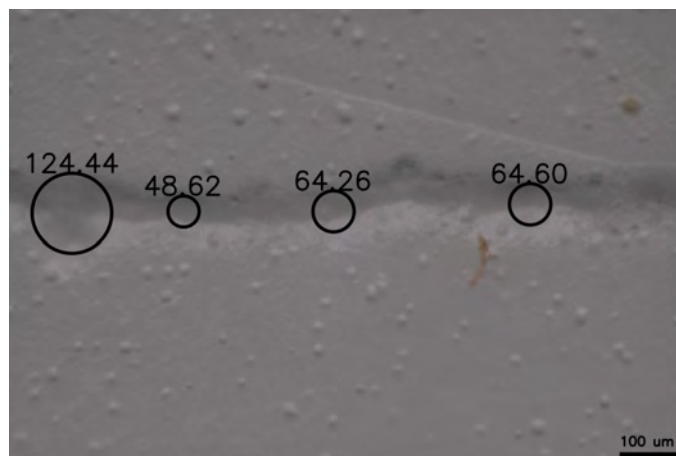


FIGURE 4.29: Ablation groove formed on ice target by fs laser pulses of 40 μJ laser energy with scanning speed 0.2 mm/s. Imaging: Macro-Photography

For 30 μJ , the diameters ranged from about 80 to 105 μm , while for 35 μJ , they reached up to 147 μm . Craters formed at 40 μJ showed diameter values between 91 and 102 μm . The groove demonstrates significant variation in width along its

length, ranging from approximately 48.62 μm to 124.44 μm . This width variability likely results from slight fluctuations in the laser energy, possible shifts in the focus due to uneven surface, and the effect of sample motion on laser energy distribution [Yang et al., 2023]. These factors may cause variations in the laser's interaction with the ice along the groove, leading to inconsistent material removal.

4.4.5 Discussion and Outlook

The characterization of craters and grooves produced by fs laser ablation on stainless steel, glass, and artificial ice targets provides valuable insights into the complex interactions between laser parameters and material properties. In general, higher pulse energies and extended ablation times result in larger craters with more intricate morphologies, featuring characteristics such as ridges, melting zones, rims, and displaced material. Incubation effects, particularly evident in stainless steel, demonstrate that repeated pulses lower the ablation threshold. However, in the high pulse regimes used in this study (750000 to 3000000 pulses), glass and ice likely reached saturation threshold fluence, which may obscure detailed observation of ablation threshold and incubation effects. To accurately study these effects, especially in ice, experiments that include lower pulse numbers are recommended.

In artificial ice, rim formation—caused by the recondensation of vaporized material around crater edges—and variations in crater size at similar pulse energies indicate complex dynamics influenced by recondensation, uneven energy distribution, and possibly poor focusing. These factors complicate efforts to achieve uniform ablation profiles on ice, crucial for preserving isotopic integrity in water isotope analysis. Incomplete phase transitions may lead to isotopic fractionation, emphasizing the need for precise control and further optimization of laser-ice interactions.

Improving the focusing procedure, incorporating both a visual inspection system and advanced focus control is recommended for a more consistent result. A basic camera setup provides essential real-time feedback on crater formation and initial 'tight' focusing which provides flexibility and precision in laser ablation, while enhancing reproducibility [Cousin et al., 1995]. In addition, recent advancements highlight the use of both image-based and signal-based auto-focus methods that ensure high accuracy and responsiveness in laser systems [Dinh et al., 2023]. However, for applications using fs pulses, controlled defocusing could also be beneficial, as it optimizes material removal while minimizing thermal damage and this could also be investigated [Chang et al., 2012].

The optical microscopy system captures surface details of the craters and grooves, effectively showing edge smoothness and subtle changes over time, but it lacks depth perception due to the single focal plane, making it difficult to observe internal crater features. The macro photography system with focus stacking offers a limited sense of depth but does not provide a clear view of the morphology due to the reflective background and lower resolution. Future work should focus on improving imaging techniques, possibly with higher magnification objectives and optimized lighting, as well as dark background to enhance depth and morphological clarity. Also, Cryo-Scanning Electron Microscopy (Cryo-SEM) should be considered for imaging ablation craters. In this case, the sample should have a height of

approximately 5 mm and a length of less than 1 cm. Developing a method to create ice samples of these specific dimensions is necessary. Once craters are drilled into the samples, they can be transferred to SEM for analysis using small, insulated polystyrene boxes in a liquid nitrogen environment. This approach would allow detailed visualization of internal crater features, complementing the limitations of optical microscopy and macro photography.

4.5 Ablation Chamber

4.5.1 Introduction

The ablation chamber links the femtosecond laser ablation system and the CRDS analyzer, facilitating the collection, integrity, and efficient transfer of ablated material for water isotope analysis of the ice core samples. In this section, we present the design and functionality of the ablation chamber developed for the fs laser ablation system, which features an open design that allows the chamber to be positioned above the ice sample without fully enclosing it. The cryo-cell can accommodate ice core sections up to 55 cm in length, and the chamber forms a seal at its base where it contacts the ice. The design should ensure effective handling of the ablated material and precise control of gas flow for robust and smooth delivery of the ablated mass to the analyzer. Key features to meet these requirements include the use of dry air as a carrier gas, which is compatible with the CRDS analyzer, sealing mechanisms, and precision alignment. Theoretical estimations investigating the effects of laser ablation parameters and gas flow on water vapour production, guided the development of the chamber, ensuring the design met both practical and analytical needs. This section explains the design process of the ablation chamber and each component's function, outlining the key considerations that shaped the prototype. It further discusses the insights gained from testing the 3D-printed prototype and details the refinements that should be implemented in the final version.

4.5.2 Water Vapour production by fs LA on ice

The primary aim is to investigate the impact of various laser settings and operational conditions, together with varying carrier gas flow rates, on the production of water vapour and its final concentration. Calculations of water vapour produced by LA were based on ablation crater dimensions, depth and diameter, which are related to the ablated volume.

The fluence F , (energy per unit area delivered by the laser) is calculated for different pulse energies using the formula 3.12, with E the pulse energy values ranging from 5 to 40 μJ and w , the beam radius at focus set at 50 μm . For each fluence value that exceeds a pre-set threshold F_{th} of 15 μJ , the crater diameter is calculated based on the equation 3.11 which provides insight into the lateral extent of the ablation. The ablation depth per pulse, L , is determined using the equation 3.10 characterizing the depth of material removed by each laser pulse on the high fluence regime using the heat diffusion length l_{th} (Eq. 3.8), for pulse duration $\tau_L = 400$ fs.

The volume of ice affected by ablation is estimated by assuming a cylindrical crater geometry, where the ablation depth and crater diameter are used to approximate the ablated volume V_{ice} :

$$V_{\text{ice}} = \pi \left(\frac{D}{2} \right)^2 \cdot L$$

From this calculated volume, the mass of ice removed (m_{ice}) is derived by:

$$m_{\text{ice}} = V_{\text{ice}} \times \rho$$

TABLE 4.5: Parameters for Water Vapour Production Calculations

Parameter	Value
Physical Properties of Ice	
Thermal Conductivity (k)	2.22 W/(m K)
Specific Heat Capacity (c_p)	2090 J/(kg K)
Density (ρ)	920 kg/m ³
Chemical Properties of Ice	
Molecular Weight of Water (M_{water})	18.015×10^{-3} kg/mol
Optical Properties of Ice	
Absorption Coefficient (α)	28.427/m
Constants	
Ideal Gas Constant (R)	8.314 J/(mol K)
Experimental Parameters	
Laser Wavelength (λ)	1030 nm
Laser Pulse Duration (τ_L)	400 fs
Laser Beam Radius (w_0)	1.2 mm
Beam Expander	3X
Lens Focal Length (f)	200 mm
Focused Beam Spot Radius (w)	50 μ m
Scanning Speed (v)	0.2 – 1 mm/s
Threshold Pulse Energy (E_{th})	15 μ J
Pulse Energy (E_{pulse})	20 – 60 μ J
Flow Rate Range	20 – 40 cm ³ /min
Temperature (T)	253 K
Pressure (P)	101 325 Pa

We assume a complete conversion of the ablated ice mass to vapour, which simplifies the calculation of vapour yield. However, this approximation may lead to an overestimation because not all energy leads to direct vaporization in fs laser ablation. Ablation of dielectrics with femtosecond lasers often involves rapid electron excitation and ionization, leading to a complex process that includes melting, vaporization, and phase explosions, resulting in droplets and clusters along with vapour. Despite this, the assumption of complete vaporization provides a useful estimate of the vapour produced and allows straightforward comparisons of vapour yields under different experimental laser ablation conditions.

The volume of water vapour at given temperature and pressure is calculated by the ideal gas law:

$$V_{\text{vapour}} = \frac{m_{\text{ice}} \times R \times T}{M_{\text{water}} \times P} \quad (4.7)$$

where R is the ideal gas constant, T is the temperature, M_{water} is the molecular weight of water, and P is the atmospheric pressure. The values of the parameters used for the calculation are detailed in Table 4.5.

The concentration of water vapour in the gas flow is calculated by:

$$\text{Water Vapour [ppm]} = \left(\frac{\text{Water Vapour [cc/min]}}{\text{Total Flow Rate [cc/min]}} \right) \times 10^6$$

where the total flow rate ranges from 20 cm³/min to 40 cm³/min.

Various ablation scenarios are explored to simulate different experimental conditions. Two primary modes are considered: discrete ablation and continuous scanning. In discrete ablation, the laser repeatedly targets the same spot on the sample, allowing for estimation of the penetration depth and material removal achieved by each pulse over a set ablation time. The calculations yield an estimate of the total ablated volume and the mass of ice removed, providing a basis for understanding the efficiency and consistency of material removal. The number of laser pulses, N , delivered during the ablation of a single spot can be calculated as:

$$N = f_{\text{rep}} \cdot t_{\text{ablation}} \quad (4.8)$$

where N is the total number of laser pulses, f_{rep} is the pulse repetition frequency (PRF), and t_{ablation} is the ablation time. The effective number of pulses [Zhao et al., 2019] [Crawford et al., 2004], N_{eff} , in scanning mode is determined by considering the overlap between pulses and is calculated by the following expression:

$$N_{\text{eff}} = \frac{2 \cdot w \cdot f_{\text{rep}}}{v} \quad (4.9)$$

where w is the laser spot radius, f_{rep} is the pulse repetition frequency (PRF) and v is the scan speed.

Fig. 4.30 shows ablation characteristics as a function of laser fluence, F_0 , ranging from 0.15 to 0.25 J/cm² and the number of pulses up to 3×10^6 as determined for ablation time varying from 10 to 60 seconds. These results are based on the assumption that the total penetration depth is the product of the number of pulses and the ablation depth per pulse. It is important to note that this assumption oversimplifies the actual dynamics of laser ablation, where effects such as shielding, redeposition, and changes in material properties often prevent a linear increase of ablation depth with increasing pulse count. The first graph shows that the total penetration depth reaches approximately 3.76 mm at higher fluences and pulse counts, which provides an estimate of ablation efficiency. The second graph shows the crater diameter, which ranges from 57 mm to 192 mm, with changes primarily driven by the number of pulses, indicating a cumulative effect on the lateral dimensions of the ablated zone. The third graph shows the mass of ablated ice reaching a maximum of 112.5 μg , reflecting the combined influence of fluence and pulse number in determining the total material removal.

Fig. 4.31 presents water vapour production (in ppm) as a function of laser pulse energy (5 to 40 μJ), and dry air flow rate (20 to 40 cc/min), assuming complete conversion of ablated mass to vapour. The vapour concentration reaches a maximum

of approximately 3000 ppm at high pulse energy and low flow rates. However, this simulation does not account for complex physical and optical phenomena that take place during ablation [Jiang et al., 2004; Christensen et al., 2009; Wædegaard et al., 2012] that affect crater shape and in turn the amount of ablated material, in the form of water vapour.

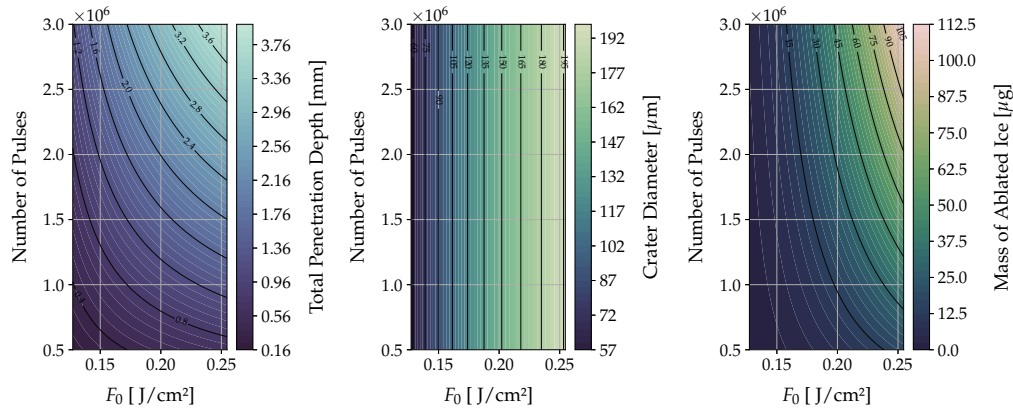


FIGURE 4.30: Ablation characteristics as a function of laser fluence (F_0) and number of pulses. Shown from left to right: total penetration depth, crater diameter, and mass of ablated ice.

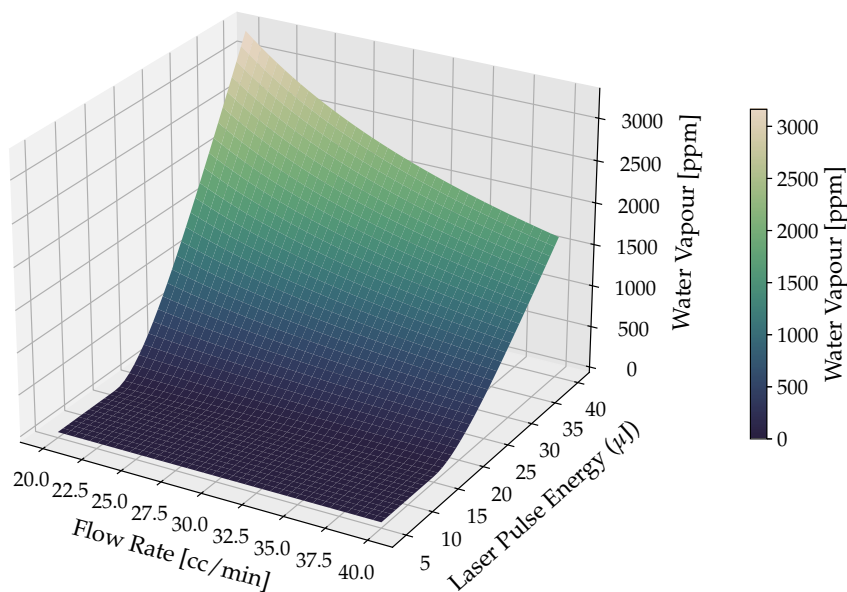


FIGURE 4.31: Water vapour production (ppm) as a function of laser pulse energy and dry air flow rate during ablation. Ablation time varies from 10 to 60 seconds.

Fig. 4.32 shows ablation characteristics as a function of laser fluence, F_0 , and scanning speed of the linear stage (0.01 to 1 mm/s). Again, the total penetration depth is assumed to be a simple multiple of the effective number of pulses and the ablation depth per pulse. The maximum penetration depth in this case is 0.123 mm,

which decreases with increasing scanning speed, indicating a reduction in the effective number of pulses impacting a specific location. The second graph shows a consistent crater diameter ranging from $57\ \mu\text{m}$ to $192\ \mu\text{m}$, unaffected by scanning speed but influenced by fluence. The third graph shows a maximum ablated mass of $3.6\ \mu\text{g}$ which is significantly lower compared to fixed spot ablation due to the reduced interaction time between the laser and the sample.

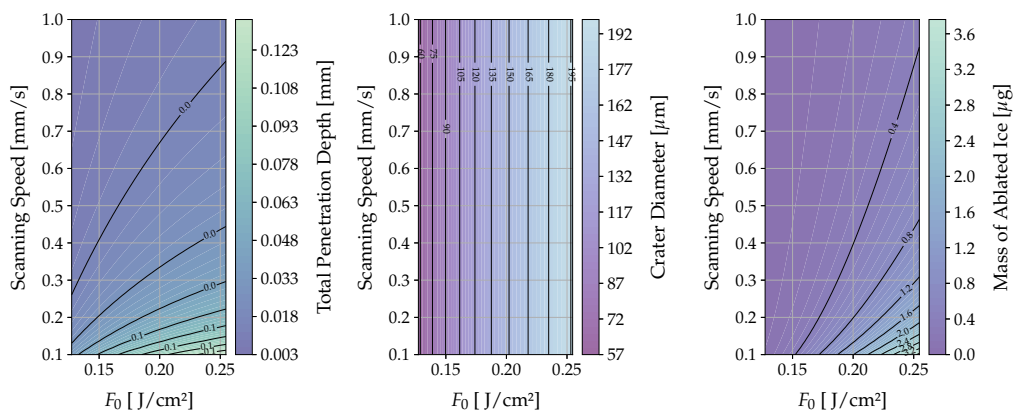


FIGURE 4.32: Ablation characteristics as a function of laser fluence (F_0) and scanning speed of the linear stage. Shown from left to right: total penetration depth, crater diameter, and mass of ablated ice.

4.5.3 Ablation Chamber Design

The ablation chamber was designed to facilitate laser ablation sample collection within a controlled environment ensuring accuracy and repeatability during the analysis.

The lower section comprises a small cylindrical compartment (Fig. 4.33), sealed from above by the laser window and from below by an O-ring, forming the ablation cup (V_{cup} : $2174\ \text{mm}^3$) where ablation occurs. This compartment has a threaded hole for installing a 1-inch laser optical window (Fig. 4.33b), allowing the laser beam to pass through while maintaining a sealed environment, which is critical for ensuring beam quality and preserving sample integrity. The O-ring at the base forms a tight seal with the surface of the ice sample (the groove for the O-ring can be seen in Fig. 4.33c), preventing the escape of ablated material and maintaining the environmental integrity of the sample area, ensuring that external contaminants do not interfere with the experiment. The O-ring should create a smooth contact that allows the ice sample to move beneath the chamber without causing any disturbance. As the linear stage moves the ice sample, the O-ring maintains stable contact, ensuring both an effective seal and the preservation of the sample's integrity. The chamber is equipped with angled sample inlet and outlet channels positioned at 45 degrees, represented by the yellow fittings. These angled channels are used to introduce and extract gases during the ablation process. The inlet supplies dry air, which flows through the ablation cup to guide the ablated material towards the outlet. The outlet connects to a tube interfacing with a CRDS analyzer. The controlled airflow from the inlet to the outlet ensures that ablated material driven by the carrier gas is efficiently transported out of the chamber and directed to the analyzer for further analysis, allowing for real-time monitoring of the ablated material.

The upper section of the chamber has a dual-concentric design. The central opening is reserved for the laser beam to pass through, while the surrounding annular space is filled with dry air. The dry air is introduced via the flush port and flows into four small holes in the bottom section of the chamber, which align with the corresponding annular space (Fig. 4.33c). These holes channel the dry air down to the base of the lower section, where they extend to the perimeter of the interface between the chamber and the sample. In this arrangement part of the dry air at the interface is directed towards the outer diameter of the O-ring, which establishes a controlled flow of air that prevents the air of the cryo-cell from entering the ablation zone, thus preserving a stable environment during ablation.

The ablation chamber assembly is mounted to the plexiglass enclosure using a mounting flange (Fig. 4.34), which is designed to accommodate four guide rods, serving as the integration point with the enclosure to provide a secure and rigid attachment (Fig. 4.35). The guide rods extend from the mounting flange through holes in the upper part of the chamber, providing stability and precise vertical alignment, allowing the entire assembly to be finely adjusted in height. This setup ensures that the entire system, including the optics, the hole in the plexiglass, and the corresponding hole in the chamber, remains aligned, thus maintaining the precise laser path for ablation. The springs attached to the guide rods, stabilized by shock rod ends or spring cups, maintain controlled compression and extension, allowing the chamber to adapt to variations in sample height without compromising alignment. This feature ensures consistent positioning of the chamber and enhances repeatability and precision during the ablation process. The spring mechanism allows for smooth vertical compliance when encountering minor surface irregularities, enabling the chamber to slide over the sample when the latter is moving. Although there are four guide rod connections, only two of them are used to allow for controlled lateral flexibility. This provides sufficient vertical stability while offering the necessary degree of freedom to compensate for small surface irregularities, ensuring that the chamber remains properly aligned as the linear stage moves the ice sample.

The 3D-printed ablation chamber was integrated into the optics enclosure and adjusted to maintain a secure fit on a metal target (placed on the linear stage), with an O-ring in contact with the surface. Two guide rods were incorporated to provide flexibility during translational movement. The chamber's performance was tested with the sample moving at a speed of 0.2 mm/s ([video](#)). In future iterations, changes in the O-ring and spring-mechanism could be made to improve sliding between the ice sample and the chamber for better performance.

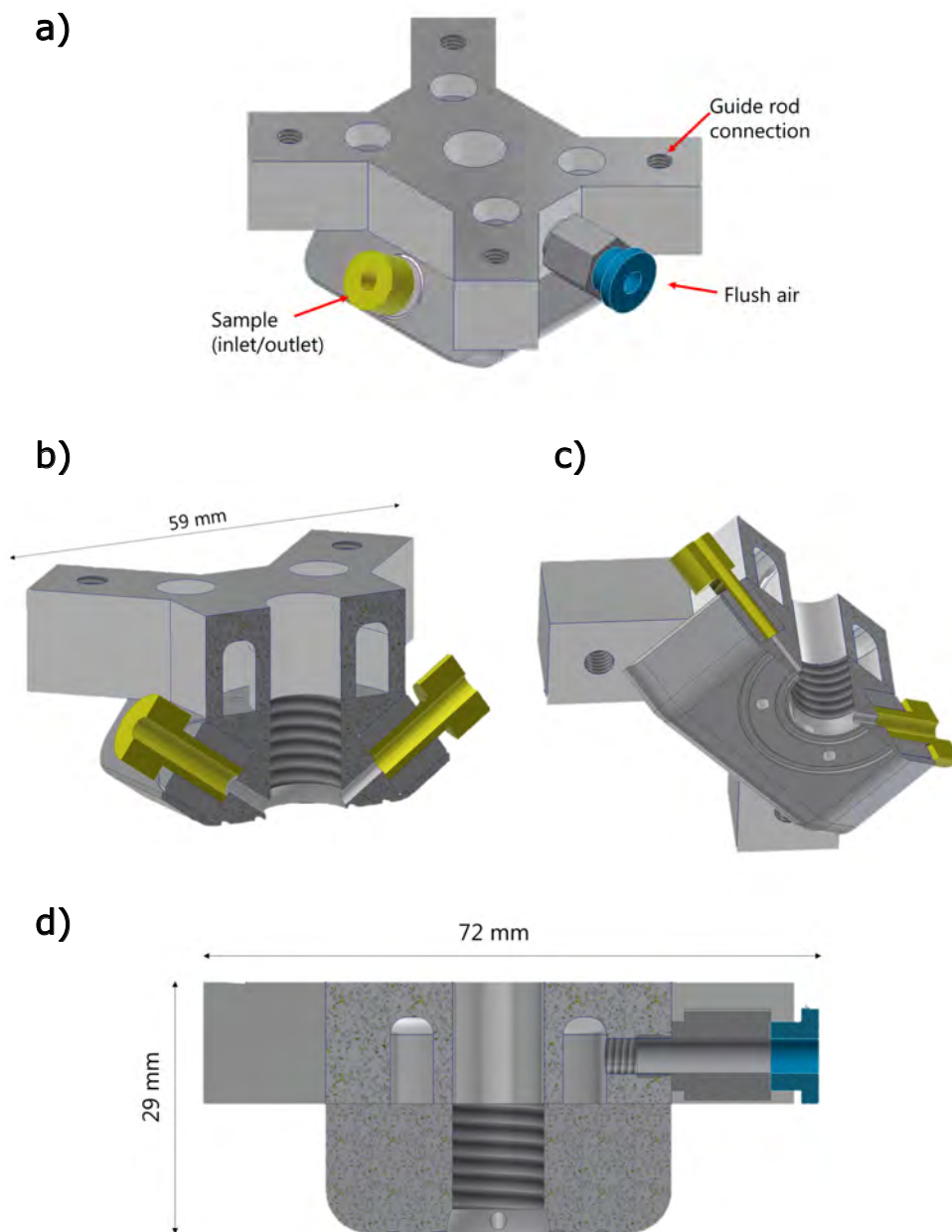


FIGURE 4.33: Initial prototype of the ablation chamber for the fs LA-CRDS system. (a) Top view showing guide rod connections, sample inlet/outlet, and flush air port. (b) and (c) Cross-sectional views illustrating the sealing mechanism and internal structure. (d) Side view with dimensions of the ablation chamber, highlighting the chamber geometry.

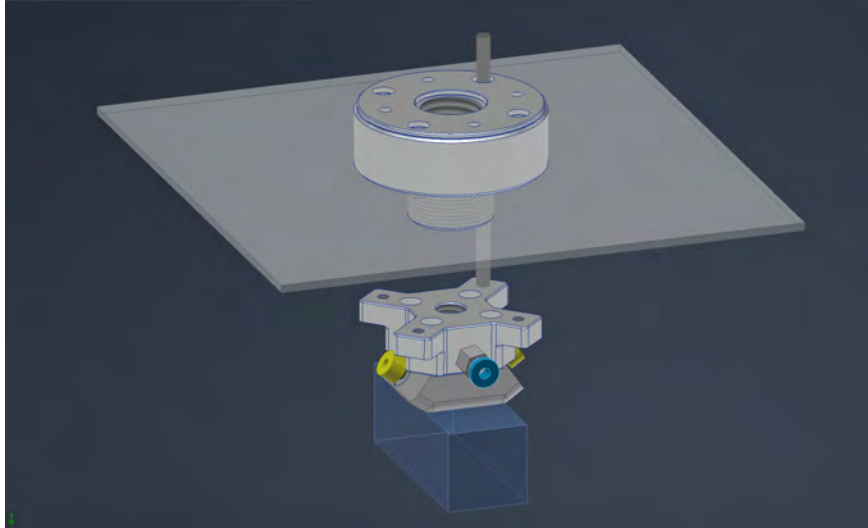


FIGURE 4.34: Assembly of the ablation chamber positioned under a plane representing the optics enclosure, showing the mounting features for alignment and stability.

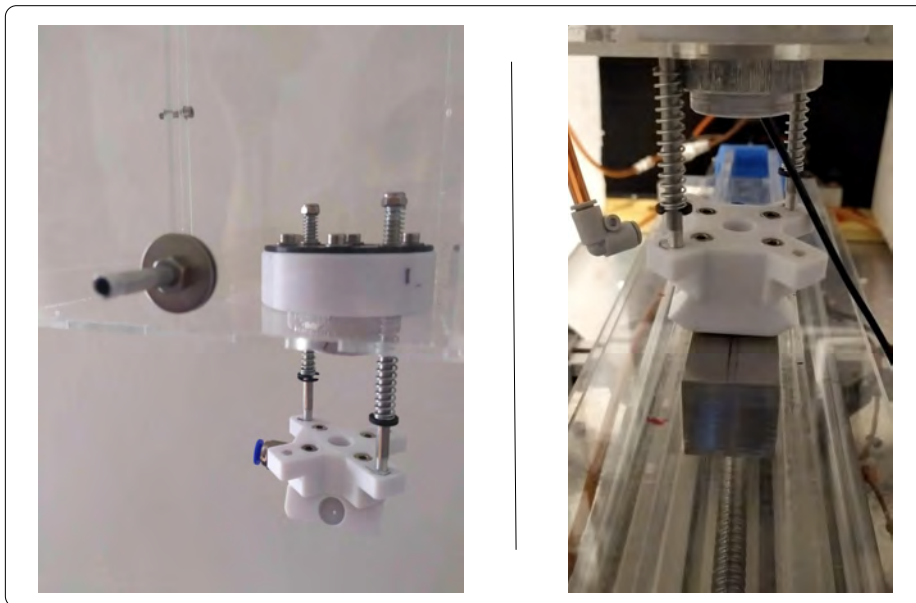


FIGURE 4.35: 3D-printed ablation chamber prototype. (Left) Mounted on the plexiglass enclosure, showing the guide rods and spring mechanism for positioning. (Right) Chamber positioned above a metal target on the linear stage, used for testing.

4.5.4 Discussion and Outlook

The initial prototype of the ablation chamber was designed and 3D-printed, integrated into the system and tested. The results indicate that while the chamber structure meets several key requirements, the spring mechanism and the O-ring interface need refinement to improve movement smoothness, especially when used on an ice surface. Enhanced flexibility and stability during translational movement are essential for consistent contact and to minimize wear between the O-ring and the sample surface. Furthermore, dedicated experiments focusing on crater characterization under varying experimental parameters—including high-resolution imaging of craters/grooves and measurement of crater dimensions and especially ablation depth—will be essential to understand the exact volume of material removed. This data will facilitate more accurate simulations of water vapour production and optimization of flow dynamics within the chamber. An in-depth examination of the quality of the generated/collected sample and gas transfer processes will be important in minimizing isotopic fractionation. By enabling controlled and efficient transport of ablated material in continuous scanning mode, the *fs LA-CRDS* system can be further evaluated for isotopic composition accuracy in subsequent CRDS analysis.

Chapter 5

ns LA - CRDS

5.1 Paper published in Analyst

This chapter presents a proof-of-concept study that represents a key advancement in the application of LA-CRDS for water isotope analysis in ice cores. Building on the methodological framework of the previous chapter, which introduced the fs LA-CRDS for high-resolution water isotope studies, this chapter shifts focus to a nanosecond laser operating in the UV range. The goal is to evaluate the feasibility of coupling a commercially available ns LA system from the University of Venice, typically used with an ICP-MS analyzer for impurity studies in ice cores, with CRDS, while optimizing experimental parameters to maximize water vapour production for isotopic analysis.

A central focus of this study is the ability of the ns LA system to effectively produce water vapour from solid ice samples, addressing the critical question of how to optimize vapour yield while minimizing isotopic fractionation. The research systematically investigates parameters influencing vapour production, providing valuable insights into the dynamics of laser-material interaction and the efficiency of the ablation process. Despite the inherent limitations of ns lasers—such as the potential for isotopic fractionation due to longer pulse durations—this chapter highlights how far this technology can be pushed to achieve high-resolution water isotopic measurements.

Another key aspect of this study was the preparation of solid ice standards, providing a way to calibrate water isotope measurements with the new ns LA-CRDS system. Traditionally, liquid standards are used for VSMOW-SLAP calibration in water isotope analysis, as the analytical procedure for ice cores involves melting the ice into a liquid state. This approach ensures consistency between the sample and calibration standards before vaporization and subsequent measurement. However, laser ablation used in this study, which generates the gas-phase sample directly from the ice, requires isotopically homogeneous ice standards, prepared from the available liquid standards, to achieve reliable calibration. This enables calibration using ice standards with LA-CRDS, reducing potential errors such as isotopic fractionation during phase transitions and discrepancies in vapour generation between ice ablation and liquid standard vaporization.









By analyzing artificial ice standards and an Antarctic ice core sample, this study demonstrates the potential of using a ns LA-CRDS system for water isotope analysis, while identifying the current limitations and areas for improvement. Despite challenges such as isotopic fractionation and signal fluctuations during laser ablation, the initial findings are promising, indicating that the isotopic composition of both standard and ice core samples is in reasonable agreement with known values, though further refinement is needed.

This work shows how ns LA technology can optimize vapour yield, achieve system stability in discrete analysis mode through laser ablation raster-scanning, and provides insights into isotopic fractionation and its possible sources. Furthermore, it establishes a basis for comparing ns LA systems with fs LA systems, laying a foundation for advancing laser-based isotopic analysis methods. The goal is to achieve greater precision and accuracy specifically for ice core studies, while also broadening applicability to paleoclimate research and related fields. The versatility of LA-CRDS technique extends to various fields beyond ice cores, facilitated by CRDS instruments designed for specific isotopes like $\delta^{13}\text{C}$. This technology has been proven effective in studies involving both inorganic and bioaccumulated carbonates [Stremtan et al., 2024].



Cite this: DOI: 10.1039/d4an01054j

Towards high-resolution water isotope analysis in ice cores using laser ablation – cavity ring-down spectroscopy†

Eirini Malegiannaki, ^{*a,b} Pascal Bohleber, ^{b,c} Daniele Zannoni, ^b Ciprian Stremtan, ^d Agnese Petteni, ^b Barbara Stenni, ^b Carlo Barbante, ^{b,e} Bo M. Vinther ^a and Vasileios Gkinis ^a

A new micro-destructive technique for high-resolution water isotope analysis of ice samples using a Laser Ablation (LA) system coupled with a Cavity Ring Down Spectrometer (CRDS) is presented. This method marks the first time water isotope analysis is conducted directly on the ice, bypassing the traditional steps of melting and vaporizing the ice sample, thanks to the direct transition of ice into water vapour through the laser ablation process. A nanosecond ArF laser ablation system (193 nm) with an integrated two-volume ablation chamber was successfully coupled to a CRDS analyzer, utilizing nitrogen as the carrier gas. The application goal is the use of LA-CRDS for ice core studies, so a method for preparing ice standard samples using liquid water isotope standards, widely used for ice core analysis, is introduced. The measurements were conducted in a discrete mode, by performing laser ablation raster scans of 4 mm × 4 mm areas, establishing a sampling resolution of 4 mm along an ice core's depth. The water vapour concentration reaching the CRDS analyzer as well as the quality of the water isotopic measurements of $\delta^{18}\text{O}$ and δD were influenced by laser parameters, such as laser spot size, repetition rate, laser fluence, ablation time as well as by the flow rates of the carrier gas. After optimizing the experimental conditions for water vapour formation, three ice standards samples were analyzed for calibration purposes on the VSMOW-SLAP scale and a section of an ice core sample was also tested. Critical parameters influencing the precision and accuracy of water isotopic measurements were investigated, and isotopic fractionation phenomena were identified, pointing to essential considerations for the technique's further development.

Received 2nd August 2024,
Accepted 19th October 2024

DOI: 10.1039/d4an01054j

rsc.li/analyst

1 Introduction

Polar ice core records stand as one of the most invaluable archives in paleoclimate research, providing detailed insights into environmental changes spanning from decades to hundreds of millennia.¹ The Beyond EPICA project, aiming to

retrieve a 1.5 million year-old ice core from Antarctica, represents a significant step forward in this field with water isotopes serving as a pivotal parameter for past climate reconstruction and interpretation.² Water stable isotope ratios, which are usually reported in delta-notation ($\delta^{18}\text{O}$ and δD),³ are fundamental to the study of past climate processes, acting as a proxy for past temperatures.⁴ Ice core archives allow for the continuous experimental determination of water isotopes^{5,6} which in turn enables the detailed reconstruction of climate records, improving our understanding of past atmospheric conditions and long-term climate trends. However, extracting water isotope signals from the Beyond EPICA – Oldest Ice Core presents unique analytical challenges. In the ice core's oldest and deepest sections and up to the depths where the stratigraphy is preserved, more than 10 kyr are packed into each meter of ice.^{7,8} The resulting extremely thin ice layers require high-resolution sampling techniques to improve both depth and temporal resolution which will lead to high-quality signal retrieval and better interpretation of the

^aPhysics of Ice Climate and Earth, Niels Bohr Institute, University of Copenhagen, Tagensvej 16, 2200 Copenhagen, Denmark. E-mail: eirini.malegiannaki@nbi.ku.dk

^bDepartment of Environmental Sciences, Informatics and Statistics, Ca' Foscari University of Venice, Via Torino 155, 30172 Venice Mestre, VE, Italy

^cDepartment of Geosciences, Alfred Wegener Institute Helmholtz Centre for Polar and Marine Research, Bremerhaven, Germany

^dTeledyne Photon Machines, Bozeman, MT, USA

^eInstitute of Polar Sciences, National Research Council (CNR-ISP), Via Torino 155, 30172 Venice Mestre, VE, Italy

†Electronic supplementary information (ESI) available: Humidity response of the CRDS analyzer, TEDRIST ice core cutting scheme, and LA-CRDS measurement images from the TEDRIST ice core section. See DOI: <https://doi.org/10.1039/d4an01054j>



climate data. The development of cutting-edge, high-resolution sampling techniques is crucial not only for extracting continuous high-resolution water isotope signals but also for investigating processes that contribute to signal attenuation or even loss in deep ice, such as the diffusion of water molecules, critical for signal restoration,⁹ and the formation of water veins.^{10,11}

Cavity Ring Down Spectroscopy (CRDS)^{12,13} has been widely used for water stable isotope analysis on ice cores with comparable precision to the traditional IRMS analyzer.^{14,15} A CRDS water isotope analyzer utilizes a high finesse optical cavity to extend the effective path length of a laser beam, enabling the ultra-sensitive detection of gas-phase molecules and producing signal for multiple water stable isotopes simultaneously ($\delta^{18}\text{O}$, δD) based on their unique near-infrared absorption characteristics. The implementation of Continuous Flow Analysis (CFA) for ice core samples¹⁶ enabled continuous melting of the ice, which after efficient vaporization of the liquid sample and subsequent water isotope analysis by CRDS, has resulted in high-precision water isotope signals along with a depth resolution of less than 1 cm.^{17–19} However, even with streamlined sample preparation in current CFA-CRDS protocols, the melting procedure can artificially alter the signal, the depth control remains challenging, and the resulting depth and temporal resolution is insufficient for resolving thin layers in the deep ice cores. This underscores the need for the development of high-resolution, minimally invasive sampling techniques.

Laser Ablation (LA) is used as a sampling method²⁰ that allows a minute amount of sample to turn into vapour, plasma, and particles, without any specific requirements of sample size or preparation. For analytical purposes, the ablated material is collected in an ablation chamber and transported *via* a carrier gas to an analyzer, commonly an ICP-MS (Inductively Coupled Plasma – Mass Spectrometer).²¹ LA-ICP-MS exploits the particulate phase of the ablated material, introduced directly to the analyzer, for chemical analysis, leaving the ablation chamber which is flushed with a carrier gas. LA analytical power lies also in the direct analysis of the vapour produced by measuring the atomic/ionic emissions of the created plasma (LIBS).

LA has been already used both for LIBS hydrogen isotope analysis of frozen water deuteriated samples^{22,23} and for ice sampling obtaining high-resolution multi-elemental analysis of ice samples when coupled with ICP-MS.^{24–26} Given its micro-destructive nature and high spatial resolution of sub-millimeter scale, LA serves a dual purpose on ice sampling: (a) minimal sample preparation while the smallest amount of sample possible is used for analysis and (b) ice core analysis achieving a depth resolution of less than 100 μm , producing even two-dimensional impurity images on ice sections.²⁷ Existing laser ablation systems vary primarily in the type of laser source used and the design of the ablation chamber. The former impacts the methodology for sample removal and the nature of the ablated material for analysis, while the ablation chamber design influences how the sample is collected and delivered to the analyzer, both of which are crucial for accurate analysis.

Laser pulse duration and wavelength stand out as the most investigated parameters that affect the laser-matter interaction, thereby shaping the properties of the removed material.^{28–31} Lasers that emit radiation in the infrared (IR) and generate pulses either in the nanosecond²¹ or femtosecond regime^{32,33} have been utilized for laser ablation on ice samples taking into account the high absorption coefficient of ice at this wavelength.³⁴ Laser sources emitting at wavelengths of 213 nm (ref. 35 and 36) and 193 nm (ref. 26 and 37) have been shown to couple well enough with ice in spite of its low absorption at these wavelengths.³⁴ In particular UV excimer lasers at 193 nm achieve controlled ablation with significantly less material removed than with an IR laser source.

Ablation chambers implemented to date come in two designs: open and closed. Open design is used for measurements of entire sections of an ice core cut³⁵ according to a standard scheme into lengths of either 55 cm or 100 cm for specific analyses. In this configuration, the ablation chamber is positioned above the sample, and it is crucial to establish a secure seal at its base. On the other hand, the closed design is tailored to hold smaller sections of the core within the chamber.^{26,38} Advancements in closed system designs include the introduction of a smaller inner cup³⁹ within the ablation chamber. This modification reduces the dispersion of ablated material both at the site of ablation and along the transfer line, enabling precise adjustment of the carrier gas flow⁴⁰ for efficient and reliable delivery to the analyzer.

Exploiting the unique advantages of Laser Ablation as a sampling method, the integration of LA with CRDS is proposed to tackle the intricate challenges involved in water isotope analysis in deep ice cores, offering high-resolution sampling with a more straightforward and accurate depth registration, while at the same time preserving the samples for further analysis. At Ca' Foscari University of Venice, it was the first time, to our knowledge, that water isotope analyses were conducted utilizing a commercial Laser Ablation (LA) system coupled with a Cavity Ring Down Spectrometer (CRDS), with careful adjustments to the coupling protocol already used for LA-ICP-MS²⁶ and fine-tuning of laser parameters. While the basic working principles of LA sampling remain consistent, significant differences arise when interfacing with a CRDS analyzer, particularly in terms of required water vapour quantities, adopted configurations for collecting and transporting the ablated mass, and the characteristics of the gas ultimately analyzed.

2 Methods

2.1 ns LA – CRDS system

The Laser Ablation – Cavity Ring Down Spectrometer (LA-CRDS) experimental setup for ice is based on the ice core LA-ICP-MS system established at the University of Venice.²⁶ It comprises three core units: (a) the Laser Ablation (LA) system which incorporates an ArF* excimer laser to generate laser pulses in the nanosecond regime (Analyte Excite+, Teledyne Photon Machines, Bozeman MT, USA), (b) the ablation cryo-



cell (HelEx II 2-volume ablation cell, Teledyne Photon Machines, Bozeman MT, USA) designed for placing the ice sample, where the ablated mass is generated and collected, and (c) the CRDS Water Isotopic Analyzer (L-2130i, PICARRO, Santa Clara CA, USA) employed for conducting water isotope measurements on the ablated samples (Fig. 1). A transport line serves as the conduit connecting the LA system and the CRDS, and delivers the ablated sample from the ablation cell directly to the CRDS cavity for analysis. The microscope system for sample visualization is designed with adjustable magnification and incorporates a high-definition, color GigE camera, positioned perpendicularly to the sample and aligned co-axially with the laser beam. The laser beam and the optical camera move in alignment on the Z-axis, facilitating precise focusing of the laser beam onto the sample surface.

2.1.1 Ablation chamber. The two-volume cryo-cell is a closed-chamber configuration which indicates that the ablation chamber accommodates the sample internally (Fig. 1a) as well as an inner cup (Fig. 1b) that surrounds the area where the ablation takes place. The cell is designed with an upper transparent window for observation, while its inner cup features a conically shaped enclosure sealed by an optical window, allowing the laser beam to reach and irradiate the sample. The beam itself is perpendicular relative to the sample plane. The bottom part of the cell houses a specially designed cryogenic sample holder.²⁶ Through the circulation of a glycol–water mixture cooled at $-35\text{ }^{\circ}\text{C}$, the system ensures the ice sample's surface remains around $-23 \pm 2\text{ }^{\circ}\text{C}$.⁴¹ Positioned above the sample surface, the open-bottomed design of the inner cup directs the ablated material into the integrated collection line, using cyclonic flow leading to low-dispersion ablation.^{39,42–44} Maintaining a fixed distance between the inner ablation cup and the sample surface ensures a steady sampling environment and a consistent path for gas transfer for every ablation event.

Sample transport is facilitated by the carrier gas which is introduced *via* two independently controlled inlets of the cell: one delivering gas through the HelEx arm to the inner ablation cup, and the second to the main body of the ablation chamber. The outlet of the system, functioning as the collection line, is designed to be co-axial with the carrier gas flow of the arm, and employs a PEEK tube with an outer diameter of $1/16''$. This forms a direct link to the CRDS analyzer inlet. The flow rate in both the inner ablation cup and the main body is controlled by software-integrated mass flow controllers, MFC2 and MFC1 respectively, and can be fine-tuned for rapid single pulse response (SPR) or for maintaining more stable signals, based on the specific requirements of the application. Mounted on a motorized stage, the cryo-cell allows precise micrometric movement for flexible ablation in single-spot, line, or raster scanning modes.

2.1.2 LA-CRDS coupling. Originally designed to interface with an ICP-MS instrument for multi-elemental impurity studies on ice cores,^{26,27} the LA system adapted for this study, employing the L-2130i CRDS as the analyzer.^{12,45} In the standard operational mode of the L2130-i analyzer, a mixture of water vapour with dry air or nitrogen flows continuously through the cavity. This process stabilizes the cavity at a pressure of 67 mbar and maintains a temperature of $80\text{ }^{\circ}\text{C}$. The water vapour concentration in the cavity is kept within a range of 1000–30 000 ppm. To ensure a steady flow, the system employs two proportional valves, arranged in a feedback loop, designed to regulate the flow of gas entering (inlet) and exiting (outlet) the cavity, achieving a flow rate of $40\text{ cm}^3\text{ min}^{-1}$ in standard condition. For the LA-CRDS operation, nitrogen was selected as the carrier gas, compatible with both the LA chamber and the CRDS cavity. The coupling of the two instruments was established using the PEEK $1/16''$ outer diameter transport tubing, extending from the inner ablation cup directly to the CRDS inlet in an open split configuration to stabilize the gas flow to the analyzer. All the connections can be depicted in Fig. 1c and 2.

2.2 Water vapour detection

During LA-CRDS measurements, laser pulses ablate a pre-defined surface area as the ablation chamber moves in a bidirectional raster scan, continuously transferring ablated ice to the CRDS cavity. Raster scanning mode was selected over line scan and single spot ablation because it produced a continuous stream of freshly ablated material, resulting in a stronger signal in the CRDS analyzer. The produced ablated mass consists of a mixture of aerosol and vapour. The presence of a filter placed directly after the CRDS inlet and before the cavity effectively prevents particles in the aerosol phase from entering the cavity. Each measurement generates a distinct peak for the water vapour signal, as depicted in Fig. 2. This figure further clarifies the measurement process where the laser ablation process is captured in the bidirectional scanning mode: a green spot marks the beginning of laser firing (raster scan) and a red spot denotes the end of the last pulse of the scan. The markers correspond to the green and red dashed lines on

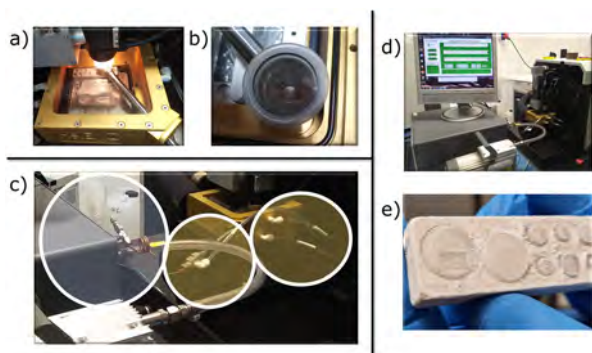


Fig. 1 Detailed view of the LA-CRDS setup and sample processing components. (a) Cryo-cell loaded with samples. (b) Close-up of the ablation chamber's inner cup. (c) Connections for LA – CRDS coupling. (d) The integrated LA-CRDS system. (e) Metal holder containing ice samples. The first cavity shows the result of laser ablation in a raster scan mode, where the material has been removed.



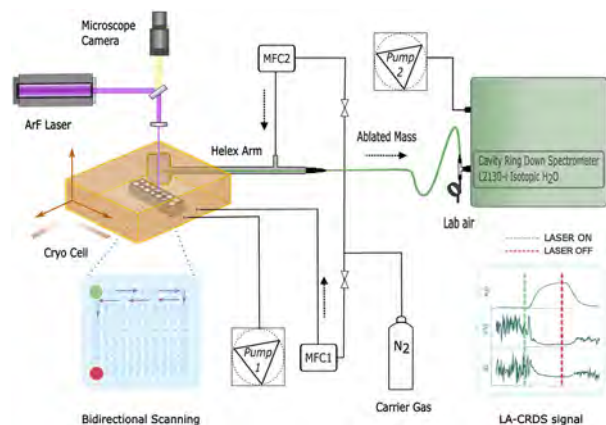


Fig. 2 Schematic diagram of the LA-CRDS experimental setup, highlighting the signal progression captured by the CRDS analyzer during a laser ablation raster scan on an ice sample.

the time series graphs for water vapour, $\delta^{18}\text{O}$, and δD . The water vapour signal exhibits a consistent pattern, gradually rising, plateauing during a stable measurement phase, and then returning to the baseline, when no more vapour mass is delivered, as the continuous flow of nitrogen gas removes residual water vapour, before the next measurement preventing interference. This pattern directly corresponds to the $\delta^{18}\text{O}$ and δD readings, which also display a phase of stability within the same time intervals during the raster scan.

Optimization of the laser parameters, carrier gas flow rates, and the scanning mode were critical for detecting a relatively high signal for water vapour ($\text{H}_2\text{O} > 2000$ ppm) (Fig. S3†) and they are presented in Table 1. The laser settings for the measurements in this study were as follows: the fluence was set between 7 and 10 J cm^{-2} , the repetition rate was 300 Hz , while using a laser spot size of $150 \mu\text{m}$. The ablation time was

typically set at around 90 seconds covering an area of $4 \text{ mm} \times 4 \text{ mm}$, establishing a 4 mm sampling interval along an ice core's depth (vertical axis of the ice core). The dosage, which defines the number of laser pulses per unit of space, was 12 – 20 and its high-value results in a better S/N ratio.⁴⁶ The flow rates for MFC1 and MFC2 were maintained between 0.1 and 0.15 L min^{-1} . It was observed that lower flow rates and lower pressure (15 PSI to 16 PSI) resulted in a higher and more stable water vapour concentration (Fig. S3†). This suggests a two-phase ablation product: aerosol and vapour. At low pressures, only vapour is transported through the PEEK tube, moving much slower than aerosol under normal conditions, leading to a longer washout period. The resulting water vapour levels detected, between 2000 – $12\,000$ ppm, highlight the successful optimization of the LA-CRDS measurement parameters, well above the detection threshold of the CRDS analyzer.

2.3 Sample preparation

Following the recently established approach for making homogeneous artificial ice standards for calibration of the ICP-MS, we used “method A” described in ref. 47. A metal plate with holes of three distinct sizes (two large at 14.9 mm diameter, six medium at 7.7 mm diameter, and six small at 5.9 mm diameter) served as both the tool for creating the standards and the sample holder for analysis (Fig. 1e). Holes were filled with standard water of known isotopic composition, followed by rapid freezing upon submersion in liquid nitrogen. The resulting ice surface was leveled by scraping with a ceramic ZrO_2 blade (American Cutting Edge, USA), either through manual application or with the blade secured in a custom-designed PTFE vice. This process ensures a uniform distance between the ablation chamber and sample surface for efficient material collection and minimizes signal fluctuations during laser ablation analysis.

Table 1 LA-CRDS operating parameters

Laser system parameters	
Pulse width	ns
Wavelength	193 nm
Fluence	7 J cm^{-2} to 10 J cm^{-2}
Repetition rate	300 Hz
Spot size	$150 \mu\text{m}$
Dosage	12 – 20
Ablation time	$\approx 90 \text{ s}$
Raster scan area	$4 \text{ mm} \times 4 \text{ mm}$
Laser ablation cell	
Carrier gas	N_2
MFC1 – ablation chamber	0.1 L min^{-1} to 0.15 L min^{-1}
MFC2 – ablation cup	0.1 L min^{-1} to 0.15 L min^{-1}
Pressure – ablation chamber	15 PSI to 16 PSI
Pressure – ablation cup	15 PSI to 16 PSI
Cavity ring down spectrometer	
Carrier gas	N_2
Cavity pressure	67 mbar
Cavity temperature	$80 \text{ }^\circ\text{C}$
Flow rate	$40 \text{ cm}^3 \text{ min}^{-1}$
Water vapour	2000 ppm to $12\,000 \text{ ppm}$

3 Results and discussion

3.1 Ice standards characterization

Water isotope measurements were conducted using Discrete Liquid Analysis *via* Cavity Ring-Down Spectroscopy to evaluate the ice standard preparation method. Ice samples were produced from the NS liquid standard (Methods, Section 2.3), extracted from each hole, and melted at room temperature for 10 – 15 minutes. The resulting liquid samples were analyzed with the CRDS analyzer in Discrete Analysis mode. We collected 400 – $600 \mu\text{L}$ of water from large holes, which were individually analyzed. In contrast, meltwater from sets of six medium holes was combined into single samples for analysis. Ice from small holes was not analyzed due to extraction difficulties. The sample preparation procedure was conducted five times, resulting in a total of 15 samples: 10 from the large holes (two per repetition) and 5 from the medium holes (one per repetition, combining meltwater from all six medium holes). Measured isotopic average, after the removal of one



outlier, for $\delta^{18}\text{O}$ (-15.17‰ , $\text{SD} = 0.07$) and δD (-112.38‰ , $\text{SD} = 0.31$) showed no significant deviations from the established true value (-15.37‰ and -112.75‰ , respectively). Analysis of isotopic signatures, grouped by hole size, revealed no significant differences, demonstrating water isotopic homogeneity across samples prepared with varying hole sizes. This supports that hole size does not impact measurement accuracy, validating the use of diverse hole sizes for ice sample preparation.

3.2 System performance

3.2.1 System stability. To assess the system's stability, we created an ice standard sample using an adhesive chamber mold attached to a polycarbonate slide, which we filled with the NS water isotope standard following "method C" described in ref. 47. The resulting ice standard sample ($65\text{ mm} \times 22\text{ mm} \times 0.25\text{ mm}$) was subjected to laser raster scanning under the optimized experimental conditions outlined in Table 1. The procedure targeted approximately half of the sample's surface for about 7 minutes at a laser fluence of 7 J cm^{-2} . Maintaining a stable signal during continuous laser scanning has been challenging. Fluctuations in the water vapour signal, as shown in Fig. 3a, are most likely attributed to the inherent acceleration and deceleration of the stage during scanning, and the potential irregularities on the sample's surface. Both factors can significantly affect the laser ablation process, leading to variability in both the water vapour signal and isotopic measurements. Allan variance analysis (Fig. 3b), calculated for $\delta^{18}\text{O}$ and δD over different integration times using the 6-minute segment of the data (highlighted with grey color (Fig. 3a)), further confirmed this instability. Correcting the isotopic signal for the CRDS analyzer's humidity response did not significantly alter the observed fluctuations (Fig. S1 and

S2†). While the fluctuating water vapour levels indicate inconsistencies in the amount of sample ablated and transported to the CRDS analyzer, the uncorrelated isotopic signal suggests additional factors are influencing isotopic measurements, beyond the analyzer's sensitivity to varying water vapour concentrations. These factors might include, but are not limited to, variations in the ablation process itself leading to isotopic fractionation or other complexities related to the overall LA-CRDS analyzer performance. The variability of the isotopic signal over long ablation durations and large sample areas, further supports the chosen approach of discrete sampling, which utilizes short ablation durations (90 seconds) on small sample areas $4\text{ mm} \times 4\text{ mm}$ and exploits short periods of relative stability to obtain more reliable isotopic data.

3.2.2 VSMOW two-point calibration. Raw data acquired by the LA-CRDS for $\delta^{18}\text{O}$ and δD are derived based on the internal calibration line of the CRDS analyzer. However, to address potential instrumental drift and biases, a VSMOW calibration was performed before proceeding to further data analysis. To implement this, LA-CRDS measurements were conducted on three ice standard samples—TD, NVL, and NS—prepared using the corresponding internal water isotope standards, with known $\delta^{18}\text{O}$ and δD values determined *via* conventional CRDS (reported on the VSMOW-SLAP scale in Table 2).

Four samples of each standard were prepared in separate holes in the metal holder. These holes, designated S1, S2, M1, and M2, correspond to different sizes (small hole 1, small hole 2, medium hole 1, and medium size hole 2). All samples representing a single standard were assumed to share a uniform isotopic composition. Three raster scan measurements ($4\text{ mm} \times 4\text{ mm}$) were conducted per sample: the initial scan at the surface, Layer 1, followed by two measurements, Layer 2 and Layer 3, conducted 100–150 micrometers deeper than the preceding one. This approach aimed to test whether replicate measurements could be obtained from the same area without requiring sample removal or additional preparation steps. The measurement workflow is shown schematically in Fig. 4.

Measurements were conducted on two separate days, utilizing a laser fluence of 8.7 J cm^{-2} on Day 1 and 9.7 J cm^{-2} on Day 2. The data obtained is presented across two graphs (Fig. 5a) for both laser fluence levels, detailed by the sample ID, which integrates the standard name, hole designation, and layer number, reflecting the sequence and depth of measurements. Fig. 5a shows water vapour peaks and the δD signal, with highlighted time windows indicating the LA scanning analysis periods. For constructing a two-point calibration line, the peaks corresponding to Layer 1 of the second replicates measured for the TD and NS standards, specifically 'TD S1 1'

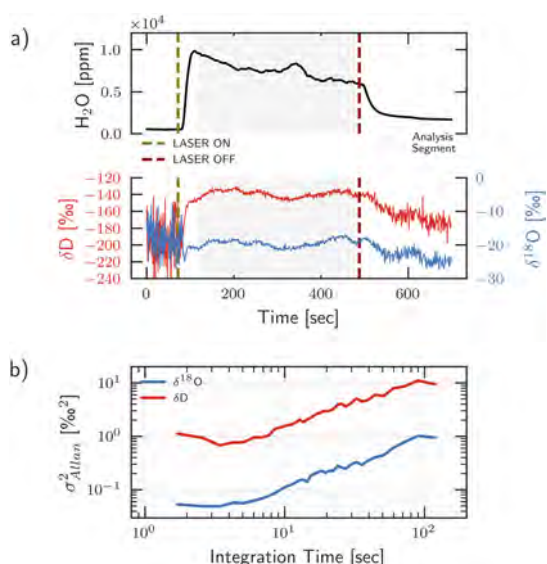


Fig. 3 Water vapour concentration and δD (red) and $\delta^{18}\text{O}$ (blue) signal (a) across a 7-minute LA raster scan of NS ice, marked by dashed lines. The grey area highlights the data segment analyzed used for the (b) Allan variance plots for δD and $\delta^{18}\text{O}$.

Table 2 Water isotopic composition of liquid laboratory standards

Standard sample	$\delta^{18}\text{O}$ [‰]	δD [‰]
TD	-38.82	-307.00
NVL	-31.15	-240.02
NS	-15.37	-112.62



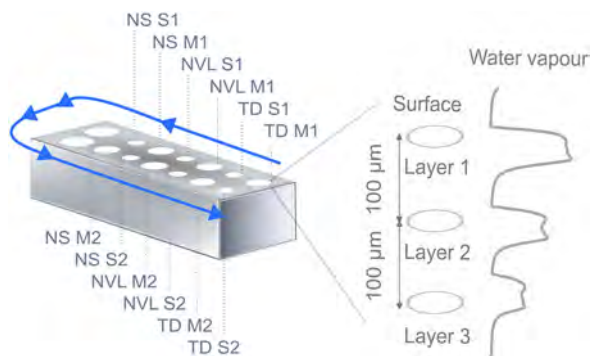


Fig. 4 Schematic of the measurement workflow for three ice standard water LA-CRDS analysis. Four samples per standard (TD, NVL, NS) are placed in specific holder holes (S1, S2, M1, M2). Each sample undergoes three measurements: an initial surface scan (Layer 1) followed by two deeper scans (Layers 2 and 3) at 100 μm intervals. The right panel shows the corresponding water vapour signal for each layer.

and 'NS S1 1' (highlighted in purple), were selected to minimize the impact of potential memory effects from prior measurements. The remaining peaks, depicted in grey, were classified as 'unknowns' to assess the technique's precision and accuracy.

Calibration lines for $\delta^{18}\text{O}$ and δD were established based on the mean values of 36 data points collected over a 30-second interval (Fig. 5b), along with their known reference values. The calibration coefficients for $\delta^{18}\text{O}$ at a fluence of 8.7 J cm^{-2} are $a_{\text{VSMOW}} = 0.99$ and $b_{\text{VSMOW}} = 0.32$, and for 9.7 J cm^{-2} , they are $a_{\text{VSMOW}} = 0.98$ and $b_{\text{VSMOW}} = -1.44$. For δD , the coefficients at 8.7 J cm^{-2} are $a_{\text{VSMOW}} = 1.08$ and $b_{\text{VSMOW}} = 28.47$, and at 9.7 J cm^{-2} , they are $a_{\text{VSMOW}} = 1.09$ and $b_{\text{VSMOW}} = 23.99$. The raw time series data were then calibrated using the following formula:

$$\delta_{\text{VSMOW}} = a_{\text{VSMOW}} \cdot \delta_{\text{measured}} + b_{\text{VSMOW}} \quad (1)$$

3.2.3 Extraction of VSMOW water isotope values. The water isotopic values were derived by computing the mean and stan-

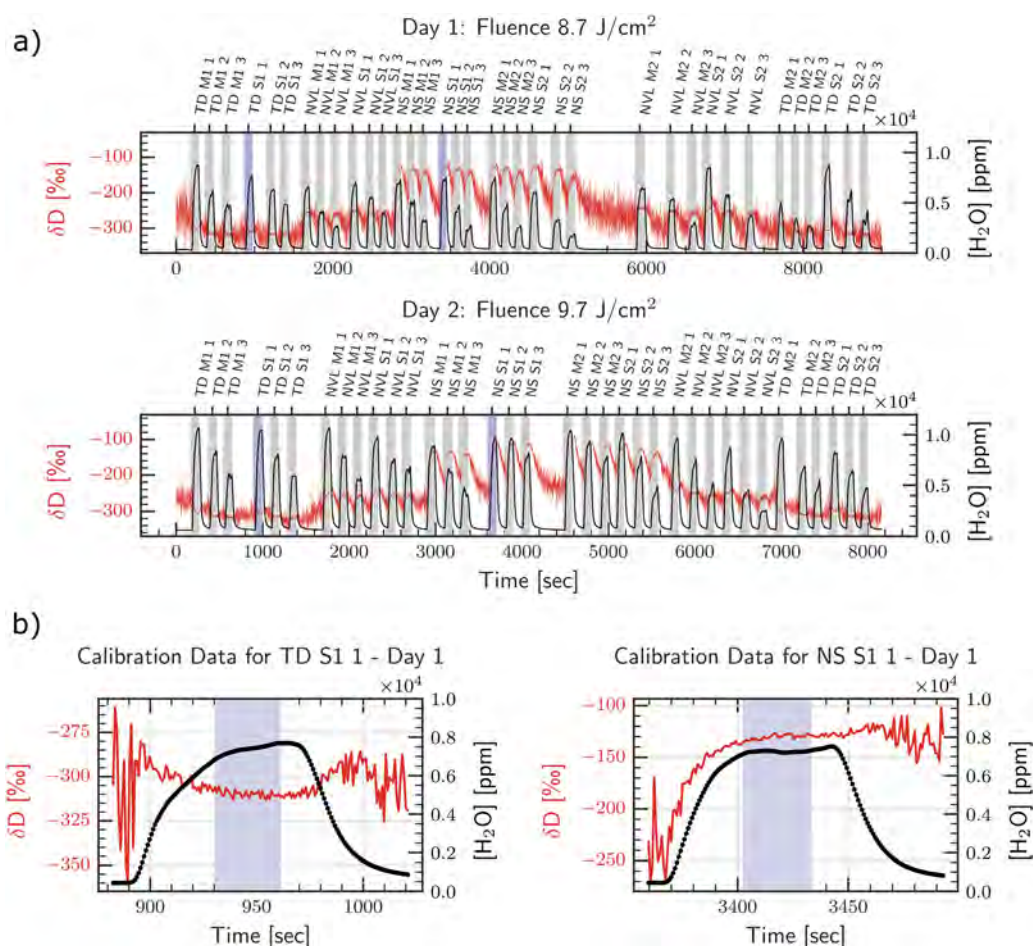


Fig. 5 (a) Time series of δD and water vapour signals for TD, NVL, and NS standards over two days at laser fluences of 8.7 J cm^{-2} (top) and 9.7 J cm^{-2} (bottom). Sample IDs include the standard name, hole designation, and layer number. Shaded regions represent the laser ablation time windows for 'unknown' samples (grey) and calibration peaks (purple). (b) Calibration data showing the selected peaks from the second replicates of TD and NS standards ('TD S1 1' and 'NS S1 1' - Day 1). The shaded regions indicate the 30-second analysis time windows used to determine the mean values for constructing calibration equations.



standard deviation during the stable phase of each peak from the calibrated data, using a 30-second data window. Although minor variations in peak shape were observed due to scanning duration and laser fluence, the data extraction process remained consistent across all peaks with the same time intervals used for statistical analysis. Tables 3 and 4 present the results for all the standard samples measured. The mean standard deviation within individual layers and across all measurements is also detailed, providing insights into measurement repeatability. The corresponding mean deviation from known values is also calculated to offer an assessment of overall accuracy throughout the experimental runs.

The water vapour concentrations, as shown in Tables 3 and 4, vary across layers and fluence levels. At a fluence of 8.7 J cm^{-2} , the highest vapour content is observed in Layer 1 (7205 ppm), decreasing to 3159 ppm in Layer 3. A similar pattern is observed at a higher fluence of 9.7 J cm^{-2} with water vapour content starting at 9335 ppm in Layer 1 and decreasing to 5316 ppm in Layer 3, which suggest that increased laser energy enhances vaporization. This is consistent with previous

findings that show that relative amounts of gas and particulate phases produced by laser ablation are dependent on both laser fluence and laser wavelength, with higher energy density and longer wavelengths generating more vapour during laser ablation.⁴⁸ However, the decreasing water vapour signals from deeper layers, despite laser focus adjustments by 100–150 μm to compensate for material removal and target subsequent layers, suggest that the initial ablation events may significantly alter the laser-ice interaction leading to less efficient material removal. The ablation process can create an uneven surface through crater formation with microstructural changes which can obscure the camera's view, making it challenging to maintain precise laser focus as ablation progresses. This, in turn, could lead to less efficient laser energy coupling with the target ice layer, resulting in reduced water vapour generation.

Although the calibrated isotopic values for the standards follow the expected trend (Fig. 6a), achieving accurate isotopic measurements for $\delta^{18}\text{O}$ and δD remains a significant challenge, for both surface and deeper layers analyzed. The data show increasing mean deviation from known values with

Table 3 Results for ice standards measured at fluence 8.7 J cm^{-2}

ID	[H ₂ O]/ppm	$\delta^{18}\text{O}$ (‰)	SD	δD (‰)	SD	$\Delta\delta^{18}\text{O}$ (‰)	Z-Score	$\Delta\delta\text{D}$ (‰)	Z-Score
TD M1 1	8480	-38.26	0.36	-300.90	1.77	-0.56	1.55	-6.10	3.46
TD M1 2	5822	-38.92	0.46	-314.05	2.31	0.10	-0.21	7.05	-3.06
TD M1 3	4605	-38.91	0.61	-315.66	2.50	0.09	-0.15	8.66	-3.46
TD S1 1	7374	-38.82	0.30	-307.00	1.99	-0.00	0.00	0.00	0.00
TD S1 2	6242	-39.11	0.39	-315.72	1.88	0.29	-0.74	8.72	-4.64
TD S1 3	4816	-39.08	0.50	-317.79	2.15	0.26	-0.51	10.79	-5.02
NVL M1 1	6403	-31.19	0.37	-248.39	2.48	0.04	-0.11	8.37	-3.37
NVL M1 2	4045	-31.51	0.58	-250.86	2.94	0.36	-0.63	10.84	-3.69
NVL M1 3	2624	-31.34	0.78	-254.24	4.39	0.19	-0.24	14.22	-3.24
NVL S1 1	6737	-31.24	0.31	-243.55	1.75	0.09	-0.28	3.53	-2.02
NVL S1 2	5520	-31.34	0.37	-246.41	2.27	0.19	-0.50	6.39	-2.81
NVL S1 3	3802	-31.38	0.58	-249.12	3.64	0.23	-0.40	9.10	-2.50
NS M1 1	6915	-15.59	0.43	-117.91	2.99	0.23	-0.53	5.29	-1.77
NS M1 2	4888	-15.55	0.54	-117.23	2.62	0.19	-0.36	4.61	-1.76
NS M1 3	3137	-16.56	0.71	-125.36	3.75	1.20	-1.68	12.74	-3.40
NS S1 1	7247	-15.36	0.36	-112.62	2.54	-0.00	0.00	0.00	-0.00
NS S1 2	4347	-15.38	0.61	-116.36	3.30	0.02	-0.03	3.74	-1.13
NS S1 3	2392	-16.46	0.89	-129.47	5.24	1.10	-1.23	16.85	-3.21
NS M2 1	7123	-15.44	0.37	-110.77	1.61	0.08	-0.21	-1.85	1.15
NS M2 2	4418	-15.41	0.43	-114.63	2.91	0.05	-0.12	2.01	-0.69
NS M2 3	2561	-16.26	0.77	-126.83	4.93	0.90	-1.17	14.21	-2.88
NS S2 1	6008	-15.14	0.39	-110.24	2.12	-0.22	0.56	-2.38	1.12
NS S2 2	3248	-15.89	0.61	-120.85	3.38	0.53	-0.87	8.23	-2.44
NS S2 3	1718	-17.05	1.06	-142.16	8.30	1.69	-1.60	29.54	-3.56
NVL M2 1	6385	-30.36	0.36	-234.60	2.71	-0.79	2.17	-5.42	2.00
NVL M2 2	5293	-31.04	0.42	-243.78	2.48	-0.11	0.25	3.76	-1.52
NVL M2 3	2903	-31.12	0.84	-248.16	4.57	-0.03	0.03	8.14	-1.78
NVL S2 1	8398	-31.34	0.39	-240.06	2.14	0.19	-0.48	0.04	-0.02
NVL S2 2	5647	-31.37	0.36	-246.27	2.71	0.22	-0.60	6.25	-2.31
NVL S2 3	3681	-31.56	0.63	-251.62	2.58	0.41	-0.65	11.60	-4.50
TD M2 1	4636	-34.91	0.56	-283.94	3.20	-3.91	6.99	-23.06	7.21
TD M2 2	3196	-37.30	0.57	-305.08	3.83	-1.52	2.70	-1.92	0.50
TD M2 3	2606	-36.89	0.71	-304.19	4.25	-1.93	2.70	-2.81	0.66
TD S2 1	8393	-37.99	0.30	-302.31	1.62	-0.83	2.76	-4.69	2.88
TD S2 2	5241	-38.19	0.50	-311.74	2.49	-0.63	1.27	4.74	-1.90
TD S2 3	3061	-38.09	0.61	-314.91	3.70	-0.73	1.21	7.91	-2.14
Layer 1	7205		0.36		2.13	-0.20		-0.36	
Layer 2	4826		0.49		2.76	-0.03		5.37	
Layer 3	3159		0.72		4.17	0.28		11.75	
All	4868		0.54		3.10	0.04		6.13	



Table 4 Results for ice standards measured at fluence 9.7 J cm⁻²

ID	[H ₂ O]/ppm	δ ¹⁸ O (‰)	SD	δD (‰)	SD	Δδ ¹⁸ O (‰)	Z-Score	ΔδD (‰)	Z-Score
TD M1 1	10 214	-39.00	0.36	-306.75	1.33	0.18	-0.49	-0.25	0.19
TD M1 2	8021	-39.16	0.32	-318.39	1.61	0.34	-1.05	11.39	-7.09
TD M1 3	5890	-39.97	0.43	-319.84	1.89	1.15	-2.70	12.84	-6.78
TD S1 1	10 113	-38.83	0.35	-307.05	1.51	0.01	-0.04	0.05	-0.04
TD S1 2	7760	-39.27	0.34	-319.18	1.60	0.45	-1.33	12.18	-7.59
TD S1 3	5888	-39.85	0.42	-321.85	1.78	1.03	-2.44	14.85	-8.32
NVL M1 1	10 297	-32.76	0.38	-252.24	2.69	1.61	-4.28	12.22	-4.54
NVL M1 2	7796	-32.57	0.25	-252.41	2.04	1.42	-5.75	12.39	-6.07
NVL M1 3	5491	-33.49	0.41	-257.33	2.16	2.34	-5.65	17.31	-8.01
NVL S1 1	9313	-33.05	0.40	-247.99	2.09	1.90	-4.70	7.97	-3.80
NVL S1 2	7312	-33.60	0.36	-252.74	2.26	2.45	-6.77	12.72	-5.64
NVL S1 3	6414	-33.46	0.41	-255.37	1.94	2.31	-5.68	15.35	-7.90
NS M1 1	8710	-17.27	0.59	-123.81	3.73	1.91	-3.25	11.19	-3.00
NS M1 2	6313	-16.94	0.34	-122.78	2.50	1.58	-4.64	10.16	-4.06
NS M1 3	4201	-18.70	0.45	-131.96	3.06	3.34	-7.40	19.34	-6.32
NS S1 1	9461	-15.36	0.30	-112.45	2.89	0.00	-0.01	-0.17	0.06
NS S1 2	9538	-13.36	0.35	-100.14	1.90	-2.00	5.74	-12.48	6.57
NS S1 3	7853	-13.11	0.33	-101.35	2.10	-2.25	6.89	-11.27	5.38
NS M2 1	10 220	-15.49	0.24	-111.07	2.33	0.13	-0.55	-1.55	0.67
NS M2 2	9105	-13.92	0.49	-103.68	3.00	-1.44	2.95	-8.94	2.98
NS M2 3	7447	-14.09	0.32	-106.34	2.64	-1.27	3.99	-6.28	2.38
NS S2 1	9838	-16.91	0.29	-114.14	2.33	1.55	-5.31	1.52	-0.65
NS S2 2	6944	-16.44	0.34	-118.03	2.44	1.08	-3.22	5.41	-2.21
NS S2 3	4216	-18.24	0.63	-130.05	3.67	2.88	-4.56	17.43	-4.75
NVL M2 1	9193	-32.48	0.41	-239.65	1.88	1.33	-3.29	-0.37	0.20
NVL M2 2	6868	-32.46	0.36	-248.75	2.12	1.31	-3.65	8.73	-4.11
NVL M2 3	4683	-33.25	0.47	-254.56	2.12	2.10	-4.46	14.54	-6.84
NVL S2 1	8142	-32.42	0.54	-247.09	1.99	1.27	-2.37	7.07	-3.55
NVL S2 2	4254	-33.57	0.58	-255.30	3.08	2.42	-4.18	15.28	-4.97
NVL S2 3	2485	-34.21	0.74	-259.01	5.83	3.06	-4.14	18.99	-3.26
TD M2 1	9308	-38.81	0.30	-305.07	1.81	-0.01	0.03	-1.93	1.07
TD M2 2	6472	-38.83	0.38	-312.07	2.45	0.01	-0.03	5.07	-2.07
TD M2 3	4744	-39.23	0.47	-315.75	3.17	0.41	-0.86	8.75	-2.76
TD S2 1	8112	-38.01	0.38	-298.90	1.78	-0.81	2.13	-8.10	4.54
TD S2 2	6144	-39.66	0.38	-318.80	2.05	0.84	-2.21	11.80	-5.76
TD S2 3	4478	-40.20	0.52	-321.79	2.72	1.38	-2.68	14.79	-5.45
Layer 1	9335		0.39		2.20	0.91		2.78	
Layer 2	7211		0.37		2.25	0.70		6.97	
Layer 3	5316		0.47		2.76	1.37		11.38	
All	7167		0.41		2.41	1.00		7.30	

sample depth, indicating reduced accuracy for subsequent layers analyzed at greater depths. At a fluence of 8.7 J cm⁻², mean deviation for δ¹⁸O is -0.20‰ in Layer 1, -0.03‰ in Layer 2, and 0.28‰ in Layer 3, while for δD, it is -0.36‰, 5.37‰, and 11.75‰, respectively. This trend is exacerbated at a higher fluence of 9.7 J cm⁻² especially for δ¹⁸O, with the deviation increasing at 0.91‰ in Layer 1, 0.70‰ in Layer 2, and 1.37‰ in Layer 3, indicating a pronounced influence of fluence on measurement accuracy. At the same laser fluence, deviation values for δD are 2.78‰, 6.97‰, and 11.38‰, for the respective layers.

The deviation from the known values (Fig. 6b) shows a slight trend towards isotopic depletion for both δ¹⁸O and δD, although it exhibits some variability, indicating both depletion and enrichment. This trend is particularly pronounced at higher laser fluences, suggesting that isotopic fractionation towards lighter isotopes in the analyzed vapour phase is amplified with increasing laser energy input. The data further prove that, on average, the measured isotopic values tend to be lower than the expected values. Both elemental and isotopic fraction-

ation have been investigated in aerosols produced by LA and analyzed by ICP-MS, with studies indicating that more volatile species are present in the gas phase rather than in the particulate phase,⁴⁹⁻⁵² which in this study would partially explain the depleted gas phase. Other effects like melting zones and recondensation which are linked with the ablation process could also contribute to the overall fractionation. However, understanding the mechanisms underlying isotopic fractionation of the gas-phase product during LA-CRDS is beyond the scope of this study.

In depth profile analysis, it was observed that the most substantial fractionation occurs in deeper layers, particularly when considering δD values. The higher fluence causes greater deviations but follows a similar trend for the accuracy over multiple layers. Both the efficiency of material removal and the accuracy of isotopic measurements are influenced by the accumulating effects of prior ablations which alter the micro-environment, including structural modifications and recondensation, and so the exposed surface for each subsequent analysis. Therefore, observed deviations from expected values



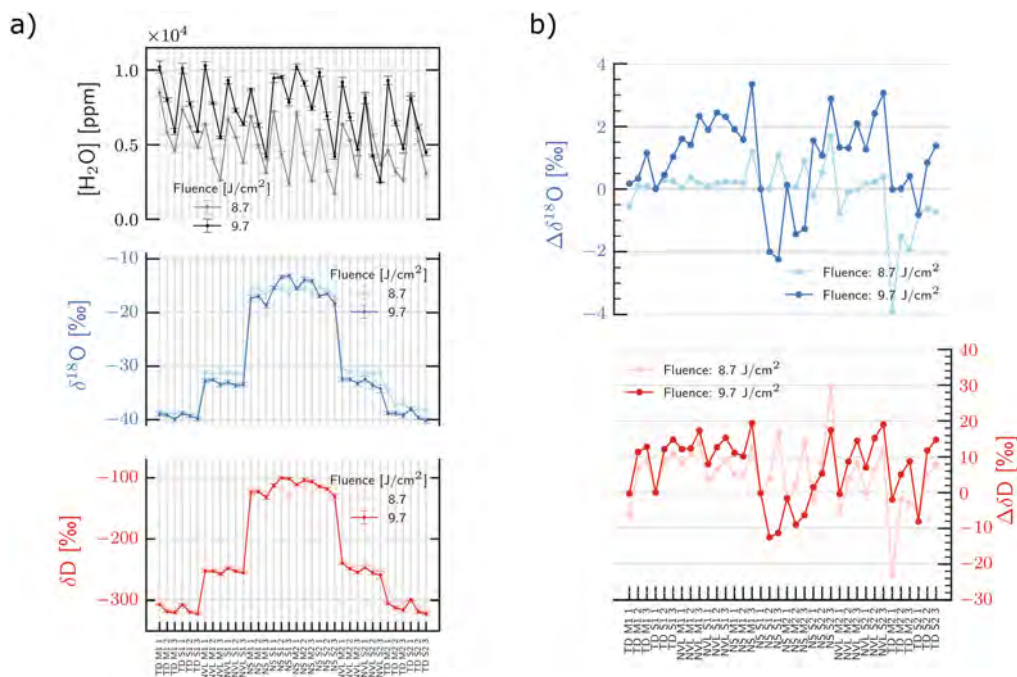


Fig. 6 Calibrated results for TD, NVL, NS ice standard samples (a) and difference between known and calibrated values of $\delta^{18}\text{O}$ and δD (b), analyzed at fluences of 8.7 and 9.7 J cm^{-2} .

in deeper layers, along with reduced water vapour signals, highlight the complex relationship between laser fluence, ice matrix properties, and effects of previous ablation events.

The mean SD values that were calculated for each layer, reveal a clear trend in the measurement variability: as water vapour content increases, the standard deviation for both isotopes decrease, suggesting higher water vapour content leads to more precise isotopic measurements. Specifically, at a fluence of 8.7 J cm^{-2} , the average standard deviation for $\delta^{18}\text{O}$ ranges from 0.36‰ in Layer 1 to 0.72‰ in Layer 3, with deeper layers represented by lower water vapour levels, and for δD from 2.13‰ to 4.17‰ , while at 9.7 J cm^{-2} , the average standard deviation values for $\delta^{18}\text{O}$ range from 0.39‰ to 0.47‰ and δD from 2.20‰ to 2.76‰ for the respective layers.

Fig. 7 shows the relationship between the standard deviation of $\delta^{18}\text{O}$ and δD with water vapour content at both fluence levels. The increase in the mass of ice ablated, which is reflected in the higher production of water vapour contributes to more stable isotopic measurements. Standard deviation values for both $\delta^{18}\text{O}$ and δD decrease up to a water vapour concentration until they reach a plateau between $6000\text{--}8000 \text{ ppm}$ achieved at a fluence of 8.7 J cm^{-2} . This trend of decreasing variability with increasing water vapour concentration is similarly observed at higher energy of 9.7 J cm^{-2} ; however, the initial standard deviations are lower due to the greater mass ablated, leading to a high signal captured in the detector.

Despite these observations, when the humidity concentration exceeds 8000 ppm , specifically at 9.7 J cm^{-2} , there is an observed increase in the variability of standard deviation

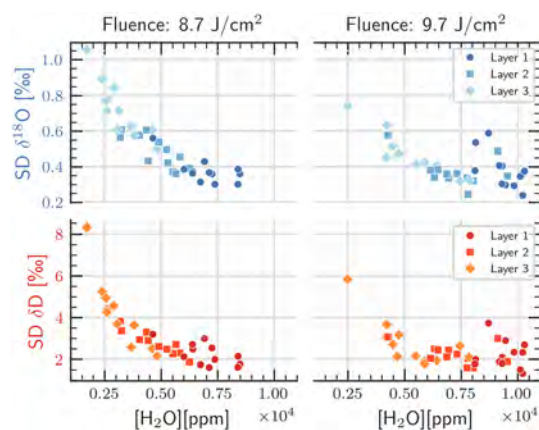


Fig. 7 Standard deviation of isotopic ratios $\delta^{18}\text{O}$ and δD across different fluence levels and layers plotted against the mean water vapour concentration for ice standards data.

values. This increase, despite the generation of more water vapour, likely results from further enhanced but “uncontrolled” ablation. Uncontrolled ablation seems to produce variable amounts of ablated mass and consequently variable water vapour levels, as evidenced by the mean water vapour values for each layer (in ppm), along with the average of their respective standard deviations (8.7 J cm^{-2} : 7205 (Mean SD: 100), 4826 (Mean SD: 117), 3159 (Mean SD: 99) and 9.7 J cm^{-2} : 9335 (Mean SD: 255), 7211 (Mean SD: 155), 5316 (Mean SD: 184)). Increased fluctuations in uncontrolled water vapour production may introduce variability in isotopic fractionation,



ultimately compromising the precision of isotopic measurements. A similar transition between a well-defined and an enhanced but uncontrolled ablation regime has been previously described in the study of impurities in ice cores through LA-ICP-MS. Although observed at a lower fluence threshold than in this study, an additional dependency was found for ice impurity standards on their elemental concentration, laser spot size and fluence.⁴⁷ The results obtained here further highlight this crucial consideration for LA-CRDS analysis of ice: the need to balance sufficient water vapour generation for robust signal intensity with maintaining a controlled ablation process to minimize isotopic fractionation arising from variable ablation volumes, especially at higher fluences.

3.3 LA-CRDS on Antarctic ice core section

A 50 mm × 10 mm section of an ice core from Neumayer Station, Antarctica, was measured by LA-CRDS. The cutting scheme of the core is shown in Fig. S4.† Measurements were conducted on 4 mm × 4 mm segments, covering the ice

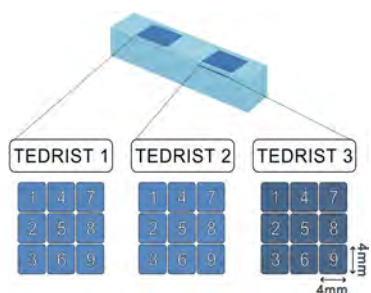


Fig. 8 Schematic diagram of the laser scanning pattern on the TEDRIST ice core section. The areas are divided into three TEDRIST regions with different fluence levels used during LA-CRDS analysis. TEDRIST 1 and TEDRIST 2 were ablated with a laser fluence of 8.7 J cm⁻² and TEDRIST 3 with 9.7 J cm⁻².

section (Fig. S5†) as depicted in the schematic of the laser scanning pattern (Fig. 8). Surface measurements with a laser fluence of 8.7 J cm⁻² (TEDRIST 1 and TEDRIST 2, indicated in blue) were performed on the same day the standards were measured with the same fluence (Day 1). Subsequent measurements targeted a deeper part of the core at a higher laser fluence of 9.7 J cm⁻² (TEDRIST 3, in dark blue), conducted on the same day as the standards measured with 9.7 J cm⁻² (Day 2). For these latter measurements, the previously ablated area was scraped to ensure a clean flat surface for analysis. Ice core data were calibrated using the specific calibration lines developed for each fluence level, with final isotopic values calculated by averaging data over consistent 30-second intervals. The results for all variables measured, including water vapour, $\delta^{18}\text{O}$, and δD , are presented in Tables 5 and 6.

The water vapour concentrations produced in both laser fluence levels are similar, unlike the vapour produced when ice standards were analyzed, where higher fluence resulted in higher water vapour concentrations. This suggests that the laser couples differently with the ice core compared to the ice standards. Additionally, the water vapour levels for the ice core are lower than those obtained for the respective fluence during surface measurements on the ice standards, further indicating a distinct interaction between the laser and different ice matrices.

The calibrated isotopic values were compared against the reference water isotope values determined by Discrete-CRDS Analysis ($\delta^{18}\text{O}$: -21.34‰ and δD : -165.4‰). The isotopic measurements of $\delta^{18}\text{O}$ and δD for the ice core data reveal significant deviations from expected values (Fig. 9). At the lower laser fluence of 8.7 J cm⁻², both $\delta^{18}\text{O}$ and δD values are overestimated, as indicated by the mean deviations ($\delta^{18}\text{O} = -1.47\text{‰}$ and $\delta\text{D} = -4.77\text{‰}$) and Z-scores in Table 5. On the other hand, at the higher fluence of 9.7 J cm⁻², an underestimation is evident, with mean deviations ($\delta^{18}\text{O} = 1.28\text{‰}$ and $\delta\text{D} = 8.94\text{‰}$) as shown in Table 6. The deviation of the derived iso-

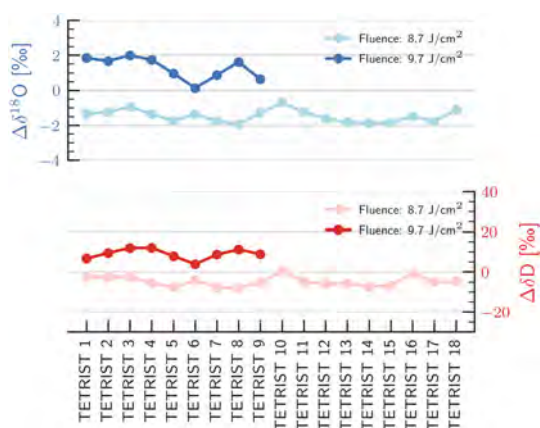
Table 5 Results for TEDRIST ice core section measured at fluence 8.7 J cm⁻²

ID	[H ₂ O]/ppm	$\delta^{18}\text{O}$ (‰)	SD	δD (‰)	SD	$\Delta\delta^{18}\text{O}$ (‰)	Z-Score	$\Delta\delta\text{D}$ (‰)	Z-Score
TEDRIST 1	5599	-20.00	0.37	-162.92	2.55	-1.34	3.62	-2.48	0.97
TEDRIST 2	4980	-20.10	0.41	-162.96	2.24	-1.24	3.00	-2.44	1.09
TEDRIST 3	4783	-20.39	0.49	-162.90	2.57	-0.95	1.94	-2.50	0.97
TEDRIST 4	4387	-19.99	0.40	-160.02	2.42	-1.35	3.36	-5.38	2.22
TEDRIST 5	6033	-19.59	0.50	-157.87	2.12	-1.75	3.50	-7.53	3.55
TEDRIST 6	5943	-19.97	0.38	-161.20	2.09	-1.37	3.60	-4.20	2.02
TEDRIST 7	6078	-19.58	0.33	-157.80	1.99	-1.76	5.32	-7.60	3.82
TEDRIST 8	5853	-19.41	0.37	-157.49	1.83	-1.93	5.16	-7.91	4.32
TEDRIST 9	6149	-20.05	0.40	-160.23	2.00	-1.29	3.24	-5.17	2.58
TEDRIST 10	5188	-20.65	0.43	-165.88	3.42	-0.69	1.62	0.48	-0.14
TEDRIST 11	4844	-20.09	0.51	-160.62	2.88	-1.25	2.45	-4.78	1.66
TEDRIST 12	4197	-19.72	0.60	-159.30	5.26	-1.62	2.72	-6.10	1.16
TEDRIST 13	5473	-19.53	0.47	-159.85	2.61	-1.81	3.83	-5.55	2.13
TEDRIST 14	5088	-19.45	0.40	-158.07	3.72	-1.89	4.70	-7.33	1.97
TEDRIST 15	4853	-19.50	0.45	-158.69	2.59	-1.84	4.05	-6.71	2.59
TEDRIST 16	5230	-19.85	0.49	-164.48	3.69	-1.49	3.04	-0.92	0.25
TEDRIST 17	4830	-19.55	0.46	-160.39	3.38	-1.79	3.89	-5.01	1.48
TEDRIST 18	5187	-20.23	0.46	-160.62	2.45	-1.11	2.44	-4.78	1.95
All	5261		0.44		2.77	-1.47		-4.77	



Table 6 Results for TEDRIST ice core section measured at fluence 9.7 J cm^{-2}

ID	[H ₂ O]/ppm	$\delta^{18}\text{O}$ (‰)	SD	δD (‰)	SD	$\Delta\delta^{18}\text{O}$ (‰)	Z-Score	$\Delta\delta\text{D}$ (‰)	Z-Score
TEDRIST 1	5176	-23.18	0.41	-172.04	3.00	1.84	-4.49	6.64	-2.22
TEDRIST 2	5594	-23.01	0.44	-174.87	2.88	1.67	-3.79	9.47	-3.29
TEDRIST 3	4597	-23.33	0.55	-177.35	3.31	1.99	-3.61	11.95	-3.61
TEDRIST 4	4831	-23.07	0.36	-177.40	3.15	1.73	-4.77	12.00	-3.81
TEDRIST 5	5577	-22.32	0.44	-173.33	2.81	0.98	-2.22	7.93	-2.82
TEDRIST 6	6200	-21.47	0.40	-169.25	2.61	0.13	-0.33	3.85	-1.47
TEDRIST 7	5303	-22.22	0.45	-174.04	2.69	0.88	-1.93	8.64	-3.21
TEDRIST 8	4426	-22.96	0.47	-176.60	2.88	1.62	-3.44	11.20	-3.89
TEDRIST 9	5262	-21.98	0.43	-174.23	2.88	0.64	-1.48	8.83	-3.06
All	5218		0.44		2.91	1.28		8.94	

**Fig. 9** Difference between known and calibrated values of $\delta^{18}\text{O}$ and δD for the ice core section at laser fluences of 8.7 and 9.7 J cm^{-2} .

topic values from expected values on ice core analysis do not align well with those obtained on ice standards, despite using the same calibration parameters for each fluence, likely because the calibration standards are not fully matrix matched, as some differences in ablation characteristics have been observed between artificial and glacier ice at high fluences.⁴⁷

The mean standard deviation values for $\delta^{18}\text{O}$ and δD indicate that the variability for the two sets of measurements is similar, likely due to the similar water vapour levels, and closely matches the values obtained for the ice standards at the same water vapour concentration range. Although the isotopic fractionation response to laser fluence is non-uniform, the similar measurement variability suggests that the method maintains a level of consistency comparable to that of the ice standards.

3.4 LA-CRDS in ice core isotope analysis

Unlike the existing ice sampling methods in ice core studies, which are combined with a CRDS analyzer, and require either the discrete melting of cut ice pieces (10 mm in length) or the continuous melting/vaporizing of an entire ice core section (55 cm or 100 cm in length) for water isotope analysis,¹⁶ the laser ablation system presented here showed capabilities of minimal sample preparation and sample consumption that

allow the preservation of the analyzed sample for further analysis. Laser ablation offers the possibility for accurate depth registration which is critical for the extraction of high-quality isotopic time series. The new system can analyze samples with maximum dimensions of $50 \text{ mm} \times 10 \text{ mm} \times 10 \text{ mm}$, achieving a sampling resolution of 4 mm, comparable to that achieved by conventional sampling methods, with potential for even higher resolution, crucial for both resolving thin layers in the deep sections of an ice core and restoring isotopic signal, achieving high-resolution temporal profiles. Sequential ablation scans over the same area are not recommended. The challenges associated with refocusing the laser beam due to crater formation and the potential alteration of isotopic composition in deeper layers by recondensation processes can compromise the accuracy of the measurements. Despite current limitations in precision and accuracy, the qualitative agreement between observed and established values opens new possibilities for ice core research highlighting the method's promise for future applications in water isotope analysis. Implementing the LA-CRDS technique in ice core studies necessitates the use of a laser source with properties that minimize laser ablation-induced isotopic fractionation while generating high concentrations of water vapour. Testing high power lasers with shorter pulse durations could potentially meet these requirements and achieve the highest possible resolution, ideally extending to the micrometer scale. Additionally, developing larger ablation chambers to accommodate standard ice core dimensions will broaden the applicability of this technique. These advancements will enable LA-CRDS to function as a micro-destructive method, providing high-quality water isotope data with the precision and accuracy needed to capture even the most intricate climate signals, potentially in a continuous mode.

4 Conclusions

This study presents a novel technique for analyzing water isotopes in ice samples by coupling a commercial laser ablation system, equipped with a nanosecond ArF (193 nm) laser, with a CRDS water isotope analyzer. This method successfully generates a gas phase product from ablated ice for isotopic analysis. A discrete sampling approach ensures relatively stable



water vapour and corresponding water isotope signals, enabling qualitative isotopic characterization. Water vapour production and isotopic composition, calibrated to the VSMOW-SLAP scale, exhibit strong dependence on laser ablation parameters. Sequential ablation at greater depths of ice standards revealed reduced water vapour levels and increasing isotopic deviations with successive ablations, likely due to a complex interplay between challenging refocusing conditions with depth and fractionation due to recondensation of the pre-ablated material. Surface measurements also displayed discrepancies, potentially arising from ablation-induced fractionation or transport effects, with higher fluences exacerbating these deviations. Ice core analysis further confirmed that the observed signal variability originated from limitations in the laser ablation system's performance, rather than inhomogeneities within the ice standards and introduced the need for matrix-matched standards that demonstrate a comparable ablation response to ice core samples. Unlocking the full potential of high-resolution LA-CRDS for ice core analysis requires lasers with high power output and short pulse durations to enhance water vapour generation from sample areas smaller than the millimeter scale, while minimizing laser-induced isotopic fractionation, ultimately enabling the extraction of detailed high-quality paleoclimatic records.

Data availability

Data for this article, including liquid CRDS analysis on ice standards and LA-CRDS on ice standards and ice core samples are available at Zenodo: LA_CRDS_WATER_ISOTOPE_ICE_CORES_RAW_DATA at <https://doi.org/10.5281/zenodo.13152033>.

The code used for data analysis is available on GitHub at: https://github.com/EiriniNBI/LA_CRDS_Water_Isotope.git.

Conflicts of interest

The authors have declared that there are no potential conflicts of interest.

Acknowledgements

The authors would like to thank Maria Hörhold, Melanie Behrens and Matthias Hüther from Alfred Wegener Institute for providing the TEDRIST sample used for intercomparison exercises within the BEOIC (Beyond Epica-Oldest Ice Core) Water Isotope Consortium, which was instrumental in this study for testing the LA-CRDS technique. This work has received funding by the European Union's Horizon 2020 Research and Innovation Program under Marie Skłodowska-Curie Grant Agreement No. 955750. Pascal Bohleber gratefully acknowledges funding from the European Union's Horizon 2020 Research and Innovation Program under the Marie Skłodowska-Curie Grant Agreement No. 101018266. Vasileios Gkinis acknowledges support from the Villum Foundation

(Project No. 00022995, 00028061), the Danish Independent Research Fund (DFG Grant No. 10.46540/2032-00228B) and Carlsberg Foundation (project 2013_01_0899, CF21-0199).

References

- 1 J. Jouzel and V. Masson-Delmotte, *Quat. Sci. Rev.*, 2010, **29**, 3683–3689.
- 2 J. Jouzel, *Water Stable Isotopes: Atmospheric Composition and Applications in Polar Ice Core Studies*, Elsevier, 2014, pp. 213–256.
- 3 *Environmental Isotopes in The Hydrological Cycle*, ed. W. Mook, International Atomic Energy Agency and United Nations Educational, Scientific and Cultural Organization, 2000, vol. 1.
- 4 W. Dansgaard, *Tellus A*, 2012, **16**, 436.
- 5 E. C. Members, *Nature*, 2004, **429**, 623–628.
- 6 N. Members, *Nature*, 2004, **431**, 147–151.
- 7 D. A. Lilien, D. Steinhage, D. Taylor, F. Parrenin, C. Ritz, R. Mulvaney, C. Martín, J.-B. Yan, C. O'Neill, M. Frezzotti, H. Miller, P. Gogineni, D. Dahl-Jensen and O. Eisen, *Cryosphere*, 2021, **15**, 1881–1888.
- 8 A. Chung, F. Parrenin, D. Steinhage, R. Mulvaney, C. Martín, M. G. P. Cavitte, D. A. Lilien, V. Helm, D. Taylor, P. Gogineni, C. Ritz, M. Frezzotti, C. O'Neill, H. Miller, D. Dahl-Jensen and O. Eisen, *Cryosphere*, 2023, **17**, 3461–3483.
- 9 C. Holme, V. Gkinis and B. M. Vinther, *Geochim. Cosmochim. Acta*, 2018, **225**, 128–145.
- 10 K. Pol, V. Masson-Delmotte, S. Johnsen, M. Bigler, O. Cattani, G. Durand, S. Falourd, J. Jouzel, B. Minster, F. Parrenin, C. Ritz, H. Steen-Larsen and B. Stenni, *Earth Planet. Sci. Lett.*, 2010, **298**, 95–103.
- 11 F. S. L. Ng, *Cryosphere*, 2023, **17**, 3063–3082.
- 12 E. Crosson, *Appl. Phys. B: Lasers Opt.*, 2008, **92**, 403–408.
- 13 E. Kerstel and L. Gianfrani, *Appl. Phys. B: Lasers Opt.*, 2008, **92**, 439–449.
- 14 I. S. Begley and C. M. Scrimgeour, *Anal. Chem.*, 1997, **69**, 1530–1535.
- 15 M. Gehre, H. Geilmann, J. Richter, R. A. Werner and W. A. Brand, *Rapid Commun. Mass Spectrom.*, 2004, **18**, 2650–2660.
- 16 V. Gkinis, T. J. Popp, T. Blunier, M. Bigler, S. Schüpbach, E. Kettner and S. J. Johnsen, *Atmos. Meas. Tech.*, 2011, **4**, 2531–2542.
- 17 B. D. Emanuelsson, W. T. Baisden, N. A. N. Bertler, E. D. Keller and V. Gkinis, *Atmos. Meas. Tech.*, 2015, **8**, 2869–2883.
- 18 T. R. Jones, J. W. C. White, E. J. Steig, B. H. Vaughn, V. Morris, V. Gkinis, B. R. Markle and S. W. Schoenemann, *Atmos. Meas. Tech.*, 2017, **10**, 617–632.
- 19 E. J. Steig, T. R. Jones, A. J. Schauer, E. C. Kahle, V. A. Morris, B. H. Vaughn, L. Davidge and J. W. White, *Front. Earth Sci.*, 2021, **9**, 640292.



- 20 R. E. Russo, X. Mao and O. V. Borisov, *TrAC, Trends Anal. Chem.*, 1998, **17**, 461–469.
- 21 H. Reinhardt, M. Kriews, H. Miller, O. Schrems, C. Lüdke, E. Hoffmann and J. Skole, *Anal. Bioanal. Chem.*, 2001, **370**, 629–636.
- 22 M. Burger, P. J. Skrodzki, L. A. Finney, J. Hermann, J. Nees and I. Jovanovic, *Phys. Plasmas*, 2018, **25**(8), 083115.
- 23 C. Li, Q. Li, L. Li, B. Men, H. Wu, D. Wu, R. Hai, X. Wu and H. Ding, *Spectrochim. Acta, Part B*, 2023, **206**, 106735.
- 24 H. Reinhardt, M. Kriews, H. Miller, C. Lüdke, E. Hoffmann and J. Skole, *Anal. Bioanal. Chem.*, 2003, **375**, 1265–1275.
- 25 W. Müller, J. M. G. Shelley and S. O. Rasmussen, *J. Anal. At. Spectrom.*, 2011, **26**, 2391.
- 26 P. Bohleber, M. Roman, M. Šala and C. Barbante, *J. Anal. At. Spectrom.*, 2020, **35**, 2204–2212.
- 27 P. Bohleber, M. Roman, M. Šala, B. Delmonte, B. Stenni and C. Barbante, *Cryosphere*, 2021, **15**, 3523–3538.
- 28 B. N. Chichkov, C. Momma, S. Nolte, F. Alvensleben and A. Tünnermann, *Appl. Phys. A: Mater. Sci. Process.*, 1996, **63**, 109–115.
- 29 F. Poitrasson, X. Mao, S. S. Mao, R. Freydier and R. E. Russo, *Anal. Chem.*, 2003, **75**, 6184–6190.
- 30 J. Koch, S. Schlamp, T. Rösgen, D. Fliegel and D. Günther, *Spectrochim. Acta, Part B*, 2007, **62**, 20–29.
- 31 M. Shaheen, J. Gagnon and B. Fryer, *Chem. Geol.*, 2012, **330–331**, 260–273.
- 32 K. M. Peensoo, MSc thesis, *Physics of Ice, Climate and Earth*, University of Copenhagen, 2021.
- 33 E. Malegiannaki, K. M. Peensoo, P. Bohleber and V. Gkinis, *Past Global Changes Magazine*, 2023, vol. 31, pp. 64–65.
- 34 S. G. Warren and R. E. Brandt, *J. Geophys. Res.: Atmos.*, 2008, **113**, D14220.
- 35 S. B. Sneed, P. A. Mayewski, W. Sayre, M. J. Handley, A. V. Kurbatov, K. C. Taylor, P. Bohleber, D. Wagenbach, T. Erhardt and N. E. Spaulding, *J. Glaciol.*, 2015, **61**, 233–242.
- 36 N. E. Spaulding, S. B. Sneed, M. J. Handley, P. Bohleber, A. V. Kurbatov, N. J. Pearce, T. Erhardt and P. A. Mayewski, *Environ. Sci. Technol.*, 2017, **51**, 13282–13287.
- 37 D. Della Lunga, W. Müller, S. O. Rasmussen and A. Svensson, *J. Glaciol.*, 2014, **60**, 970–988.
- 38 D. Della Lunga, W. Müller, S. O. Rasmussen, A. Svensson and P. Vallenga, *Cryosphere*, 2017, **11**, 1297–1309.
- 39 S. J. M. Van Malderen, A. J. Managh, B. L. Sharp and F. Vanhaecke, *J. Anal. At. Spectrom.*, 2016, **31**, 423–439.
- 40 T. V. Acker, S. J. V. Malderen, T. Buckle and F. Vanhaecke, *High-speed sub-micrometer imaging of sub-cellular structures in single cells using ARIS*, Teledyne Cetac Technologies Inc. technical report, 2017.
- 41 P. Bohleber, N. Stoll, M. Rittner, M. Roman, I. Weikusat and C. Barbante, *Geochem., Geophys., Geosyst.*, 2023, **24**, e2022GC010595.
- 42 S. M. Eggins, R. Grün, M. T. McCulloch, A. W. Pike, J. Chappell, L. Kinsley, G. Mortimer, M. Shelley, C. V. Murray-Wallace, C. Spötl and L. Taylor, *Quat. Sci. Rev.*, 2005, **24**, 2523–2538.
- 43 D. N. Douglas, A. J. Managh, H. J. Reid and B. L. Sharp, *Anal. Chem.*, 2015, **87**, 11285–11294.
- 44 S. J. Van Malderen, T. Van Acker and F. Vanhaecke, *Anal. Chem.*, 2020, **92**, 5756–5764.
- 45 E. J. Steig, V. Gkinis, A. J. Schauer, S. W. Schoenemann, K. Samek, J. Hoffnagle, K. J. Dennis and S. M. Tan, *Atmos. Meas. Tech.*, 2014, **7**, 2421–2435.
- 46 M. Šala, V. S. Šelih, C. C. Stremtan, T. Tămaş and J. T. van Elteren, *J. Anal. At. Spectrom.*, 2021, **36**, 75–79.
- 47 P. Bohleber, P. Larkman, N. Stoll, D. Clases, R. Gonzalez de Vega, M. Šala, M. Roman and C. Barbante, *Geochem., Geophys., Geosyst.*, 2024, **25**, e2023GC011425.
- 48 T. Van Helden, K. Mervič, I. Nemet, J. T. van Elteren, F. Vanhaecke, S. Rončević, M. Šala and T. Van Acker, *Anal. Chim. Acta*, 2024, **1287**, 342089.
- 49 J.-L. Todol and J.-M. Mermet, *Spectrochim. Acta, Part B*, 1998, **53**, 1645–1656.
- 50 H.-R. Kuhn and D. Günther, *Anal. Chem.*, 2003, **75**, 747–753.
- 51 S. E. Jackson and D. Günther, *J. Anal. At. Spectrom.*, 2003, **18**, 205–212.
- 52 H.-R. Kuhn, N. J. Pearson and S. E. Jackson, *J. Anal. At. Spectrom.*, 2007, **22**, 547.



Chapter 6

Conclusions and Outlook

The study presented in this thesis focused on the development of a high-resolution water isotope analysis technique for ice cores using laser ablation coupled with cavity ring-down spectroscopy (LA-CRDS). This method allows direct analysis of ice without the need for melting and vaporization, providing significant improvements in terms of spatial resolution and depth registration, enhancing temporal resolution. Femtosecond and nanosecond laser ablation systems were investigated to optimize the conversion of ice into vapour while ensuring the isotopic integrity of the measurements.

The femtosecond laser ablation system, initially designed and constructed by the Water Stable Isotope group at the Physics of Ice, Climate, and Earth Department of the Niels Bohr Institute, University of Copenhagen, and further developed in this thesis, is a specialized system for laser-ablation cavity ring-down spectroscopy (LA-CRDS) measurements on ice cores for water isotope analysis. The system incorporates a high-power laser that generates femtosecond pulses at kHz repetition rates, facilitating the production of sufficient ablated material in the gas phase to meet the CRDS requirements, which typically operates by receiving water vapour mixed with dry air reaching a concentration of approximately 20000 ppm when performing either discrete liquid analysis or continuous flow analysis. The system's main components, including the optical table and a freezer functioning as a cryo cell, an open-top sample holder mounted on a linear stage, were further enhanced with an enclosure filled with dry air for the focusing optics to avoid condensation. An ablation chamber, designed to make direct contact with the sample surface around the ablation area without fully enclosing the ice sample, was 3D printed for initial evaluation. The cryo-cell's open design allows the direct use of standard-sized ice sticks assigned for water isotope analysis, eliminating the need for extensive pre-processing such as cutting and melting. Only minor scraping is needed to ensure a smooth surface, facilitating accurate laser focusing. This micro-destructive system is highly advantageous, enabling multiple analyses on the same sample, which can improve measurement precision and statistical evaluation.

Laser ablation on artificial ice was successfully performed. However, as the system is not fully operational, isotopic analyses of the produced water vapour could not be conducted. Several tests were performed on the gas-flow system to establish a low-humidity environment in both the freezer and the optics enclosure by splitting the dry air flow. Although further improvements are required to fully isolate the system from external influences and maintain low humidity inside the freezer,

stable humidity levels of 1000-1500 ppm were achieved. These conditions were sufficient for initial crater characterization and a preliminary assessment of the ablation procedure.

Crater characterization was essential for the evaluation of the ablation process on ice and the investigation of effects such as incubation under various laser ablation modes (spot ablation and line scanning for groove formation) and settings. Preliminary assessments, conducted using optical microscopy and macro photography with a microscope objective, provided valuable insights into crater morphology, while visual inspection indicated depths in the millimeter range. These assessments also provided data for simple calculations of water vapour production and determination of the flow conditions to achieve optimal water vapour concentration for the CRDS water isotopic analyzer. These initial findings indicate that the quantity of the ablated vapour may be sufficient for subsequent isotope analysis. Additionally, higher pulse energies and prolonged ablation durations led to larger crater sizes, resulting in a larger amount of ablated material. However, these conditions also introduced irregularities in crater morphology and evidence of localized melting, which necessitate further investigation and strategies to minimize their impact on the reliability of water isotope measurements.

Currently, an initial prototype of the ablation chamber has been constructed, which requires further evaluation to determine the efficiency of its sealing, sample collection, and material transfer. The custom-built nature of the fs LA-CRDS system offers flexibility, allowing modifications tailored to specific experimental needs. However, it should be noted that the system is still in the development stage and is not yet fully functional for continuous LA-CRDS measurements. Further refinements and testing are needed to achieve full operational capability, particularly in the areas of ablation efficiency, vapour collection, and system sealing. Despite these current limitations, the system represents a highly adaptable and promising approach for advancing ice core isotope analysis.

The ns LA-CRDS system developed, employing a closed design ablation chamber capable of accommodating samples up to 5 cm in length, achieved a sampling resolution of 0.4 cm along the ice core depth. This resolution is comparable to that obtained with conventional CFA-CRDS methods and enabled the detection of high-resolution water isotope signals from both ice standards and ice core samples. Although the laser spot size used was 150 μm , the system employed raster scans of multiple laser pulses over a 4 mm \times 4 mm surface area, averaging the resulting signal to provide measurements in a discrete manner.

Key findings of the research included the identification of factors affecting water vapour production and isotopic measurement quality, such as laser fluence, ablation time, and carrier gas flow rates. Isotopic fractionation was observed, although further dedicated studies are needed to fully understand its sources. Additionally, the use of LA-CRDS revealed that re-ablating the same area led to isotopic fractionation and refreezing effects, which should be avoided. Instead, depth-directional scraping of the surface is recommended for subsequent measurements to maintain data quality and minimize artifacts.

Comparative studies between the established methods, CFA-CRDS and Discrete Liquid Analysis-CRDS, and the newly developed Laser Ablation-Cavity Ring-Down Spectroscopy are essential for evaluating its accuracy. Such studies must account

for key differences in sampling resolution and volume to ensure reliable assessments. High-resolution CFA-CRDS, for example, continuously analyzes entire cross-sections of ice core samples, with each measurement providing an isotopic profile over a 0.5 cm segment, covering all of the material in the selected length along the core depth. In contrast, LA-CRDS can offer similar or higher resolution (approximately 0.4 cm) but samples a much smaller volume due to the nanometer-scale depth of ablation. Due to the smaller sample volume analyzed by LA-CRDS compared to CFA-CRDS, the specific ablation spot may not fully capture the broader isotopic variations that CFA-CRDS measures across a larger segment. Therefore, careful comparisons are essential to confirm that observed isotopic differences reflect true environmental changes rather than being influenced by the limitations of sampling size or methodology, underscoring the importance of measurement precision. To enhance accuracy and validate the new LA-CRDS technique, extensive comparisons with established water isotope liquid analysis-CRDS methods should be conducted on the same ice core samples. The micro-destructive nature of LA-CRDS allows for using the same sample for both measurements, facilitating direct cross-validation. Such comparisons are crucial for refining the LA-CRDS procedure, improving measurement accuracy, and ultimately ensuring isotopic measurements reliably reflect environmental conditions captured in ice cores.

Advancing laser ablation techniques for analyzing water isotopes in ice cores requires not only the improvement of instrumentation but also the development of preparation methods for ice standard samples, which are used for calibration to enhance measurement accuracy. Further investigation of the homogeneity of ice standards prepared with the proposed method in 5 and the development of matrix-matched standards that closely mimic the physical and isotopic properties of natural ice samples will enable more accurate and precise calibration.

Additionally, studying the gas and particulate phases produced by laser ablation using CRDS for the gas phase and ICP-MS for the particulate phase provides complementary insights into the nature of the ablated material. This combined approach could improve understanding of both techniques and the effectiveness of sampling methods for isotopic and elemental analysis.

A preliminary experiment could involve developing a synchronized system capable of simultaneously delivering a fraction of the ablated material from the same ablation event to both CRDS and ICP-MS for real-time analysis. Employing CRDS for gas analysis and ICP-MS for particulate analysis, such a system would facilitate simultaneous data acquisition, providing a comprehensive perspective on ablation dynamics. This approach needs a standardized set of laser parameters that adequately serve the requirements of both CRDS and ICP-MS and could enable direct comparison and correlation between gas and particulate phases, yielding new insights into laser-material interaction mechanisms. By providing information about material modifications and the nature of the ablated mass, this approach could significantly improve the methodologies for high-quality isotopic and elemental analysis.

In the long term, the above approach could evolve into a dual-analysis system for ice cores, enabling simultaneous isotopic and elemental measurements. This system might consist of two specialized laser setups, each optimized for a specific

type of analysis, or an adaptable laser configuration capable of dynamically adjusting parameters for both CRDS and ICP-MS. By switching laser parameters in real-time or conducting sequential analyses on the same ice core sample, the system could provide high-precision isotopic data while also analyzing chemical impurities. Such advancements would significantly improve ice core studies obtaining high-resolution isotopic measurements and detailed characterization of elemental composition while broadening the applications of ice core studies in environmental and geological research.

Finally, the spatial resolution (sampling/depth resolution) achieved by the ns LA-CRDS system can be further increased by improving the fs LA-CRDS system. The use of a high-power laser generating femtosecond pulses aims to maximize the amount of ablated material converted into the gas phase while enabling the scanning of smaller surface areas. Investigation of the sources of potential isotopic fractionation is important for employing effective strategies that can be implemented to minimize it. High-resolution isotopic analysis using LA-CRDS, enabling precise depth registration, will play a significant role in resolving highly thinned layers in deep ice cores and studying processes such as isotope diffusion, which smooths the isotopic signal. High-resolution data will contribute to signal restoration through back-diffusion (analyzing information in the spectral domain of the isotopic time series) and provide new insights into ice core research, such as diffusion along liquid veins. These advancements will improve the interpretation of paleoclimatic signals from long, continuous ice core records and improve future climate predictions, while preserving samples for subsequent analysis.

Appendix A

Laser Beam Characterization

A.1 Laser Beam profiles

A.1.1 Gaussian Beam

The output of common lasers is characterized by the standard Gaussian or TM_{00} beam mode. "Gaussian beam" refers to the distribution perpendicular to the direction of propagation where the intensity has a typical gaussian profile [Wilson et al., 1998]. The transverse profile of the *optical intensity* (irradiance), I , of the beam with given power P ($= \pi/2 \cdot I_0 \cdot w_0$) can be expressed by a Gaussian function as follows:

$$I(r, z) = |E(r, z)|^2 = I_0 \left(\frac{w_0}{w(z)} \right)^2 e^{-\frac{2r^2}{w^2(z)}} \quad (\text{A.1})$$

where the beam radius $w(z)$ is the distance from the optical axis where the intensity drops to $1/e^2$ (13.5%) of the maximum value (on the optical axis). The corresponding *amplitude*, E , also, follows a gaussian distribution in the plane transverse to propagation axis of a laser beam and it can be expressed by the following form:

$$E(r, z) = \sqrt{I_0} \frac{w_0}{w(z)} e^{-\frac{r^2}{w^2(z)}} e^{ikz + \frac{ikr^2}{2R(z)} - i\zeta(z)} \quad (\text{A.2})$$

The shape of a Gaussian beam is presented in figure A.2 and it is defined by the *beam waist*, w_0 , which is the point along the propagation axis where the beam radius reaches its minimum value.

Any field of light with wavelength λ , initially confined to a finite region of radius $r = w_0$, will be subjected to a diffractive spreading beyond a characteristic distance, the so-called *Rayleigh length*, z_R [Born et al., 1999]. Thus, the characteristic spreading of a Gaussian beam as it propagates in free space is a result of diffraction. The Rayleigh distance z_R is defined as the distance from the beam waist to the point where the beam cross-sectional area has doubled after propagating. This means that the irradiance (power/area) has dropped 50% or that beam radius has increased by a factor of $\sqrt{2}$.

$$z_R = \frac{\pi w_0^2 n}{\lambda} \quad (\text{A.3})$$

Actual laser beams exhibit some deviation from the ideal Gaussian behavior, measured by the beam quality factor, M^2 factor, which is a metric that compares a real laser beam with the corresponding diffraction-limited Gaussian beam. Rayleigh length for a real beam is defined as:

$$z_R = \frac{\pi w_0^2 n}{\lambda M^2} \quad (\text{A.4})$$

Depth of Focus is defined as twice the Rayleigh length which equals to $2 \cdot z_R$.

Beam Divergence angle, in the far field, is defined as the ratio of the beam radius $w(z)$ and the distance from the beam waist, z , for high values of z and is given by:

$$\theta \approx \tan \theta = \lim_{z \rightarrow \infty} \frac{w(z)}{z} = \lim_{z \rightarrow \infty} \frac{w_0 \sqrt{1 + \left(\frac{z}{z_R}\right)^2}}{z} = \frac{w_0}{z_R} \quad (\text{A.5})$$

$$\theta = \frac{w_0}{z_R} \quad (\text{A.6})$$

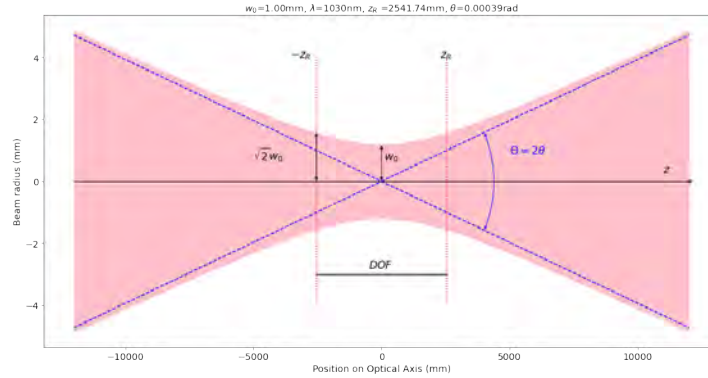


FIGURE A.1: Propagation and characteristic parameters of a laser beam operating at 1030 nm in the fs regime.

A.1.2 Bessel Beam

They are called Bessel beams, due to the particular shape in the transverse plane, which is mathematically described by a Bessel function

$$J_0(u) = \frac{1}{2\pi} \int_0^{2\pi} e^{iu \cos v} dv \quad (\text{A.7})$$

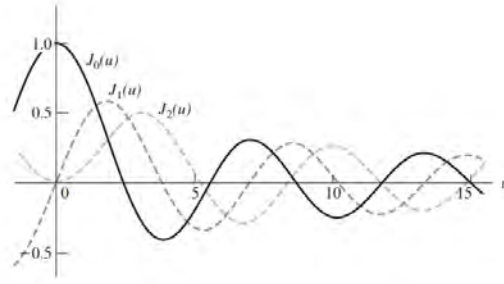


FIGURE A.2: Bessel Functions. [Hecht, 2012]

The transverse intensity profile of the BB follows a zeroth order Bessel function, which has a high intensity central peak surrounded by number of concentric rings. A Bessel beam is a wave whose amplitude is described by a Bessel function of the first kind.

Bessel beams (BBs) appear immune to diffraction over finite propagation distances due to the conical nature of light propagation along the optical axis, while at the same time BB maintain a tight focus over a relatively long depth of focus (DOF), much longer compared with the standard Gaussian beams. This results to sharp edges of features and minimal thermal effects to surrounding areas.

The ideal Bessel beam is impossible to create, as it contains an infinite amount of rings over an infinite space. Pseudo-Bessel beams, on the other hand, are confined to an aperture. Bessel beams are conical phase beams. This beam type is characterized by high aspect ratio, by the means of long beam across the direction of laser beam propagation and smaller width compared to a gaussian shaped beam.

Each of the bright rings carries the same amount of power, so that the intensity of each ring should decrease as the number of rings grows, for a given beam of finite power. The intensity of the bright central core should decrease as the number of rings increases [Hecht, 2012].

$$E_n(r, \varphi, z) = A e^{ik_z z} J_n(k_r r) e^{\pm i n \varphi} \quad (\text{A.8})$$

The diameter of the central lobe can be determined by the first zeros of the Bessel function [McGloin et al., 2005].

$$2r_b = 2\kappa / (k \sin(\theta)); \text{ where } k = 2\pi / \lambda \quad (\text{A.9})$$

The peak fluence at the central lobe can be approximated by

$$F_b = 4E_{in} / (r_b z_b \tan(\theta)) \quad (\text{A.10})$$

Axicons are used to generate zeroth-order Bessel beams.

A.2 Optical Elements

The optical elements used on the focusing optical configuration are described below:

a. Plano Convex Lens

Plano-convex lenses are optical lenses that have one spherical and one flat surface, with a positive focal length. They are used to converge or focus incoming light, ideally suited for collimation or focusing tasks with monochromatic illumination.

Given an initial laser beam waist w_0 at the lens's front focal plane, the waist size w' at the lens's back focal plane can be predicted using the modified lens formula that accounts for M^2 :

$$w' = \frac{f\lambda M^2}{\pi w_0}, \quad (\text{A.11})$$

where f is the focal length of the lens, λ is the wavelength of the laser, and M^2 is the beam quality factor, which represents the deviation of the beam from an ideal Gaussian profile, influencing its divergence and focusing behavior.

The diameter of the laser spot at the focal plane, or the minimum achievable beam waist, is then given by:

$$d_f = \frac{4\lambda M^2 f}{\pi d} \quad \text{where } d = 2w_0 \quad (\text{A.12})$$

$$\text{DOF} = 2z_R = \frac{\pi}{2\lambda M^2} d_f^2 = \frac{\pi M^2}{2\lambda} \left(\frac{4\lambda f}{\pi d} \right)^2 = \frac{8\lambda M^2}{\pi} \left(\frac{f}{d} \right)^2 \quad (\text{A.13})$$

b. Achromatic Lens

An achromatic lens effectively reduces chromatic and spherical aberrations by combining two lenses—typically a positive low-index crown glass and a negative high-index flint glass, which are inherent in a singlet lens. Achromatic doublets maintain consistent focal lengths across various wavelengths, achieving sharper focus by minimizing spherical aberrations. An achromatic lens precisely focuses a parallel beam of light to a diffraction-limited "spot". In this study, an air-spaced achromatic doublet was used (ACA254-200-B, f: 200 mm by Thorlabs) which offers superior correction for optical aberrations and exhibits greater resistance to laser damage compared to conventional achromatic doublets.

c. Beam Expander

Galilean beam expander is constructed by the use of an objective lens with a negative focal length and an image lens with a positive focal length positioned at a distance L which equals the sum of their focal lengths. This beam expander design has no internal focus and makes Galilean beam expanders ideal when working with high-power laser systems. Small beam waist results in a larger

divergence angle, while a large beam waist results in a smaller divergence angle or in other words, a more collimated beam. This is the reason why beam expanders can obtain a small beam divergence by increasing beam diameter.

In this study a fixed 3X magnification beam expander with sliding lens was used (BE03-1064 3X UVFS High-Power Beam Expander, V-Coated for 1064 nm by Thorlabs).

d. Axicon lens

Axicons, conical lenses or rotationally symmetric prisms, are optical elements that have rotational symmetry about the z-axis as they have conical surface on the one side, with the tip looking outwards, and a flat one on the other side [Khonina et al., 2021]. In most cases, the transverse cross section is a circle, as for an ordinary lens. An axicon generates a quasi-Bessel beam (a beam comprised of rings equal in power to one another) throughout its depth of focus (DOF) region, which is the overlap region of a gaussian beam passing through it, and images a point source as a line along the optical axis. The Bessel beam region may be thought of as the interference of conical waves formed by the axicon. Gradually, axicon transforms the beam into a ring shaped one with constant width and increasing radius as it propagates, so that projects a 'spot' ring beyond the DOF, in the far field regime [Litvin et al., 2008]. The important parameters that characterize an axicon are its front face radius, R , the cone angle (the inclination angle of the surface), α , and the refractive index, n . These parameters together determine the length of the DOF of the axicon:

$$\text{DOF} = \frac{R\sqrt{1 - n^2 \sin^2 \alpha}}{\sin \alpha \cos \alpha (n \cos \alpha - \sqrt{1 - n^2 \sin^2 \alpha})} \approx \frac{R}{(n - 1)\alpha} \quad (\text{A.14})$$

where R is the radius of the beam entering the axicon, n is the axicon's index of refraction, and α is the alpha angle.

The simplified equation assumes that the angle of refraction is small and becomes less accurate as α decreases. The axicon angle, α , does not change with increasing distance from the optical axis, while it would continuously change for an ordinary lens. Refraction thus leads to a constant ray deflection angle within a range of input ray positions. In the far field regime where the beam is projected far away from the axicon, the ring diameter, D_r , increases with distance, as the beam propagates in a conical phase, but the rays are non-diverging resulting to the constant thickness of the created ring along the propagation axis. The rings thickness, t_r , is equivalent to the half of the incoming laser beam's diameter, R .

$$t_r = \frac{R\sqrt{1 - n^2 \sin^2 \alpha}}{\cos \alpha (n \sin^2 \alpha + \cos \alpha \sqrt{1 - n^2 \sin^2 \alpha})} \approx R \quad (\text{A.15})$$

The simplified equation again assumes small angles of refraction. The diameter of the ring can be given by the following approximation:

$$D_r = 2L \sin \alpha \left(\frac{n \cos \alpha - \sqrt{1 - n^2 \sin^2 \alpha}}{n \sin^2 \alpha + \cos \alpha \sqrt{1 - n^2 \sin^2 \alpha}} \right) \approx 2L \tan((n - 1)\alpha) \quad (\text{A.16})$$

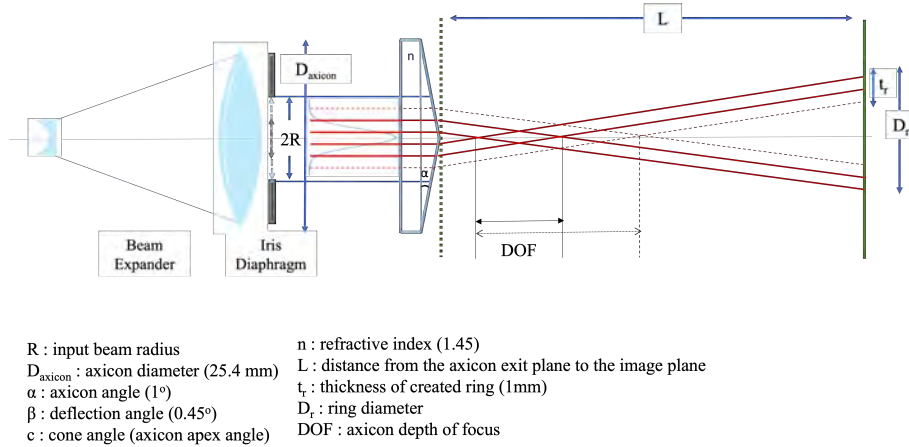


FIGURE A.3: Axicon Lens System.

In this study an 1° angle axicon lens was used (AX251-B - 1.0° , 650 - 1050 nm AR Coated UVFS, $\varnothing 1''$ ($\varnothing 25.4$ mm) Axicon by Thorlabs)

A.3 Beam profiling

A.3.1 Laser Beam Size

```

1
2 import imageio.v2 as iio
3 import numpy as np
4 import cv2
5 import matplotlib.pyplot as plt
6 from scipy.optimize import curve_fit
7 from scipy.signal import find_peaks
8 import laserbeamsize as lbs
9
10 class BeamRead:
11     def __init__(self, image_path, background_path=None, pixel_size_um=3.45,
12     ↪ lambda1=1030e-9, crop_threshold_fraction=0.01,
13     ↪ signal_threshold_fraction=0.05, beam_type='circular'):
14         # Initialize class attributes
15         self.image = iio.imread(image_path).astype(np.float32)
16         self.pixel_size_um = pixel_size_um # Pixel size in micrometers
17         self.lambda1 = lambda1
18         self.crop_threshold_fraction = crop_threshold_fraction # For cropping
19     ↪ threshold
20         self.signal_threshold_fraction = signal_threshold_fraction # For signal
21     ↪ threshold in profile preprocessing
22         self.beam_type = beam_type # 'circular' or 'gaussian'
23
24         # Convert image to grayscale if it's not already (to handle 3D image with
25     ↪ channels)
26         if len(self.image.shape) == 3:
27             self.image = cv2.cvtColor(self.image, cv2.COLOR_BGR2GRAY)
28
29         # Background subtraction if background_path is provided
30         if background_path:
31             bg = iio.imread(background_path).astype(np.float32)
32             if len(bg.shape) == 3:
  
```

```

28         bg = cv2.cvtColor(bg, cv2.COLOR_BGR2GRAY)
29         self.image -= bg
30     else:
31         # If no background image, subtract background using corner estimation and
32         ↪ tilted background
33         corner_mean, corner_std = lbs.corner_background(self.image)
34         self.image -= corner_mean
35         self.image = lbs.subtract_tilted_background(self.image)
36
37     # Normalize the grayscale image
38     self.gray = cv2.normalize(self.image, None, 0, 255,
39                             ↪ cv2.NORM_MINMAX).astype(np.uint8)
40
41     def crop_to_beam(self):
42         # Use the crop_threshold_fraction for cropping
43         _, thresholded = cv2.threshold(self.gray, np.max(self.gray) *
44         ↪ self.crop_threshold_fraction, 255, cv2.THRESH_BINARY)
45         contours, _ = cv2.findContours(thresholded, cv2.RETR_EXTERNAL,
46         ↪ cv2.CHAIN_APPROX_SIMPLE)
47         if not contours:
48             raise ValueError("No contours found in the image.")
49         largest_contour = max(contours, key=cv2.contourArea)
50         x, y, w, h = cv2.boundingRect(largest_contour)
51         return self.gray[y:y+h, x:x+w], (x, y, w, h)
52
53     def dual_gaussian(self, x, A1, mu1, sigma1, A2, mu2, sigma2, baseline):
54         return (A1 * np.exp(-(x - mu1)**2 / (2 * sigma1**2)) +
55             A2 * np.exp(-(x - mu2)**2 / (2 * sigma2**2)) + baseline)
56
57     def preprocess_profile(self, profile):
58         # Use the signal_threshold_fraction for preprocessing the profile
59         non_zero_indices = np.where(profile > np.max(profile) *
60         ↪ self.signal_threshold_fraction)[0]
61         if len(non_zero_indices) == 0:
62             raise ValueError("No significant data points found.")
63         start_index = non_zero_indices[0]
64         return profile[start_index:], start_index
65
66     def fit_beam_profile(self, profile):
67         x_data = np.arange(len(profile))
68
69         # Find peaks in the profile
70         peaks, properties = find_peaks(profile, height=np.max(profile)*0.2,
71         ↪ distance=50)
72         if len(peaks) < 2:
73             raise ValueError("Could not find two peaks in the data.")
74
75         # Sort peaks by amplitude
76         peak_heights = properties['peak_heights']
77         sorted_indices = np.argsort(peak_heights)[::-1] # Descending order
78         peaks = peaks[sorted_indices]
79         peak_heights = peak_heights[sorted_indices]
80
81         # Use the two highest peaks
82         mu1, mu2 = peaks[:2]
83         A1, A2 = peak_heights[:2]
84
85         # Ensure mu1 < mu2
86         if mu1 > mu2:
87             mu1, mu2 = mu2, mu1
88             A1, A2 = A2, A1
89
90         # Estimate the baseline level (average of the first few data points)

```

```

85     baseline = np.mean(profile[:10])
86
87     # Initial guesses for sigma
88     sigma1 = sigma2 = 30 # Adjust based on expected peak widths
89
90     initial_guess = [A1, mu1, sigma1, A2, mu2, sigma2, baseline]
91
92     try:
93         params, cov = curve_fit(self.dual_gaussian, x_data, profile,
94                                 → p0=initial_guess, maxfev=20000)
95         return params
96     except RuntimeError as e:
97         print(f"Error during fitting: {e}")
98         return None
99
100 def plot_grayscale_with_profile(self, filename='grayscale_with_profile.png'):
101     cropped_image, (x, y, w, h) = self.crop_to_beam()
102
103     # Convert pixel dimensions to micrometers
104     x_micrometers = np.linspace(0, w * self.pixel_size_um, w)
105     y_micrometers = np.linspace(0, h * self.pixel_size_um, h)
106
107     beam_profile = cropped_image[int(h/2), :] # Horizontal cross-section of the
108     → beam
109
110     # Preprocess the profile
111     beam_profile, start_index = self.preprocess_profile(beam_profile)
112
113     # Fit the beam profile
114     params = self.fit_beam_profile(beam_profile)
115     if params is None:
116         print("Fitting failed.")
117         return
118
119     # Convert x_data to micrometers, taking the start_index into account
120     x_data = (np.arange(len(beam_profile)) + start_index) * self.pixel_size_um
121     fitted_profile = self.dual_gaussian(np.arange(len(beam_profile)), *params)
122
123     # Plot the grayscale image with mirrored Y-axis for the intensity plot
124     fig, ax1 = plt.subplots(figsize=(8, 8))
125
126     # Plot grayscale image
127     ax1.imshow(cropped_image, extent=[0, w * self.pixel_size_um, 0, h *
128     → self.pixel_size_um], cmap='gray')
129     ax1.set_xlabel('Position / μm')
130     ax1.set_ylabel('Position / μm')
131     ax1.set_title('Grayscale Image with Beam Profile and Fit')
132
133     # Create secondary Y-axis for intensity plot
134     ax2 = ax1.twinx()
135     ax2.plot(x_data, beam_profile, 'r-', label='Beam Cross-Section')
136     ax2.plot(x_data, fitted_profile, 'b--', label='Dual Gaussian Fit')
137     ax2.set_ylabel('Intensity', color='red')
138     ax2.tick_params(axis='y', colors='red')
139     ax2.set_ylim([0, np.max(beam_profile) * 1.2]) # Adjust Y-limits if needed
140     ax2.legend(loc='upper right')
141
142     # Display widths (sigma) in micrometers on the plot
143     sigma1_um = params[2] * self.pixel_size_um
144     sigma2_um = params[5] * self.pixel_size_um
145
146     # Calculate FWHM from sigma
147     fwhm1_um = 2.355 * params[2] * self.pixel_size_um

```

```

145     fwhm2_um = 2.355 * params[5] * self.pixel_size_um
146
147     # Display FWHM (instead of sigma) in micrometers on the plot
148     plt.text(0.2, 0.5, f'FWHM: fwhm1 = {fwhm1_um:.2f} μm, fwhm2 = {fwhm2_um:.2f}
    ↪ μm',
149             transform=ax1.transAxes, fontsize=12, verticalalignment='top',
    ↪ color='white')
150
151     plt.savefig(filename, format='pdf', dpi=600, bbox_inches='tight')
152     plt.show()
153
154     def plot_gaussian_fit(self, filename='gaussian_fit.png'):
155         cropped_image, (x, y, w, h) = self.crop_to_beam()
156
157         plt.figure(figsize=(6, 6))
158         lbs.plot_image_analysis(cropped_image, title="Original Image  $\lambda=1030\text{nm}$ 
    ↪ beam", iso_noise=True,
159                                pixel_size=self.pixel_size_um, units='μm',
    ↪ cmap='plasma')
160         plt.savefig(filename, format='pdf', dpi=600, bbox_inches='tight')
161         plt.show()
162
163
164     # Example Usage
165     image_path_gaussianbeam = ""
166     image_path_circularbeam=""
167     background_path = None
168
169     # # # For Gaussian beam
170     # beam_reader_gaussian = BeamRead(image_path, background_path,
    ↪ crop_threshold_fraction=0.08, signal_threshold_fraction=0.01,
    ↪ beam_type='gaussian')
171     # beam_reader_gaussian.plot_gaussian_fit("gaussian_beam_fit.png")
172
173     # For Circular beam
174     beam_reader_circular = BeamRead(image_path_circularbeam, background_path,
    ↪ crop_threshold_fraction=0.008, signal_threshold_fraction=0.01,
    ↪ beam_type='circular')
175     beam_reader_circular.plot_grayscale_with_profile("circular_dualfit.pdf")
176     beam_reader_circular.plot_gaussian_fit("circular_gaussianfit.pdf")
177

```

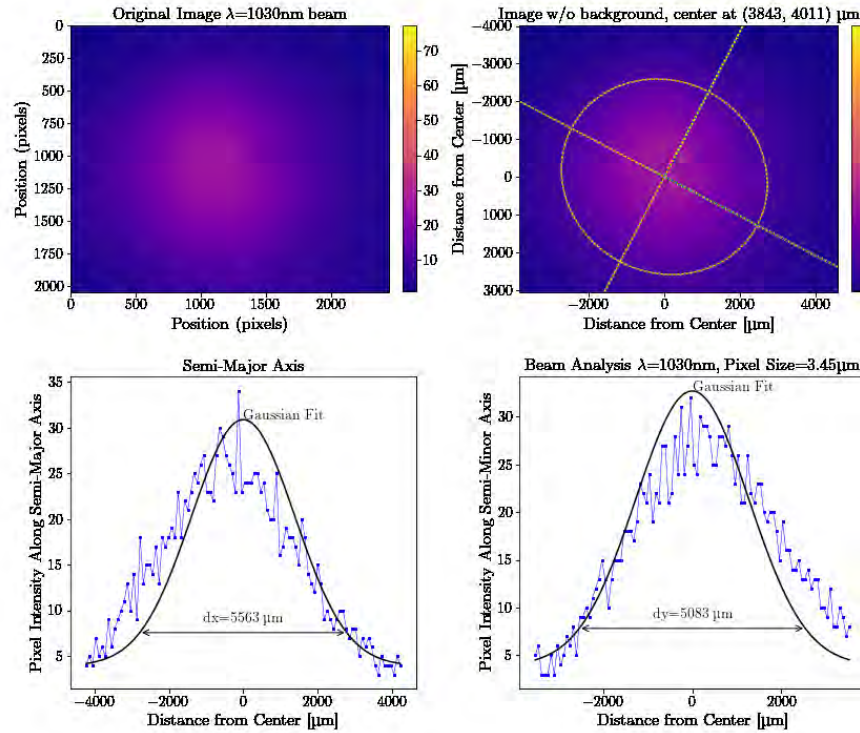


FIGURE A.4: IR laser beam spot with 3X beam expander.

Optical configuration which included a neutral density filter (NE30A-B - Ø25 mm Absorptive Neutral Density Filter, ARC: 650- 1050 nm), the 3X beam expander, an iris diaphragm, the axicon lens (AX251-B - 1.0°) was tested. The output beam of an axicon lens has either a Bessel beam profile or a ring shaped profile, beyond the depth of focus. We added a plan convex lens (f : 175 mm), so that the created beam is confined in space. Multiple images were obtained in order to investigate the change in ring size and shape when we move the lens towards the imaging system. The distance between the axicon and the imaging system was set to 340mm and the focusing lens was moving. The series of images are shown in Fig. A.5 which were analyzed using the code in A.3, as shown in Fig. A.7. The laser source used in this experiment was the 635 nm alignment laser. The input laser beam radius was about 3 mm, and the obtained beam radius by the system at the focal plane was about 1.6 mm. Different beam radius were obtained for different distances of the plano convex or doublet lens system from the imaging system and the depth of focus was determined to be around 15 mm (Fig. A.8). Ring thickness should be constant when exiting the axicon lens, it is equal to 3 mm, while at the focal point of the doublet lens it was estimated around 80 μm (Fig. A.6, using the code provided A.3). The laser ring thickness when exiting the focusing lens for different positions of the lens should also be investigated if we are to analyze the fluence applied on the irradiated area. Apart from that, when the distance between the focusing lens and the imaging system changes, the distance between the former and the axicon lens changes, as well, which may lead to different ring size of the beam light distribution recorded

by the camera. These systems are rather complicated and raytracing software could be ideal for simulations of the optical configurations and bessel beam propagation, and calculation of the DOF, as well as the ring diameter, ring thickness of the circular regime of the beam. Some tests are provided in the [A.3](#).

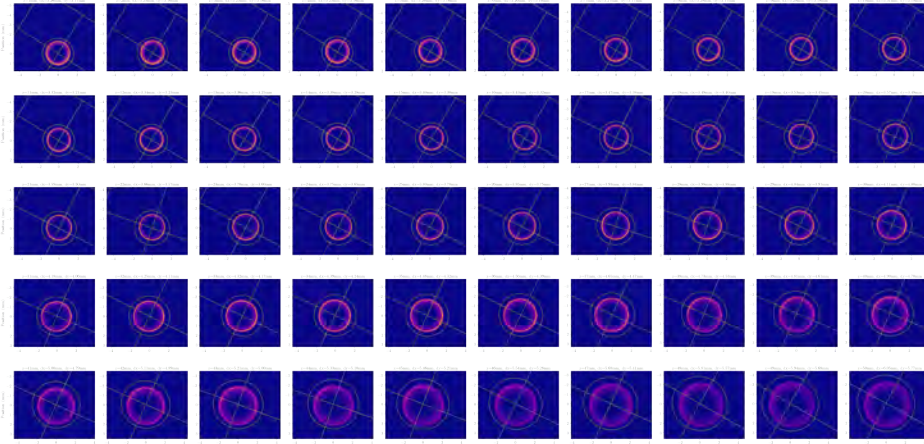


FIGURE A.5: Beam profile analysis of the ring shaped beam (alignment laser: 635 nm when moving the plano-convex lens (f : 175 mm) with respect to the imaging system.

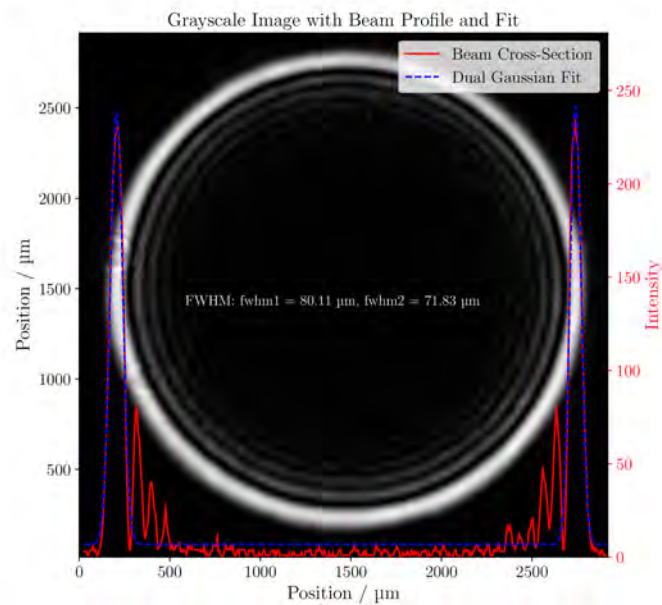


FIGURE A.6: Circular beam shape analyzed using python code [A.3](#).

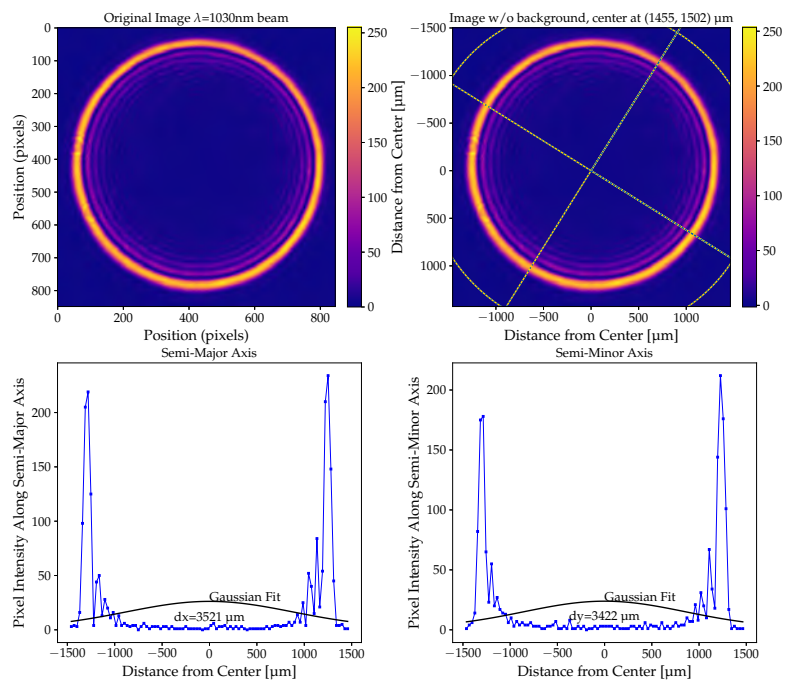


FIGURE A.7: Circular beam shape analyzed using python code [A.3](#) and laserbeamsize package.

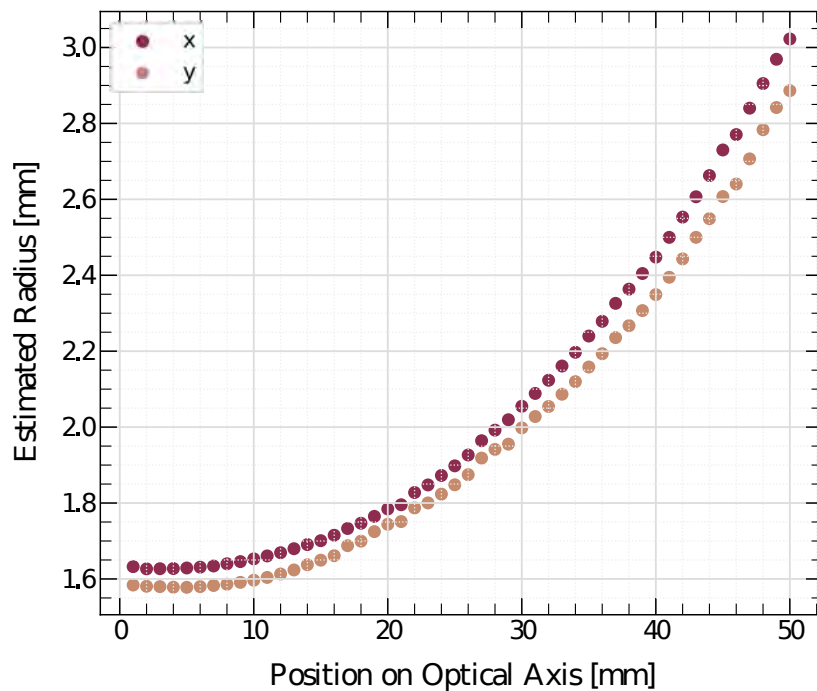


FIGURE A.8: Estimated ring radius at each position along the optical axis from the experiment of Fig. [A.5](#).

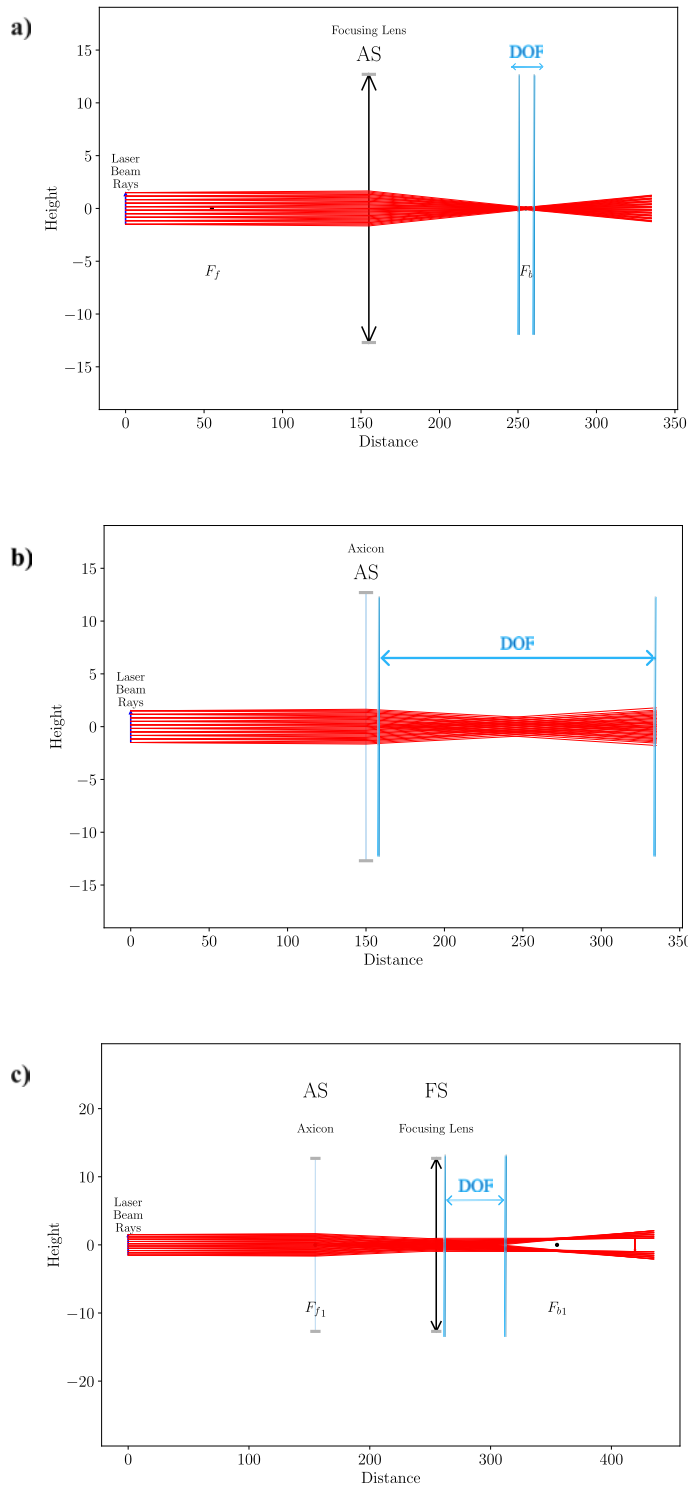


FIGURE A.9: Ray tracing diagrams illustrating laser beam propagation through different optical configurations, indicating the Depth of Focus (DOF). a) Laser beam passing through a convex lens. (b) Beam profile transformation using an axicon (c) A system of an axicon and a convex lens, illustrating changes in beam profile and extended DOF.

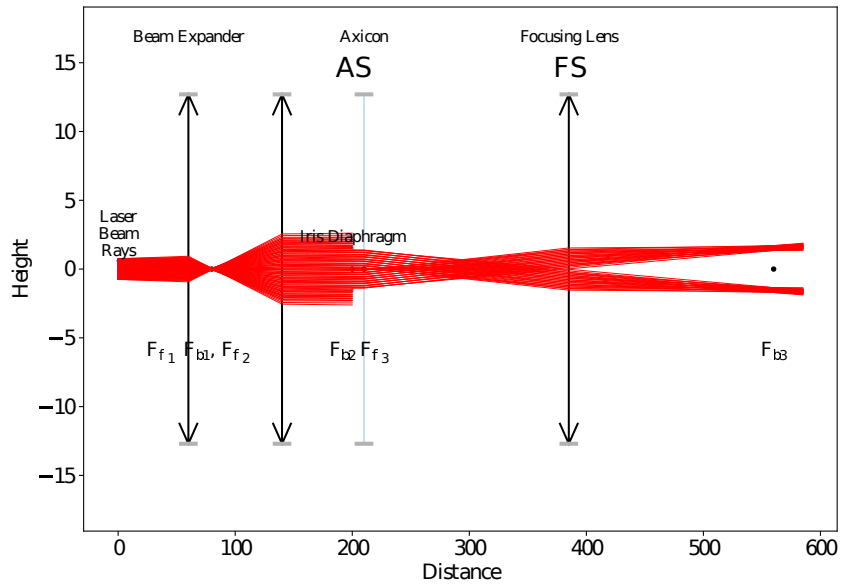


FIGURE A.10: Ray diagram of the optical configuration including a beam expander (3X), an iris diaphragm, an axicon, and a convex lens.

Appendix B

Temperature-Humidity Module

B.1 Arduino Code for Temperature Humidity Sensors

```
1 #include <DHT.h>
2 #include <DHT_U.h>
3 #include <SPI.h> //for the SD card module
4 #include <SD.h> // for the SD card
5 #include <DS3231.h> // for the RTC
6
7 //define DHT pin
8 #define DHTPIN 2 // what pin we're connected to
9 #define DHTTYPE DHT22 // DHT 22
10
11 // initialize DHT sensor for normal 16mhz Arduino
12 DHT dht(DHTPIN, DHTTYPE);
13
14 // change this to match your SD shield or module;
15 // Arduino Ethernet shield and modules: pin 4
16 // Data logging SD shields and modules: pin 10
17 // Sparkfun SD shield: pin 8
18 const int chipSelect = 4;
19
20 // RTC
21 RTC_DS1307 rtc;
22
23 void setup() {
24 //initializing the DHT sensor
25 dht.begin();
26
27 //initializing Serial monitor
28 Serial.begin(9600);
29
30 // setup for the RTC
31 while(!Serial); // for Leonardo/Micro/Zero
32 if(! rtc.begin()) {
33 Serial.println("Couldn't find RTC");
34 while (1);
35 }
36 else {
37 // following line sets the RTC to the date & time this sketch was
38 // compiled
39 rtc.adjust(DateTime(F(__DATE__), F(__TIME__)));
40 }
41 if(! rtc.isrunning()) {
42 Serial.println("RTC is NOT running!");
43 }
```

```
43
44 // setup for the SD card
45 Serial.print("Initializing SD card...");
46
47 if(!SD.begin(chipSelect)) {
48     Serial.println("initialization failed!");
49     return;
50 }
51 Serial.println("initialization done.");
52
53 //open file
54 myFile=SD.open("DATA.txt", FILE_WRITE);
55
56 // if the file opened ok, write to it:
57 if (myFile) {
58     Serial.println("File opened ok");
59     // print the headings for our data
60     myFile.println("Date,Time,Temperature C ");
61 }
62 myFile.close();
63 }
64
65
66
67 void loggingTime() {
68     DateTime now = rtc.now();
69     myFile = SD.open("DATA.txt", FILE_WRITE);
70     if (myFile) {
71         myFile.print(now.year(), DEC);
72         myFile.print('/');
73         myFile.print(now.month(), DEC);
74         myFile.print('/');
75         myFile.print(now.day(), DEC);
76         myFile.print(',');
77         myFile.print(now.hour(), DEC);
78         myFile.print(':');
79         myFile.print(now.minute(), DEC);
80         myFile.print(':');
81         myFile.print(now.second(), DEC);
82         myFile.print(",");
83     }
84     Serial.print(now.year(), DEC);
85     Serial.print('/');
86     Serial.print(now.month(), DEC);
87     Serial.print('/');
88     Serial.println(now.day(), DEC);
89     Serial.print(now.hour(), DEC);
90     Serial.print(':');
91     Serial.print(now.minute(), DEC);
92     Serial.print(':');
93     Serial.println(now.second(), DEC);
94     myFile.close();
95     delay(1000);
96 }
97
98
99 void loggingTemperature() {
100     // Reading temperature or humidity takes about 250 milliseconds!
101     // Sensor readings may also be up to 2 seconds 'old' (its a very slow
102     // sensor)
103     // Read temperature as Celsius
104     float t = dht.readTemperature();
105     // Read temperature as Fahrenheit
```

```
105 //float f = dht.readTemperature(true);
106
107 // Check if any reads failed and exit early (to try again).
108 if (isnan(t) /*|| isnan(f)*/) {
109     Serial.println("Failed to read Temp from DHT sensor!");
110     return;
111 }
112
113
114 void loggingHumidity() {
115     // Reading temperature or humidity takes about 250 milliseconds!
116     // Sensor readings may also be up to 2 seconds 'old' (its a very slow
117     // sensor)
118     // Read temperature as Celsius
119     float h = dht.readHumidity();
120
121     // Check if any reads failed and exit early (to try again).
122     if (isnan(h) /*|| isnan(f)*/) {
123         Serial.println("Failed to read RH from DHT sensor!");
124         return;
125     }
126     //debugging purposes
127     Serial.print("Humidity: ");
128     Serial.print(t);
129     Serial.println(" *C");
130     //Serial.print(f);
131     //Serial.println(" *F\t");
132
133     myFile = SD.open("DATA.txt", FILE_WRITE);
134     if (myFile) {
135         Serial.println("open with success");
136         myFile.print(t);
137         myFile.println(",");
138     }
139     myFile.close();
140 }
141
142 void loop() {
143     loggingTime();
144     loggingTemperature();
145     delay(5000);
146 }
147 // Additional functions omitted for brevity...
```

LISTING B.1: Arduino code for environmental data logging

Appendix C

Crater Characterization

C.1 Protocol for Laser Focusing

1. Measure the distance between the sample surface and the focusing lens to be equal to the focal length of the lens. Then use the laser pointer and try to focus the laser beam on the sample surface by the naked eye. You are on focus when the laser spot that reaches the sample surface or a focusing card that is placed on the sample surface has the smallest diameter. Use a metal rod as the sample target to fix this distance between the focusing lens and the sample surface.
2. Use the lowest energy possible (less than $1 \mu\text{J}$) and try to ablate a piece of paper that is placed above the ice sample.
3. Another way to do it is to focus on the metal object following the procedure with the laser pointer and then check the size and the morphology of the craters under the microscope. Usually, when changing the z position of the focusing lens using the linear stage, you can find the crater with the smallest diameter and check that the craters have some kind of depth. This is the point that the laser is tightly focused.
4. If the laser beam is to be focused on the ice surface, it is better that you have already followed the above procedures. Then the ice sample should be cut and scraped so that its height is the same as the one of the metal object used for focusing. When the ice is placed in the freezer, you can either follow steps 1 or 2.
5. Another option is to create craters in the ice while changing the z position of the focusing lens and inspect the craters under the microscope. This will help understand how tight the laser beam should be on the ice surface to drill craters.
6. When the ablation chamber is installed in the system, varying the z position of the focusing lens while monitoring the water vapour in the CRDS analyzer will allow for finding the optimal working distance between the lens and the target surface that will ensure adequate material removal. At the same time, the craters drilled can be analyzed by imaging techniques, and in this way, we can find the optimal experimental conditions, like a compromise between enough material removal for analysis and minimal heat-affected zones.

C.2 Macro Photography

C.2.1 Crater Diameter Measurement Tool

```

1  import cv2
2  import os
3  import numpy as np
4  import matplotlib.pyplot as plt
5  import matplotlib.image as mpimg
6
7
8  # Specify the folder path containing the images
9  image_folder_path = ''
10
11 # Specify the output folder where processed images will be saved
12 output_folder_path = ''
13 os.makedirs(output_folder_path, exist_ok=True)
14
15 # Global variables
16 circles = [] # List to store the circles (center_x, center_y, radius)
17 drawing = False # True if the left mouse button is down, False otherwise
18 moving = False # True if a circle is being moved
19 ix, iy = -1, -1 # Initial x and y location for drawing/moving circles
20 radius = 0 # Radius of the circle
21 microns_per_pixel = 0.17 # Conversion factor
22 selected_circle = None # Index of the selected circle for dragging
23 circle_thickness = 30 # Circle line thickness
24 scale_bar_thickness = 100 # Scale bar thickness, adjustable
25 scale_bar_font_scale = 4 # Scale bar font scale, adjustable
26 scale_bar_text_thickness = 15 # You can adjust this value for thicker or thinner
   ↪ text
27
28 # Mouse callback function
29 def draw_circle(event, x, y, flags, param):
30     global ix, iy, drawing, circles, radius, selected_circle, moving
31
32     if event == cv2.EVENT_LBUTTONDOWN:
33         # Check if the cursor is inside any existing circle for dragging
34         for i, (center_x, center_y, r) in enumerate(circles):
35             if np.sqrt((x - center_x) ** 2 + (y - center_y) ** 2) <= r +
   ↪ circle_thickness:
36                 selected_circle = i
37                 moving = True
38                 ix, iy = x, y
39                 break
40         if not moving:
41             drawing = True
42             ix, iy = x, y
43             radius = 0
44
45     elif event == cv2.EVENT_MOUSEMOVE:
46         if drawing:
47             radius = int(np.sqrt((x - ix) ** 2 + (y - iy) ** 2))
48         elif moving and selected_circle is not None:
49             # Move the circle to the new location
50             circles[selected_circle] = (x, y, circles[selected_circle][2])
51
52     elif event == cv2.EVENT_LBUTTONUP:
53         if drawing:
54             circles.append((ix, iy, radius))

```



```

55         drawing = False
56     elif moving:
57         moving = False
58         selected_circle = None
59
60     # Function to draw the circles and the diameter text
61     def draw_circles_with_diameter(img, circles):
62         for center_x, center_y, radius in circles:
63             # Draw the circle with increased thickness
64             cv2.circle(img, (center_x, center_y), radius, (0, 0, 0), circle_thickness)
65
66             # Calculate the diameter in microns
67             diameter_pixels = 2 * radius
68             diameter_microns = diameter_pixels * microns_per_pixel
69
70             # Draw the diameter in microns above each circle
71             font = cv2.FONT_HERSHEY_SIMPLEX
72             text = f"{diameter_microns:.2f}"
73             font_scale = 8 # Font scale for diameter text
74             font_thickness = 20 # Font thickness for diameter text
75             text_size = cv2.getTextSize(text, font, font_scale, font_thickness)[0]
76             text_x = center_x - text_size[0] // 2
77             text_y = center_y - radius - 10 # Adjusted for larger font size
78             cv2.putText(img, text, (text_x, text_y), font, font_scale, (0, 0, 0),
79                 ↪ font_thickness)
80
81     # Function to draw the scale bar
82     def draw_scale_bar(img):
83         global scale_bar_thickness, scale_bar_font_scale, scale_bar_text_thickness
84         scale_bar_length_microns = 100 # Length of the scale bar in microns
85         scale_bar_length_pixels = int(scale_bar_length_microns / microns_per_pixel)
86         scale_bar_y = img.shape[0] - 40 # Y-coordinate for the scale bar
87         scale_bar_x1 = img.shape[1] - 40 - scale_bar_length_pixels # Starting
88             ↪ X-coordinate
89         scale_bar_x2 = img.shape[1] - 40 # Ending X-coordinate
90         # Draw the scale bar rectangle with the specified thickness
91         cv2.rectangle(img, (scale_bar_x1, scale_bar_y - scale_bar_thickness // 2),
92             (scale_bar_x2, scale_bar_y + scale_bar_thickness // 2), (0, 0, 0),
93             ↪ -1)
94         # Draw the scale bar text with the specified font scale and text thickness
95         cv2.putText(img, f"{scale_bar_length_microns} um", (scale_bar_x1, scale_bar_y -
96             ↪ 10 - scale_bar_thickness),
97             cv2.FONT_HERSHEY_SIMPLEX, scale_bar_font_scale, (0, 0, 0),
98             ↪ scale_bar_text_thickness)
99
100     # List all files in the input folder
101     image_files = [f for f in os.listdir(image_folder_path) if
102         ↪ f.lower().endswith(('.png', '.jpg', '.jpeg', '.gif', '.bmp'))]
103
104     # Process each image in the folder
105     for image_file in image_files:
106         # Initialize circles for each image
107         circles = []
108
109         # Load the image
110         image_path = os.path.join(image_folder_path, image_file)
111         image = cv2.imread(image_path)
112         if image is None:
113             print(f"Error: Unable to load image at path {image_path}")
114             continue
115
116         # Create a window for the image
117         cv2.namedWindow(image_file, cv2.WINDOW_AUTOSIZE)

```

```
112 cv2.setMouseCallback(image_file, draw_circle)
113
114 while True:
115     # Work on a copy of the image
116     img = image.copy()
117
118     # Redraw all the circles with their diameters
119     draw_circles_with_diameter(img, circles)
120
121     # Draw the scale bar
122     draw_scale_bar(img)
123
124     # If currently drawing or moving, show the circle in progress
125     if drawing or moving:
126         cv2.circle(img, (ix, iy), radius, (0, 255, 0), circle_thickness)
127
128     cv2.imshow(image_file, img)
129     k = cv2.waitKey(1) & 0xFF
130
131     # If 'd' is pressed, delete the last circle
132     if k == ord('d') and circles:
133         circles.pop()
134
135     # If 'Esc' is pressed, close the window and exit the script
136     if k == 27: # Escape key
137         break
138
139     # If 'Enter' is pressed, save and move to the next image
140     if k == 13:
141         # Save the final image with circles and the scale bar in the output
142         # → folder
143         output_path = os.path.join(output_folder_path, image_file)
144         cv2.imwrite(output_path, img)
145         print(f"Processed and saved image: {image_file}")
146         break
147
148     # Close the window for the current image
149     cv2.destroyWindow(image_file)
150
151     # If 'Esc' key was pressed, break the loop and finish processing
152     if k == 27: # Escape key
153         print("Processing interrupted by user.")
154         break
155
156     # Destroy any remaining OpenCV windows and exit the program
157     cv2.destroyAllWindows()
158     cv2.waitKey(1)
159     cv2.waitKey(1)
160     cv2.waitKey(1)
161     cv2.waitKey(1)
162
163     print("All images processed and saved.")
164
```

C.2.2 Macro Photography System



FIGURE C.1: Macro-photography system with LED panels lighting.

Appendix D

Publications

D.1 Past Global Changes Magazine

Challenges of water-isotope measurements on ice cores

Eirini Malegiannaki^{1,2}, K. M. Peensoo¹, P. Bohleber² and V. Gkinis¹

Due to thinning of ice-core layers, the deepest part of the cores is the hardest to analyze. New micro-destructive and high-resolution instrumental approaches are necessary to retrieve a water-isotope record that accurately represents past climate variations.

Water isotopic composition of ice cores

When water travels from the evaporation to the precipitation site, the different water isotopes (H_2^{16}O , H_2^{18}O , HD^{16}O) modify its isotopic signature, represented by $\delta^{18}\text{O}$ and δD . For example, a lighter isotope, such as H_2^{16}O , evaporates more easily than a heavy one, such as H_2^{18}O , leading to a temperature-dependent fractionation and the establishment of a relationship between water isotopic composition and condensation temperature (Dansgaard 1953).

Ice cores exhibit distinctive layered characteristics where the water-isotopic signature is preserved. Due to the preservation of ice for long time periods in large ice sheets, water-isotope data offers access to a continuous and high-resolution record of past climatic variability. This is shown in the climate records generated during the EPICA (1996–2008) deep-core project which extend up to 800,000 years ago. The ongoing Beyond EPICA (2019–2026) project aims to extend the ice-core record up to 1.5 Myr in order to reconstruct Antarctica's climate history.

However, analyzing deep ice cores poses challenges. Thinning of annual layers in the deeper sections of an ice sheet, and post-depositional processes within the ice core, such as water molecule diffusion within the ice, may result in the smoothing of the water-isotope signal (Johnsen et al. 2000). This challenges the recovery of the original isotopic signal of the deposited precipitation. In addition, there are limitations in the measurement procedures which further increase difficulty in retrieving the original climate signal.

Analytical techniques for water-isotope measurements on ice cores

Advances in sample preparation and signal acquisition techniques have significantly enhanced the capability of obtaining high-resolution water-isotopic data from ice cores. Isotope Ratio Mass Spectrometry (IRMS) is an analytical technique traditionally employed to acquire water-isotope signals that offer high-precision measurements. However, due to the "sticky" nature of the water molecule, and its condensable gas phase, the water should be converted into a chemical form that is compatible with the IRMS, which is a time-consuming process and prone to inaccuracies. Laser-based

water-isotope measurement techniques display the potential to tackle the aforementioned issues (Kerstel and Gianfrani 2008), as well as other difficulties related to the expensive and bulky instrumental equipment needed.

Cavity Ring Down Spectroscopy (CRDS) is a sensitive spectroscopic technique that uses laser light and an optical cavity to measure water-isotope ratios. For the measurement, a laser pulse is injected into an optical cavity, and the decay time, or "ring down" time, of the detected light intensity is measured. This decay time is affected by the presence of gas molecules in the cavity, indicating the gas concentration. By coupling specific laser wavelengths with absorption features of the target molecules, CRDS allows for highly sensitive measurements.

CRDS has emerged as a preferred alternative to IRMS, also offering the ability to perform field measurements. Different ice-sample preparation methods enable water-isotope measurements using a CRDS analyzer in either continuous or discrete mode, respectively. However, it is important to note that both approaches require substantial time and sample consumption.

Laser Ablation: a fast micro-destructive sampling method

Laser-matter interaction has been widely used for developing new techniques,

including micromachining, laser cutting, sampling, and material development. When a pulsed laser beam is focused on a target surface, a high amount of energy is confined in space and time in the irradiated area, which can cause material ejection in the gas phase, known as Laser Ablation (LA). Ice sampling using LA serves a dual purpose: 1) It provides high-resolution analysis, and 2) it uses the smallest amount of sample possible for analysis, given the micro-destructive nature of the ablation process. In this way, the ice core is not melted and the same sample can be used for other types of analysis while, at the same time, it is possible to obtain high-quality continuous measurements.

LA has already been adopted as a sampling method in elemental concentration studies on ice cores (Della Lunga et al. 2017). Recently, LA sampling allowed for fast two-dimensional imaging of the impurities in ice at very high resolution (just a few tens of micrometers), generating new insights into ice-impurity interactions (Bohleber et al. 2021).

Laser Ablation-Cavity Ring Down Spectroscopy on ice cores

Laser Ablation (LA) and Cavity Ring Down Spectroscopy (CRDS) techniques have recently been used together to enable high-quality water-isotopic measurements on ice cores. The conceptual design of the LA-CRDS system is illustrated in Figure 1.

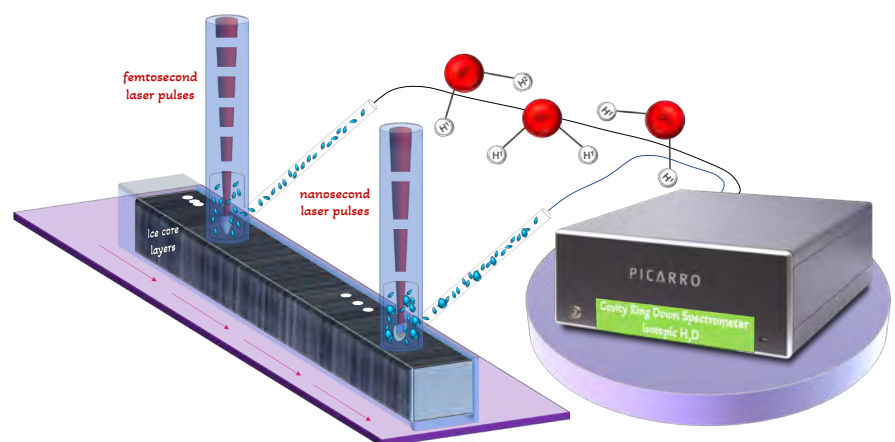


Figure 1: LA on ice-core samples using either nanosecond or femtosecond laser pulses enable material ejection in the gas phase, which is delivered to a CRDS analyzer for water-isotope detection. Placing an ice sample on a motorized stage can enable continuous high-resolution sampling.

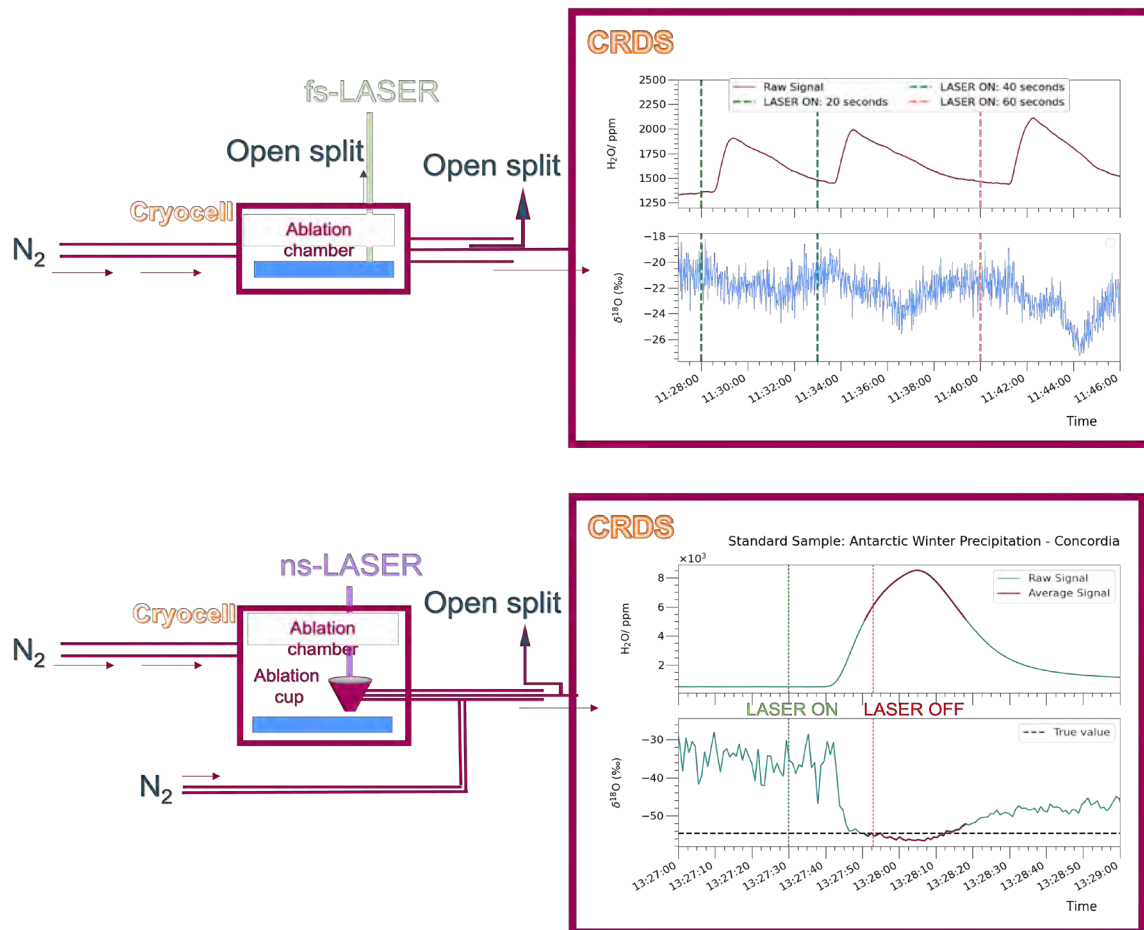


Figure 2: (A) LA-CRDS scheme using femtosecond laser pulses and a cryocell as the ablation chamber (Kerttu and Gkinis 2021). (B) LA-CRDS scheme using nanosecond laser pulses and a two-volume cryocell (ablation chamber and ablation cup). Both LA schemes led to ice ablation. The resulting vapor, H₂O, and the corresponding isotopic signal δ¹⁸O detected by the CRDS analyzer, are shown in both cases.

The experimental setup for LA sampling on ice includes essential components such as a focused laser beam, a motorized translational stage for accurate ice movement, an ablation chamber to collect the sampled material, and a transfer line that transports it to the CRDS analyzer. These components work together to enable efficient and reliable analysis of ice samples in a continuous manner.

During sampling, the laser interacts with the ice and creates a mixture of vapor and tiny particles. The laser can produce short pulses, either in the nanosecond or femtosecond range. The amount of time the laser interacts with the ice affects the composition of the mixture. One challenge in measuring water isotopes is that when the ice melts or undergoes incomplete phase changes, it can change the isotopic signature of the material being studied. However, using very short laser pulses in the femtosecond range can help reduce this issue, because the interaction time is shorter than the time it takes for heat to spread in the material.

The compatibility between the vapor produced by the LA sampling process and the gas analyzer, CRDS, led to the inception of the LA-CRDS technique. This innovative design enables fast gas-phase sample collection directly from the ice, facilitating high-quality water-isotopic measurements. The successful implementation of this approach

in experimental laboratories has yielded promising results.

Both femtosecond (Fig. 2a; Kerttu 2021) and nanosecond laser pulses (Fig. 2b) have been applied in two distinct experimental configurations coupled with a CRDS analyzer, leading to the detection of the ablated ice (artificial ice samples produced from purified and liquid water from Antarctic winter precipitation) and acquisition of the respective water-isotope signal. These initial results demonstrate the feasibility of ablating ice material with lasers of different pulse durations, and acquiring a water-isotope signal using the CRDS analyzer.

Conclusions

Advances in water-isotope measurement techniques, both on the sampling and the detection side, had already shown a big impact on the retrieval of continuous high-resolution water-isotope records from ice cores. By combining precise analyzers with melting methods, scientists can obtain detailed data.

The introduction of LA, coupled with CRDS analyzers, presents a promising approach for capturing high-resolution isotope signals, especially from the deepest parts of the ice cores. This micro-destructive technique minimizes sample usage while providing valuable insights into laser-ice interaction principles for accurate interpretation of the water-isotope instrumental signal. The synergistic work on diffusion studies (Gkinis et al.

2014; Holme et al. 2018), and the development of high-quality water-isotope measurements, will further enhance the precision of past-temperature estimations.

AFFILIATIONS

¹Physics of Ice, Climate, and Earth, Niels Bohr Institute, University of Copenhagen, Denmark
²Department of Environmental Sciences, Informatics, and Statistics, Ca' Foscari University of Venice, Italy

CONTACT

Eirini Malegiannaki: eirini.malegiannaki@nbi.ku.dk

REFERENCES

- Bohleber P et al. (2021) *The Cryosphere* 15: 3523-3538
- Dansgaard W (1953) *Tellus* 5: 461-469
- Della Lunga D et al. (2017) *The Cryosphere* 11: 1297-1309
- Gkinis V et al. (2014) *Earth Planet Sci Lett* 405: 132-141
- Holme C et al. (2018) *Geochim Cosmochim Acta* 225: 128-145
- Johnsen S et al. (2000) *Phys Ice Core Rec* 121-140
- Kerstel E, Gianfrani L (2008) *Appl Phys B Lasers Opt* 92: 439-449
- Kerttu MP (2021) MSc Thesis, University of Copenhagen, 46 pp
- Kerttu MP, Gkinis V (2021) Change in H₂O levels of a milliqu ice sample as a result of laser ablation (100kJ, 50uJ). Zenodo.

Bibliography

- Ashkenasi, D, Lorenz, M, Stoian, R, and Rosenfeld, A (1999). "Surface damage threshold and structuring of dielectrics using femtosecond laser pulses: the role of incubation". In: *Applied Surface Science* 150.1–4, pp. 101–106. ISSN: 0169-4332. DOI: [10.1016/s0169-4332\(99\)00228-7](https://doi.org/10.1016/s0169-4332(99)00228-7).
- Balling, P and Schou, J (2013). "Femtosecond-laser ablation dynamics of dielectrics: basics and applications for thin films". In: *Reports on Progress in Physics* 76.3, p. 036502. ISSN: 1361-6633. DOI: [10.1088/0034-4885/76/3/036502](https://doi.org/10.1088/0034-4885/76/3/036502).
- Barkan, E and Luz, B (2005). "High precision measurements of $^{17}\text{O}/^{16}\text{O}$ and $^{18}\text{O}/^{16}\text{O}$ ratios in H_2O ". In: *Rapid Communications in Mass Spectrometry* 19.24, pp. 3737–3742. ISSN: 1097-0231. DOI: [10.1002/rcm.2250](https://doi.org/10.1002/rcm.2250).
- Begley, I. S. and Scrimgeour, C. M. (1997). "High-Precision $\delta^2\text{H}$ and $\delta^{18}\text{O}$ Measurement for Water and Volatile Organic Compounds by Continuous-Flow Pyrolysis Isotope Ratio Mass Spectrometry". In: *Analytical Chemistry* 69.8, pp. 1530–1535. ISSN: 1520-6882. DOI: [10.1021/ac960935r](https://doi.org/10.1021/ac960935r).
- Ben-Yakar, A., Byer, R. L., Harkin, A., Ashmore, J., Stone, H., Shen, M., and Mazur, E. (2003). "Morphology of femtosecond-laser-ablated borosilicate glass surfaces". In: *Appl. Phys. Lett.* 83, 3030–3032. DOI: [10.1063/1.1619560](https://doi.org/10.1063/1.1619560).
- Berden, G., Peeters, R., and Meijer, G. (2000). "Cavity ring-down spectroscopy: Experimental schemes and applications". In: *International Reviews in Physical Chemistry* 19.4, pp. 565–607. ISSN: 1366-591X. DOI: [10.1080/014423500750040627](https://doi.org/10.1080/014423500750040627).
- Bigeleisen, J., Perlman, M. L., and Prosser, H. C. (1952). "Conversion of Hydrogenic Materials to Hydrogen for Isotopic Analysis". In: *Analytical Chemistry* 24.8, pp. 1356–1357. ISSN: 1520-6882. DOI: [10.1021/ac60068a025](https://doi.org/10.1021/ac60068a025).
- Boardman, A., Cresswell, B., and Anderson, J. (1996). "An analytical model for the laser ablation of materials". In: *Applied Surface Science* 96–98, pp. 55–60. ISSN: 0169-4332. DOI: [10.1016/0169-4332\(95\)00465-3](https://doi.org/10.1016/0169-4332(95)00465-3).
- Bohleber, P., Roman, M., Šala, M., Delmonte, B., Stenni, B., and Barbante, C. (2021). "Two-dimensional impurity imaging in deep Antarctic ice cores: snapshots of three climatic periods and implications for high-resolution signal interpretation". In: *The Cryosphere* 15.7, pp. 3523–3538. DOI: [10.5194/tc-15-3523-2021](https://doi.org/10.5194/tc-15-3523-2021).
- Bohleber, P., Roman, M., Šala, M., and Barbante, C. (2020). "Imaging the impurity distribution in glacier ice cores with LA-ICP-MS". In: *J. Anal. At. Spectrom.* 35 (10), pp. 2204–2212. DOI: [10.1039/D0JA00170H](https://doi.org/10.1039/D0JA00170H).
- Born, M and Wolf, E (1999). *Principles of Optics*. 7th. Cambridge University Press.

- Brand, W. A., Geilmann, H., Crosson, E. R., and Rella, C. W. (2009). "Cavity ring-down spectroscopy versus hightemperature conversion isotope ratio mass spectrometry; a case study on δ^2H and $\delta^{18}O$ of pure water samples and alcohol/water mixtures". In: *Rapid Communications in Mass Spectrometry* 23.12, pp. 1879–1884. ISSN: 1097-0231. DOI: [10.1002/rcm.4083](https://doi.org/10.1002/rcm.4083).
- Breitling, D., Ruf, A., and Dausinger, F. (2004). "Fundamental aspects in machining of metals with short and ultrashort laser pulses". In: *Photon Processing in Microelectronics and Photonics III*. Ed. by Herman, P. R., Fieret, J., Pique, A., Okada, T., Bachmann, F. G., Hoving, W., Washio, K., Xu, X., Dubowski, J. J., Geohegan, D. B., and Traeger, F. SPIE. DOI: [10.1117/12.541434](https://doi.org/10.1117/12.541434).
- BRESSER (2023). *BRESSER MikroCamLab*. Software available from BRESSER. Version 1.3, 3.0, 5.0, 10.0 MP. Available: <https://www.bresser.de/en/> [Accessed: Date-of-access].
- Burger, M., Schwarz, G., Gundlach-Graham, A., Käser, D., Hattendorf, B., and Günther, D. (2017). "Capabilities of laser ablation inductively coupled plasma time-of-flight mass spectrometry". In: *J. Anal. At. Spectrom.* 32 (10), pp. 1946–1959. DOI: [10.1039/C7JA00236J](https://doi.org/10.1039/C7JA00236J).
- Chang, G. and Tu, Y. (2012). "The threshold intensity measurement in the femtosecond laser ablation by defocusing". In: *Optics and Lasers in Engineering* 50.5, pp. 767–771. ISSN: 0143-8166. DOI: [10.1016/j.optlaseng.2011.12.010](https://doi.org/10.1016/j.optlaseng.2011.12.010).
- Cheng, J., Liu, C., Shang, S., Liu, D., Perrie, W., Dearden, G., and Watkins, K. (2013). "A review of ultrafast laser materials micromachining". In: *Optics Laser Technology* 46, pp. 88–102. ISSN: 0030-3992. DOI: [10.1016/j.optlastec.2012.06.037](https://doi.org/10.1016/j.optlastec.2012.06.037).
- Chichkov, B. N., Momma, C., Nolte, S., Alvensleben, F., and Tünnermann, A. (1996). "Femtosecond, picosecond and nanosecond laser ablation of solids". In: *Applied Physics A Materials Science Processing* 63.2, pp. 109–115. ISSN: 1432-0630. DOI: [10.1007/bf01567637](https://doi.org/10.1007/bf01567637).
- Christensen, B. H. and Balling, P. (2009). "Modeling ultrashort-pulse laser ablation of dielectric materials". In: *Physical Review B* 79.15, p. 155424. ISSN: 1550-235X. DOI: [10.1103/physrevb.79.155424](https://doi.org/10.1103/physrevb.79.155424).
- Chung, A., Parrenin, F., Steinhage, D., Mulvaney, R., Martín, C., Cavitte, M. G. P., Lilien, D. A., Helm, V., Taylor, D., Gogineni, P., Ritz, C., Frezzotti, M., O'Neill, C., Miller, H., Dahl-Jensen, D., and Eisen, O. (2023). "Stagnant ice and age modelling in the Dome C region, Antarctica". In: *The Cryosphere* 17.8, pp. 3461–3483. ISSN: 1994-0424. DOI: [10.5194/tc-17-3461-2023](https://doi.org/10.5194/tc-17-3461-2023).
- Cousin, H., Weber, A., Magyar, B., Abell, I., and Günther, D. (1995). "An auto-focus system for reproducible focusing in laser ablation inductively coupled plasma mass spectrometry". In: *Spectrochimica Acta Part B: Atomic Spectroscopy* 50.1, pp. 63–66. ISSN: 0584-8547. DOI: [10.1016/0584-8547\(94\)00094-c](https://doi.org/10.1016/0584-8547(94)00094-c).
- Crawford, T., Borowiec, A., and Haugen, H. (2004). "Femtosecond laser micromachining of grooves in silicon with 800 nm pulses". In: *Applied Physics A* 80.8, pp. 1717–1724. ISSN: 1432-0630. DOI: [10.1007/s00339-004-2941-2](https://doi.org/10.1007/s00339-004-2941-2).
- Crosson, E. (2008). "A cavity ring-down analyzer for measuring atmospheric levels of methane, carbon dioxide, and water vapor". In: *Applied Physics B* 92.3, pp. 403–408. ISSN: 1432-0649. DOI: [10.1007/s00340-008-3135-y](https://doi.org/10.1007/s00340-008-3135-y).
- Cuffey, K. M. and Vimeux, F. (2001). "Covariation of carbon dioxide and temperature from the Vostok ice core after deuterium-excess correction". In: *Nature* 412.6846, pp. 523–527. ISSN: 1476-4687. DOI: [10.1038/35087544](https://doi.org/10.1038/35087544).

- Dahl-Jensen, D., Mosegaard, K., Gundestrup, N., Clow, G. D., Johnsen, S. J., Hansen, A. W., and Balling, N. (1998). "Past Temperatures Directly from the Greenland Ice Sheet". In: *Science* 282.5387, pp. 268–271. ISSN: 1095-9203. DOI: [10.1126/science.282.5387.268](https://doi.org/10.1126/science.282.5387.268).
- Dallmayr, R., Goto-Azuma, K., Kjær, H. A., Azuma, N., Takata, M., Schüpbach, S., and Hirabayashi, M. (2016). "A High-Resolution Continuous Flow Analysis System for Polar Ice Cores". In: *Bulletin of Glaciological Research* 34.0, pp. 11–20. ISSN: 1884-8044. DOI: [10.5331/bgr.16r03](https://doi.org/10.5331/bgr.16r03).
- Dansgaard, W. (1964). "Stable isotopes in precipitation". In: *Tellus* 16.4, pp. 436–468. ISSN: 2153-3490. DOI: [10.1111/j.2153-3490.1964.tb00181.x](https://doi.org/10.1111/j.2153-3490.1964.tb00181.x).
- De Palo, R., Volpe, A., Gaudiuso, C., Patimisco, P., Spagnolo, V., and Ancona, A. (2022). "Threshold fluence and incubation during multi-pulse ultrafast laser ablation of quartz". In: *Optics Express* 30.25, p. 44908. ISSN: 1094-4087. DOI: [10.1364/oe.475592](https://doi.org/10.1364/oe.475592).
- Della Lunga, D., Müller, W., Rasmussen, S. O., Svensson, A., and Vallenga, P. (2017). "Calibrated cryo-cell UV-LA-ICPMS elemental concentrations from the NGRIP ice core reveal abrupt, sub-annual variability in dust across the GI-21.2 interstadial period". In: *The Cryosphere* 11.3, pp. 1297–1309. DOI: [10.5194/tc-11-1297-2017](https://doi.org/10.5194/tc-11-1297-2017).
- Di Niso, F., Gaudiuso, C., Sibillano, T., Mezzapesa, F., Ancona, A., and Lugarà, P. (2013). "Influence of the Repetition Rate and Pulse Duration on the Incubation Effect in Multiple-Shots Ultrafast Laser Ablation of Steel". In: *Physics Procedia* 41, pp. 698–707. ISSN: 1875-3892. DOI: [10.1016/j.phpro.2013.03.136](https://doi.org/10.1016/j.phpro.2013.03.136).
- Di Niso, F., Gaudiuso, C., Sibillano, T., Mezzapesa, F. P., Ancona, A., and Lugarà, P. M. (2014). "Role of heat accumulation on the incubation effect in multi-shot laser ablation of stainless steel at high repetition rates". In: *Optics Express* 22.10, p. 12200. ISSN: 1094-4087. DOI: [10.1364/oe.22.012200](https://doi.org/10.1364/oe.22.012200).
- Dinh, V. H., Hoang, L. P., Vu, Y. N. T., and Cao, X. B. (2023). "Auto-focus methods in laser systems for use in high precision materials processing: A review". In: *Optics and Lasers in Engineering* 167, p. 107625. ISSN: 0143-8166. DOI: [10.1016/j.optlaseng.2023.107625](https://doi.org/10.1016/j.optlaseng.2023.107625).
- Emanuelsson, B. D., Baisden, W. T., Bertler, N. A. N., Keller, E. D., and Gkinis, V. (2015). "High-resolution continuous-flow analysis setup for water isotopic measurement from ice cores using laser spectroscopy". In: *Atmospheric Measurement Techniques* 8.7, pp. 2869–2883. ISSN: 1867-8548. DOI: [10.5194/amt-8-2869-2015](https://doi.org/10.5194/amt-8-2869-2015).
- EPICA Community Members (2004). "Eight glacial cycles from an Antarctic ice core". In: *Nature* 429.6992, pp. 623–628. ISSN: 1476-4687. DOI: [10.1038/nature02599](https://doi.org/10.1038/nature02599).
- Epstein, S, Buchsbaum, R, Lowenstam, H, and Urey, H. C. (1951). "Carbonate-water isotopic temperature scale". In: *Geological Society of America Bulletin* 62, p. 417.
- Epstein, S and Mayeda, T (1953). "Variation of ¹⁸O content of waters from natural sources". In: *Geochimica et Cosmochimica Acta* 4.5, pp. 213–224. ISSN: 0016-7037. DOI: [10.1016/0016-7037\(53\)90051-9](https://doi.org/10.1016/0016-7037(53)90051-9).
- Gamaly, E. (2011). "The physics of ultra-short laser interaction with solids at non-relativistic intensities". In: *Physics Reports* 508.4–5, pp. 91–243. ISSN: 0370-1573. DOI: [10.1016/j.physrep.2011.07.002](https://doi.org/10.1016/j.physrep.2011.07.002).

- Gamaly, E. and Rode, A. (2013). "Physics of ultra-short laser interaction with matter: From phonon excitation to ultimate transformations". In: *Progress in Quantum Electronics* 37.5, pp. 215–323. DOI: [10.1016/j.pquantelec.2013.05.001](https://doi.org/10.1016/j.pquantelec.2013.05.001).
- Gehre, M., Geilmann, H., Richter, J., Werner, R. A., and Brand, W. A. (2004). "Continuous flow $^2\text{H}/^1\text{H}$ and $^{18}\text{O}/^{16}\text{O}$ analysis of water samples with dual inlet precision". In: *Rapid Communications in Mass Spectrometry* 18.22, pp. 2650–2660. ISSN: 1097-0231. DOI: [10.1002/rcm.1672](https://doi.org/10.1002/rcm.1672).
- Gehre, M., Hoefling, R., Kowski, P., and Strauch, G. (1996). "Sample Preparation Device for Quantitative Hydrogen Isotope Analysis Using Chromium Metal". In: *Analytical Chemistry* 68.24, pp. 4414–4417. ISSN: 1520-6882. DOI: [10.1021/ac9606766](https://doi.org/10.1021/ac9606766).
- Gkinis, V., Popp, T. J., Blunier, T., Bigler, M., Schüpbach, S., Kettner, E., and Johnsen, S. J. (2011). "Water isotopic ratios from a continuously melted ice core sample". In: *Atmospheric Measurement Techniques* 4.11, pp. 2531–2542. DOI: [10.5194/amt-4-2531-2011](https://doi.org/10.5194/amt-4-2531-2011).
- Gkinis, V., Simonsen, S., Buchardt, S., White, J., and Vinther, B. (2014). "Water isotope diffusion rates from the NorthGRIP ice core for the last 16,000 years – Glaciological and paleoclimatic implications". In: *Earth and Planetary Science Letters* 405, pp. 132–141. ISSN: 0012-821X. DOI: [10.1016/j.epsl.2014.08.022](https://doi.org/10.1016/j.epsl.2014.08.022).
- Gkinis, V., Holme, C., Kahle, E. C., Stevens, M. C., Steig, E. J., and Vinther, B. M. (2021). "Numerical experiments on firn isotope diffusion with the Community Firn Model". In: *Journal of Glaciology* 67.263, pp. 450–472. ISSN: 1727-5652. DOI: [10.1017/jog.2021.1](https://doi.org/10.1017/jog.2021.1).
- Hanuka, A., Wootton, K. P., Wu, Z., Soong, K., Makasyuk, I. V., England, R. J., and Schächter, L. (2019). "Cumulative material damage from train of ultrafast infrared laser pulses". In: *High Power Laser Science and Engineering* 7. ISSN: 2052-3289. DOI: [10.1017/hpl.2018.62](https://doi.org/10.1017/hpl.2018.62).
- Hecht, E. (2012). *Optics*. Pearson. ISBN: 9788131718070.
- HeliconSoft (2024). *Helicon Focus*. <https://www.heliconsoft.com/heliconsoft-products/helicon-focus/>. Accessed: 2024-09-24.
- Hergenröder, R. (2006). "Hydrodynamic sputtering as a possible source for fractionation in LA-ICP-MS". In: *J. Anal. At. Spectrom.* 21.5, pp. 517–524. ISSN: 1364-5544. DOI: [10.1039/b600705h](https://doi.org/10.1039/b600705h).
- Hodgson, N., Allegre, H., Caprara, A., Starodoumov, A., and Bettencourt, S. (2021). "Efficiency of ultrafast laser ablation in burst mode as a function of intra-burst repetition rate and pulse fluence". In: *Frontiers in Ultrafast Optics: Biomedical, Scientific, and Industrial Applications XXI*. Ed. by Herman, P. R., Meunier, M., and Osellame, R. SPIE. DOI: [10.1117/12.2576277](https://doi.org/10.1117/12.2576277).
- Holme, C., Gkinis, V., and Vinther, B. M. (2018). "Molecular diffusion of stable water isotopes in polar firn as a proxy for past temperatures". In: *Geochimica et Cosmochimica Acta* 225, pp. 128–145. ISSN: 0016-7037. DOI: [10.1016/j.gca.2018.01.015](https://doi.org/10.1016/j.gca.2018.01.015).
- Huber, C. and Leuenberger, M. (2003). "Fast high-precision on-line determination of hydrogen isotope ratios of water or ice by continuous-flow isotope ratio mass spectrometry". In: *Rapid Communications in Mass Spectrometry* 17.12, pp. 1319–1325. ISSN: 1097-0231. DOI: [10.1002/rcm.1055](https://doi.org/10.1002/rcm.1055).

- Jackson, S. E. and Günther, D. (2003). "The nature and sources of laser induced isotopic fractionation in laser ablation-multicollector-inductively coupled plasma-mass spectrometry". In: *Journal of Analytical Atomic Spectrometry* 18.3, pp. 205–212. ISSN: 1364-5544. DOI: [10.1039/b209620j](https://doi.org/10.1039/b209620j).
- Jee, Y., Becker, M. F., and Walser, R. M. (1988). "Laser-induced damage on single-crystal metal surfaces". In: *Journal of the Optical Society of America B* 5.3, p. 648. ISSN: 1520-8540. DOI: [10.1364/josab.5.000648](https://doi.org/10.1364/josab.5.000648).
- Jiang, L and Tsai, H. L. (2004). "Prediction of crater shape in femtosecond laser ablation of dielectrics". In: *Journal of Physics D: Applied Physics* 37.10, pp. 1492–1496. ISSN: 1361-6463. DOI: [10.1088/0022-3727/37/10/012](https://doi.org/10.1088/0022-3727/37/10/012).
- Johnsen, S. J., Clausen, H. B., Cuffey, K. M., Hoffmann, G., Schwander, J., and Creyts, T (2000). *Diffusion of stable isotopes in polar firn and ice. The isotope effect in firn diffusion*. Ed. by Hondoh, T. Physics of Ice Core Records, Hokkaido University Press, Sapporo.
- Johnsen, S. J., Dansgaard, W., and White, J. W. C. (1989). "The origin of Arctic precipitation under present and glacial conditions". In: *Tellus B* 41B.4, pp. 452–468. ISSN: 1600-0889. DOI: [10.1111/j.1600-0889.1989.tb00321.x](https://doi.org/10.1111/j.1600-0889.1989.tb00321.x).
- Johnsen, S. J., Dahl-Jensen, D., Gundestrup, N., Steffensen, J. P., Clausen, H. B., Miller, H., Masson-Delmotte, V., Sveinbjörnsdóttir, A. E., and White, J. (2001). "Oxygen isotope and palaeotemperature records from six Greenland ice-core stations: Camp Century, Dye-3, GRIP, GISP2, Renland and NorthGRIP". In: *Journal of Quaternary Science* 16.4, pp. 299–307. ISSN: 1099-1417. DOI: [10.1002/jqs.622](https://doi.org/10.1002/jqs.622).
- Johnsen, S. J. (1977). "Stable isotope homogenization of polar firn and ice". In: *Proceedings of Symposium on Isotopes and Impurities in Snow and Ice, IUGG XVI, General Assembly, Grenoble*, 210 – 219. URL: <https://api.semanticscholar.org/CorpusID:56206574>.
- Jones, T. R., Cuffey, K. M., White, J. W. C., Steig, E. J., Buizert, C., Markle, B. R., McConnell, J. R., and Sigl, M. (2017a). "Water isotope diffusion in the WAIS Divide ice core during the Holocene and last glacial". In: *Journal of Geophysical Research: Earth Surface* 122.1, pp. 290–309. ISSN: 2169-9011. DOI: [10.1002/2016jf003938](https://doi.org/10.1002/2016jf003938).
- Jones, T. R., White, J. W. C., Steig, E. J., Vaughn, B. H., Morris, V., Gkinis, V., Markle, B. R., and Schoenemann, S. W. (2017b). "Improved methodologies for continuous-flow analysis of stable water isotopes in ice cores". In: *Atmospheric Measurement Techniques* 10.2, pp. 617–632. ISSN: 1867-8548. DOI: [10.5194/amt-10-617-2017](https://doi.org/10.5194/amt-10-617-2017).
- Jouzel, J. (2013). "A brief history of ice core science over the last 50 yr". In: *Climate of the Past* 9.6, pp. 2525–2547. ISSN: 1814-9332. DOI: [10.5194/cp-9-2525-2013](https://doi.org/10.5194/cp-9-2525-2013).
- Jouzel, J., Alley, R. B., Cuffey, K. M., Dansgaard, W., Grootes, P., Hoffmann, G., Johnsen, S. J., Koster, R. D., Peel, D., Shuman, C. A., Stievenard, M., Stuiver, M., and White, J. (1997). "Validity of the temperature reconstruction from water isotopes in ice cores". In: *Journal of Geophysical Research: Oceans* 102.C12, pp. 26471–26487. ISSN: 0148-0227. DOI: [10.1029/97jc01283](https://doi.org/10.1029/97jc01283).
- Jouzel, J. and Masson-Delmotte, V. (2010). "Deep ice cores: the need for going back in time". In: *Quaternary Science Reviews* 29.27–28, pp. 3683–3689. ISSN: 0277-3791. DOI: [10.1016/j.quascirev.2010.10.002](https://doi.org/10.1016/j.quascirev.2010.10.002).
- Jouzel, J. and Merlivat, L. (1984). "Deuterium and oxygen 18 in precipitation: Modeling of the isotopic effects during snow formation". In: *Journal of Geophysical Research: Atmospheres* 89.D7, pp. 11749–11757. ISSN: 0148-0227. DOI: [10.1029/jd089id07p11749](https://doi.org/10.1029/jd089id07p11749).

- Kahle, E. C., Holme, C., Jones, T. R., Gkinis, V., and Steig, E. J. (2018). "A Generalized Approach to Estimating Diffusion Length of Stable Water Isotopes From Ice-Core Data". In: *Journal of Geophysical Research: Earth Surface* 123.10, pp. 2377–2391. ISSN: 2169-9011. DOI: [10.1029/2018jf004764](https://doi.org/10.1029/2018jf004764).
- Kahle, E. C., Steig, E. J., Jones, T. R., Fudge, T. J., Koutnik, M. R., Morris, V. A., Vaughn, B. H., Schauer, A. J., Stevens, C. M., Conway, H., Waddington, E. D., Buizert, C., Epifanio, J., and White, J. W. C. (2021). "Reconstruction of Temperature, Accumulation Rate, and Layer Thinning From an Ice Core at South Pole, Using a Statistical Inverse Method". In: *Journal of Geophysical Research: Atmospheres* 126.13. ISSN: 2169-8996. DOI: [10.1029/2020jd033300](https://doi.org/10.1029/2020jd033300).
- Kaufmann, P. R., Federer, U., Hutterli, M. A., Bigler, M., Schüpbach, S., Ruth, U., Schmitt, J., and Stocker, T. F. (2008). "An Improved Continuous Flow Analysis System for High-Resolution Field Measurements on Ice Cores". In: *Environmental Science and Technology* 42.21, pp. 8044–8050. ISSN: 1520-5851. DOI: [10.1021/es8007722](https://doi.org/10.1021/es8007722).
- Kerstel, E. and Gianfrani, L. (2008). "Advances in laser-based isotope ratio measurements: selected applications". In: *Applied Physics B* 92.3, pp. 439–449. ISSN: 1432-0649. DOI: [10.1007/s00340-008-3128-x](https://doi.org/10.1007/s00340-008-3128-x).
- Kerstel, E. (2004). "Isotope Ratio Infrared Spectrometry". In: *Handbook of Stable Isotope Analytical Techniques*. Elsevier, pp. 759–787. ISBN: 9780444511140. DOI: [10.1016/b978-044451114-0/50036-3](https://doi.org/10.1016/b978-044451114-0/50036-3).
- Kerttu, M. P. (2021). "Developing a Method for High Resolution for Water Isotope Measurements in Ice Cores". MA thesis. University of Copenhagen, Physics of Ice, Climate and Earth.
- Khonina, S. N., Kazanskiy, N. L., Khorin, P. A., and Butt, M. A. (2021). "Modern Types of Axicons: New Functions and Applications". In: *Sensors* 21.19, p. 6690. ISSN: 1424-8220. DOI: [10.3390/s21196690](https://doi.org/10.3390/s21196690).
- Koch, J., Wälle, M., Dietiker, R., and Günther, D. (2008). "Analysis of Laser-Produced Aerosols by Inductively Coupled Plasma Mass Spectrometry: Transport Phenomena and Elemental Fractionation". In: *Analytical Chemistry* 80.4, pp. 915–921. ISSN: 1520-6882. DOI: [10.1021/ac071450d](https://doi.org/10.1021/ac071450d).
- Krüger, J. and Kautek, W. (2004). "Ultrashort Pulse Laser Interaction with Dielectrics and Polymers". In: *Polymers and Light*. Springer Berlin Heidelberg, pp. 247–290. ISBN: 9783540450412. DOI: [10.1007/b12683](https://doi.org/10.1007/b12683).
- Kuhn, H.-R. and Günther, D. (2003). "Elemental Fractionation Studies in Laser Ablation Inductively Coupled Plasma Mass Spectrometry on Laser-Induced Brass Aerosols". In: *Analytical Chemistry* 75.4, pp. 747–753. ISSN: 1520-6882. DOI: [10.1021/ac0259919](https://doi.org/10.1021/ac0259919).
- Kuhn, H.-R., Pearson, N. J., and Jackson, S. E. (2007). "The influence of the laser ablation process on isotopic fractionation of copper in LA-MC-ICP-MS". In: *Journal of Analytical Atomic Spectrometry* 22.5, p. 547. ISSN: 1364-5544. DOI: [10.1039/b616232k](https://doi.org/10.1039/b616232k).
- Landais, A., Barkan, E., and Luz, B. (2008). "Record of ^{18}O and ^{17}O -excess in ice from Vostok Antarctica during the last 150,000 years". In: *Geophysical Research Letters* 35.2. ISSN: 1944-8007. DOI: [10.1029/2007g1032096](https://doi.org/10.1029/2007g1032096).
- Leitz, K.-H., Redlingshöfer, B., Reg, Y., Otto, A., and Schmidt, M. (2011). "Metal Ablation with Short and Ultrashort Laser Pulses". In: *Physics Procedia* 12, pp. 230–238. ISSN: 1875-3892. DOI: [10.1016/j.phpro.2011.03.128](https://doi.org/10.1016/j.phpro.2011.03.128).

- Lilien, D. A., Steinhage, D., Taylor, D., Parrenin, F., Ritz, C., Mulvaney, R., Martín, C., Yan, J.-B., O'Neill, C., Frezzotti, M., Miller, H., Gogineni, P., Dahl-Jensen, D., and Eisen, O. (2021). "Brief communication: New radar constraints support presence of ice older than 1.5Myr at Little Dome C". In: *The Cryosphere* 15.4, pp. 1881–1888. ISSN: 1994-0424. DOI: [10.5194/tc-15-1881-2021](https://doi.org/10.5194/tc-15-1881-2021).
- Litvin, I., McLaren, M., and Forbes, A. (2008). "Propagation of obstructed Bessel and Bessel–Gauss beams". In: *Proceedings of SPIE - The International Society for Optical Engineering* 7062. DOI: [10.1117/12.793695](https://doi.org/10.1117/12.793695).
- Liu, J. M. (1982). "Simple technique for measurements of pulsed Gaussian-beam spot sizes". In: *Optics Letters* 7.5, p. 196. ISSN: 1539-4794. DOI: [10.1364/ol.7.000196](https://doi.org/10.1364/ol.7.000196).
- Luz, B. and Barkan, E. (2010). "Variations of $^{17}\text{O}/^{16}\text{O}$ and $^{18}\text{O}/^{16}\text{O}$ in meteoric waters". In: *Geochimica et Cosmochimica Acta* 74.22, pp. 6276–6286. ISSN: 0016-7037. DOI: [10.1016/j.gca.2010.08.016](https://doi.org/10.1016/j.gca.2010.08.016).
- Malegiannaki, E., Bohleber, P., Zannoni, D., Stremtan, C., Petteni, A., Stenni, B., Barbante, C., Vinther, B. M., and Gkinis, V. (2024). "Towards high-resolution water isotope analysis in ice cores using laser ablation – cavity ring-down spectroscopy". In: *Analyst*. ISSN: 1364-5528. DOI: [10.1039/d4an01054j](https://doi.org/10.1039/d4an01054j).
- Mannion, P., Magee, J., Coyne, E., O'Connor, G., and Glynn, T. (2004). "The effect of damage accumulation behaviour on ablation thresholds and damage morphology in ultrafast laser micro-machining of common metals in air". In: *Applied Surface Science* 233.1–4, pp. 275–287. ISSN: 0169-4332. DOI: [10.1016/j.apsusc.2004.03.229](https://doi.org/10.1016/j.apsusc.2004.03.229).
- Mao, S. S., Quéré, F., Guizard, S., Mao, X., Russo, R. E., Petite, G., and Martin, P. (2004). "Dynamics of femtosecond laser interactions with dielectrics". In: *Applied Physics A* 79.7, pp. 1695–1709. ISSN: 1432-0630. DOI: [10.1007/s00339-004-2684-0](https://doi.org/10.1007/s00339-004-2684-0).
- Marks, M. R., Cheong, K. Y., and Hassan, Z. (2022). "A review of laser ablation and dicing of Si wafers". In: *Precision Engineering* 73, pp. 377–408. ISSN: 0141-6359. DOI: [10.1016/j.precisioneng.2021.10.001](https://doi.org/10.1016/j.precisioneng.2021.10.001).
- Masson-Delmotte, V., Jouzel, J., Landais, A., Stievenard, M., Johnsen, S. J., White, J. W. C., Werner, M., Sveinbjornsdottir, A., and Fuhrer, K. (2005). "GRIP Deuterium Excess Reveals Rapid and Orbital-Scale Changes in Greenland Moisture Origin". In: *Science* 309.5731, pp. 118–121. ISSN: 1095-9203. DOI: [10.1126/science.1108575](https://doi.org/10.1126/science.1108575).
- McGloin, D and Dholakia, K (2005). "Bessel beams: Diffraction in a new light". In: *Contemporary Physics* 46.1, pp. 15–28. DOI: [10.1080/0010751042000275259](https://doi.org/10.1080/0010751042000275259). eprint: <https://doi.org/10.1080/0010751042000275259>.
- Miller, M. F. (2002). "Isotopic fractionation and the quantification of ^{17}O anomalies in the oxygen three-isotope system". In: *Geochimica et Cosmochimica Acta* 66.11, pp. 1881–1889. ISSN: 0016-7037. DOI: [10.1016/s0016-7037\(02\)00832-3](https://doi.org/10.1016/s0016-7037(02)00832-3).
- Mirza, I., Bulgakova, N. M., Tomáščík, J., Michálek, V., Haderka, O., Fekete, L., and Mocek, T. (2016). "Ultrashort pulse laser ablation of dielectrics: Thresholds, mechanisms, role of breakdown". In: *Scientific Reports* 6.1. ISSN: 2045-2322. DOI: [10.1038/srep39133](https://doi.org/10.1038/srep39133).
- Mook, W. (2000). *Environmental Isotopes in the Hydrological Cycle: Principles and Applications*. Vol. I. IAEA, Unesco and IAEA.

- Motizuki, Y., Nakai, Y., Takahashi, K., Hirose, J., Sahoo, Y. V., Yumoto, M., Maruyama, M., Sakashita, M., Kase, K., Wada, S., Motoyama, H., and Yano, Y. (2023). "A novel laser melting sampler for discrete, sub-centimeter depth-resolved analyses of stable water isotopes in ice cores". In: *Journal of Glaciology*, pp. 1–7. ISSN: 1727-5652. DOI: [10.1017/jog.2023.52](https://doi.org/10.1017/jog.2023.52).
- Murphy, D. M. and Koop, T. (2005). "Review of the vapour pressures of ice and supercooled water for atmospheric applications". In: *Quarterly Journal of the Royal Meteorological Society* 131.608, pp. 1539–1565. ISSN: 1477-870X. DOI: [10.1256/qj.04.94](https://doi.org/10.1256/qj.04.94).
- Müller, W., Shelley, J. M. G., and Rasmussen, S. O. (2011). "Direct chemical analysis of frozen ice cores by UV-laser ablation ICPMS". In: *J. Anal. At. Spectrom.* 26 (12), pp. 2391–2395. DOI: [10.1039/C1JA10242G](https://doi.org/10.1039/C1JA10242G).
- Ng, F. S. L. (2023). "Isotopic diffusion in ice enhanced by vein-water flow". In: *The Cryosphere* 17.7, pp. 3063–3082. ISSN: 1994-0424. DOI: [10.5194/tc-17-3063-2023](https://doi.org/10.5194/tc-17-3063-2023).
- Nolte, S., Momma, C., Jacobs, H., Tünnermann, A., Chichkov, B. N., Wellegehausen, B., and Welling, H. (1997). "Ablation of metals by ultrashort laser pulses". In: *Journal of the Optical Society of America B* 14.10, p. 2716. ISSN: 1520-8540. DOI: [10.1364/josab.14.002716](https://doi.org/10.1364/josab.14.002716).
- Peensoo, K. M. (2024). "Developing a Method for High Resolution Water Isotope Measurements in Ice Cores". PhD thesis. University of Copenhagen. DOI: [10.5281/zenodo.14048968](https://doi.org/10.5281/zenodo.14048968).
- Poitrasson, F. and d'Abzac, F.-X. (2017). "Femtosecond laser ablation inductively coupled plasma source mass spectrometry for elemental and isotopic analysis: are ultrafast lasers worthwhile?" In: *J. Anal. At. Spectrom.* 32 (6), pp. 1075–1091. DOI: [10.1039/C7JA00084G](https://doi.org/10.1039/C7JA00084G).
- Pol, K., Masson-Delmotte, V., Johnsen, S., Bigler, M., Cattani, O., Durand, G., Falourd, S., Jouzel, J., Minster, B., Parrenin, F., Ritz, C., Steen-Larsen, H., and Stenni, B. (2010). "New MIS 19 EPICA Dome C high resolution deuterium data: Hints for a problematic preservation of climate variability at sub-millennial scale in the "oldest ice"". In: *Earth and Planetary Science Letters* 298.1–2, pp. 95–103. ISSN: 0012-821X. DOI: [10.1016/j.eps1.2010.07.030](https://doi.org/10.1016/j.eps1.2010.07.030).
- Prahl, S. (2021). *LaserBeamSize: A Python package to calculate and plot Gaussian beam parameters*. <https://pypi.org/project/laserbeamsize/>. Version 1.0.8.
- Raciukaitis, G., Brikas, M., Gecys, P., and Gedvilas, M. (2008). "Accumulation effects in laser ablation of metals with high-repetition-rate lasers". In: *High-Power Laser Ablation VII*. Ed. by Phipps, C. R. SPIE. DOI: [10.1117/12.782937](https://doi.org/10.1117/12.782937).
- Reinhardt, H., Kriews, M., Miller, H., Schrems, O., Lüdke, C., Hoffmann, E., and Skole, J. (2001). "Laser ablation inductively coupled plasma mass spectrometry: a new tool for trace element analysis in ice cores". In: *Analytical and Bioanalytical Chemistry* 370.5, pp. 629–636. ISSN: 1618-2650. DOI: [10.1007/s002160100853](https://doi.org/10.1007/s002160100853).
- Russo, R. E., Mao, X., and Borisov, O. V. (1998). "Laser ablation sampling". In: *TrAC Trends in Analytical Chemistry* 17.8, pp. 461–469. ISSN: 0165-9936. DOI: [10.1016/S0165-9936\(98\)00047-8](https://doi.org/10.1016/S0165-9936(98)00047-8).
- Russo, R. E., Mao, X., Liu, H., Gonzalez, J., and Mao, S. S. (2002). "Laser ablation in analytical chemistry—a review". In: *Talanta* 57.3, pp. 425–451. ISSN: 0039-9140. DOI: [10.1016/S0039-9140\(02\)00053-X](https://doi.org/10.1016/S0039-9140(02)00053-X).

- Schmidt, M. R. (2021). "Whispers of Ancient Air Bubbles in Polar Ice". MA thesis. University of Copenhagen, Physics of Ice, Climate and Earth.
- Schoenemann, S. W., Steig, E. J., Ding, Q., Markle, B. R., and Schauer, A. J. (2014). "Triple water-isotopologue record from WAIS Divide, Antarctica: Controls on glacial-interglacial changes in ^{17}O excess of precipitation". In: *Journal of Geophysical Research: Atmospheres* 119.14, pp. 8741–8763. ISSN: 2169-8996. DOI: [10.1002/2014jd021770](https://doi.org/10.1002/2014jd021770).
- Severinghaus, J. P., Sowers, T., Brook, E. J., Alley, R. B., and Bender, M. L. (1998). "Timing of abrupt climate change at the end of the Younger Dryas interval from thermally fractionated gases in polar ice". In: *Nature* 391.6663, pp. 141–146. ISSN: 1476-4687. DOI: [10.1038/34346](https://doi.org/10.1038/34346).
- Sharp, Z. (2007). *Principles of Stable Isotope Geochemistry*. Pearson/Prentice Hall. ISBN: 9780130091390.
- Shaw, F., Dolman, A. M., Kunz, T., Gkinis, V., and Laepple, T. (2024). "Novel approach to estimate the water isotope diffusion length in deep ice cores with an application to Marine Isotope Stage 19 in the Dome C ice core". In: *The Cryosphere* 18.8, pp. 3685–3698. ISSN: 1994-0424. DOI: [10.5194/tc-18-3685-2024](https://doi.org/10.5194/tc-18-3685-2024).
- Shugaev, M. V., Wu, C., Armbruster, O., Naghilou, A., Brouwer, N., Ivanov, D. S., Derrien, T. J.-Y., Bulgakova, N. M., Kautek, W., Rethfeld, B., and Zhigilei, L. V. (2016). "Fundamentals of ultrafast laser–material interaction". In: *MRS Bulletin* 41.12, pp. 960–968. ISSN: 1938-1425. DOI: [10.1557/mrs.2016.274](https://doi.org/10.1557/mrs.2016.274).
- Sneed, S. B., Mayewski, P. A., Sayre, W. G., Handley, M. J., Kurbatov, A. V., Taylor, K. C., Bohleber, P., Wagenbach, D., Erhardt, T. M., and Spaulding, N. E. (2015). "New LA-ICP-MS cryocell and calibration technique for sub-millimeter analysis of ice cores". In: *Journal of Glaciology* 61, pp. 233–242.
- Spaulding, N. E., Sneed, S. B., Handley, M. J., Bohleber, P., Kurbatov, A. V., Pearce, N. J., Erhardt, T., and Mayewski, P. A. (2017). "A New Multielement Method for LA-ICP-MS Data Acquisition from Glacier Ice Cores". In: *Environ. Sci. Technol.* 51.22, pp. 13282–13287. ISSN: 0013-936X. DOI: [10.1021/acs.est.7b03950](https://doi.org/10.1021/acs.est.7b03950).
- Steig, E. J., Gkinis, V., Schauer, A. J., Schoenemann, S. W., Samek, K., Hoffnagle, J., Dennis, K. J., and Tan, S. M. (2014). "Calibrated high-precision ^{17}O -excess measurements using cavity ring-down spectroscopy with laser-current-tuned cavity resonance". In: *Atmospheric Measurement Techniques* 7.8, pp. 2421–2435. ISSN: 1867-8548. DOI: [10.5194/amt-7-2421-2014](https://doi.org/10.5194/amt-7-2421-2014).
- Steig, E. J., Jones, T. R., Schauer, A. J., Kahle, E. C., Morris, V. A., Vaughn, B. H., Davidge, L., and White, J. W. C. (2021). "Continuous-Flow Analysis of $\delta^{17}\text{O}$, $\delta^{18}\text{O}$, and δD of H_2O on an Ice Core from the South Pole". In: *Frontiers in Earth Science* 9. ISSN: 2296-6463. DOI: [10.3389/feart.2021.640292](https://doi.org/10.3389/feart.2021.640292).
- Stenni, B., Jouzel, J., Masson-Delmotte, V., Röthlisberger, R., Castellano, E., Cattani, O., Falourd, S., Johnsen, S., Longinelli, A., and Sachs, J. (2004). "A late-glacial high-resolution site and source temperature record derived from the EPICA Dome C isotope records (East Antarctica)". In: *Earth and Planetary Science Letters* 217.1–2, pp. 183–195. ISSN: 0012-821X. DOI: [10.1016/s0012-821x\(03\)00574-0](https://doi.org/10.1016/s0012-821x(03)00574-0).
- Stremtan, C., Wozniak, J., Puscas, C. M., and Tamas, T. (2024). "Laser Ablation - Cavity Ring Down Spectrometry, a new method for the in-situ analysis of $\delta^{13}\text{C}$ of organic and inorganic carbonates". In: *EGU General Assembly 2024*. DOI: [10.5194/egusphere-egu24-17192](https://doi.org/10.5194/egusphere-egu24-17192).

- Stuart, B. C., Feit, M. D., Herman, S., Rubenchik, A. M., Shore, B. W., and Perry, M. D. (1996). "Nanosecond-to-femtosecond laser-induced breakdown in dielectrics". In: *Physical Review B* 53.4, pp. 1749–1761. ISSN: 1095-3795. DOI: [10.1103/physrevb.53.1749](https://doi.org/10.1103/physrevb.53.1749).
- Van Helden, T., Merviĉ, K., Nemet, I., Elteren, J. T. van, Vanhaecke, F., Ronĉeviĉ, S., Šala, M., and Van Acker, T. (2024). "Evaluation of two-phase sample transport upon ablation of gelatin as a proxy for soft biological matrices using nanosecond laser ablation – inductively coupled plasma – mass spectrometry". In: *Analytica Chimica Acta* 1287, p. 342089. ISSN: 0003-2670. DOI: [10.1016/j.aca.2023.342089](https://doi.org/10.1016/j.aca.2023.342089).
- Warren, S. G. and Brandt, R. E. (2008). "Optical constants of ice from the ultraviolet to the microwave: A revised compilation". In: *Journal of Geophysical Research: Atmospheres* 113.D14. ISSN: 0148-0227. DOI: [10.1029/2007jd009744](https://doi.org/10.1029/2007jd009744).
- Weingarten, K. (May 2009). "High Energy Picosecond Lasers: Ready for Prime Time: Industrial-grade picosecond laser systems extend micromachining applications". In: *Laser Technik Journal* 6.3, pp. 51–54. ISSN: 1863-9119. DOI: [10.1002/latj.200990041](https://doi.org/10.1002/latj.200990041).
- WeMacro (2023). *WeMacro Rail Manual*. <https://www.wemacro.com/?p=509>. Accessed: 2024-09-24.
- (2024). *WeMacro Automatic Macro Rail*. <https://www.wemacro.com/?p=509>. Accessed: 2024-09-24.
- Wilson, J. and B., H. J. F. (1998). *Optoelectronics an introduction*. Prentice Hall.
- Wædegaard, K., Frislev, M., and Balling, P. (2012). "Femtosecond laser excitation of dielectric materials: experiments and modeling of optical properties and ablation depths". In: *Applied Physics A* 110.3, pp. 601–605. ISSN: 1432-0630. DOI: [10.1007/s00339-012-7136-7](https://doi.org/10.1007/s00339-012-7136-7).
- Yang, F., Kang, R., Ma, H., Ma, G., Wu, D., and Dong, Z. (2023). "Effect of Femtosecond Laser Processing Parameters on the Ablation Microgrooves of RB-SiC Composites". In: *Materials* 16.6, p. 2536. ISSN: 1996-1944. DOI: [10.3390/ma16062536](https://doi.org/10.3390/ma16062536).
- Yang, J., Zhao, Y., Zhang, N., Liang, Y., and Wang, M. (2007). "Ablation of metallic targets by high-intensity ultrashort laser pulses". In: *Physical Review B* 76.16, p. 165430. ISSN: 1550-235X. DOI: [10.1103/physrevb.76.165430](https://doi.org/10.1103/physrevb.76.165430).
- Zhang, B., He, M., Hang, W., and Huang, B. (2013). "Minimizing Matrix Effect by Femtosecond Laser Ablation and Ionization in Elemental Determination". In: *Analytical Chemistry* 85.9, pp. 4507–4511. ISSN: 1520-6882. DOI: [10.1021/ac400072j](https://doi.org/10.1021/ac400072j).
- Zhang, W. and Hu, Z. (2020). "A critical review of isotopic fractionation and interference correction methods for isotope ratio measurements by laser ablation multi-collector inductively coupled plasma mass spectrometry". In: *Spectrochimica Acta Part B: Atomic Spectroscopy* 171, p. 105929. ISSN: 0584-8547. DOI: [10.1016/j.sab.2020.105929](https://doi.org/10.1016/j.sab.2020.105929).
- Zhao, W., Wang, L., Yu, Z., Chen, J., and Yang, J. (2019). "A processing technology of grooves by picosecond ultrashort pulse laser in Ni alloy: Enhancing efficiency and quality". In: *Optics and Laser Technology* 111, pp. 214–221. ISSN: 0030-3992. DOI: [10.1016/j.optlastec.2018.09.056](https://doi.org/10.1016/j.optlastec.2018.09.056).

- Zheng, X.-Y., Beard, B. L., Lee, S., Reddy, T. R., Xu, H., and Johnson, C. M. (2017). "Contrasting particle size distributions and Fe isotope fractionations during nanosecond and femtosecond laser ablation of Fe minerals: Implications for LA-MC-ICP-MS analysis of stable isotopes". In: *Chemical Geology* 450, pp. 235–247. ISSN: 0009-2541. DOI: [10.1016/j.chemgeo.2016.12.038](https://doi.org/10.1016/j.chemgeo.2016.12.038).
- Zhou, L., Jiang, Y., Wei, H., Zhang, S., Ma, X., Zhang, P., Pan, X., Fan, W., and Li, X. (2023). "Investigation on hybrid laser ablation and its application in fused silica damage mitigation". In: *Optics Express* 31.3, p. 4553. ISSN: 1094-4087. DOI: [10.1364/oe.478949](https://doi.org/10.1364/oe.478949).